Röhl, U., Thomas, D.J., Childress, L.B., and the Expedition 378 Scientists
Proceedings of the International Ocean Discovery Program Volume 378
publications.iodp.org

Site U1553[1]

Contents
1 Background and objectives
5 Operations
10 Lithostratigraphy
27 Biostratigraphy and micropaleontology
50 Paleomagnetism
61 Geochemistry
70 Physical properties
75 Stratigraphic correlation
80 Age-depth model and mass accumulation rates
84 References

Keywords
International Ocean Discovery Program, IODP, *JOIDES Resolution*, Expedition 378, South Pacific Paleogene Climate, Climate and Ocean Change, Site U1553, Campbell Plateau, high-southern latitude, Cenozoic climate history, carbon system dynamics, high CO_2 world, Paleocene, Eocene, Oligocene, chronostratigraphy, perturbations, temperature gradients, ocean circulation, intermediate water formation, hydrologic cycling, biological productivity, ice sheet dynamics, plate motion, wind fields

Core descriptions

Supplementary material

References (RIS)

MS 378-103
Published 6 February 2022

Funded by NSF OCE1326927

U. Röhl, D.J. Thomas, L.B. Childress, E. Anagnostou, B. Ausín, B. Borba Dias, F. Boscolo-Galazzo, S. Brzelinski, A.G. Dunlea, S.C. George, L.L. Haynes, I.L. Hendy, H.L. Jones, S.S. Khanolkar, G.D. Kitch, H. Lee, I. Raffi, A.J. Reis, R.M. Sheward, E. Sibert, E. Tanaka, R. Wilkens, K. Yasukawa, W. Yuan, Q. Zhang, Y. Zhang, A.J. Drury, and C.J. Hollis[2]

[1] Röhl, U., Thomas, D.J., Childress, L.B., Anagnostou, E., Ausín, B., Borba Dias, B., Boscolo-Galazzo, F., Brzelinski, S., Dunlea, A.G., George, S.C., Haynes, L.L., Hendy, I.L., Jones, H.L., Khanolkar, S.S., Kitch, G.D., Lee, H., Raffi, I., Reis, A.J., Sheward, R.M., Sibert, E., Tanaka, E., Wilkens, R., Yasukawa, K., Yuan, W., Zhang, Q., Zhang, Y., Drury, A.J., and Hollis, C.J., 2022. Site U1533. *In* Röhl, U., Thomas, D.J., Childress, L.B., and the Expedition 378 Scientists, *South Pacific Paleogene Climate*. Proceedings of the International Ocean Discovery Program, 378: College Station, TX (International Ocean Discovery Program). https://doi.org/10.14379/iodp.proc.378.103.2022

[2] **Expedition 378 Scientists' affiliations**

1. Background and objectives

1.1. Reconstruction of environmental conditions and physical processes in the Paleogene oceans

Ocean floor sediments have the potential to record many dimensions of past environmental conditions such as the major features of ocean circulation and the temperature and chemical composition of the water masses. From sedimentary records, we can infer water mass distributions and regions of steep gradients in temperature, salinity, and biologic productivity. For example, in the modern ocean surface water, provinces are identified by their salinity and temperature. Distinct assemblages of planktonic organisms are associated with these provinces; thus, microfossil assemblages of these organisms can be used to define the geographic extent of water masses in premodern sediments. Divergence of near-surface water usually supports higher organic productivity, which leaves a diagnostic geochemical and micropaleontological fingerprint in the underlying sediments. Steep gradients in the surface ocean are preserved in the records of planktonic microfossil assemblages and mark regions of vigorous near-surface transport such as wind-driven open-ocean and boundary currents. Winds that drive these currents may be reconstructed through the geochemical composition of the dust from upwind continental areas and the grain size of that dust once the contributions of volcanic ash have been characterized.

Reconstruction of the physical processes in the ocean provides substantial insight into past climate dynamics, particularly oceanic heat transport and its role in sustaining overall warm climates. In the present climate system, heat transport to the poles is divided approximately equally between the atmospheres and the oceans. Wind-driven currents achieve about half of the ocean heat transport, whereas the balance of oceanic heat transport is driven by the overturning circulation. Obviously, all aspects of heat transport must be defined as well as possible in our effort to better understand ocean circulation and the role it plays in times of extremely warm climates.

1.2. Sea-surface temperatures

The early Paleogene (66–34 Ma) was the most recent geologic interval during which atmospheric pCO_2 levels were likely above ~1000 ppm (e.g., Pearson et al., 2009; Pagani et al., 2011; Hönisch et al., 2012; Anagnostou et al., 2016, 2020; Gutjahr et al., 2017; Harper et al., 2020). Theory and models indicate that elevated atmospheric greenhouse gas inventories would have produced higher sea-surface temperatures (SSTs). These results are confirmed by multiproxy reconstructions of SSTs (Hollis et al., 2019) and indicate that tropical SSTs ranged from ~34° to 38°C at ~50 Ma (Pearson et al., 2007; Huber, 2008), SSTs in the high-latitude South Pacific (~55°S) and in the low-latitude Atlantic ranged from 20° to 35°C (Bijl et al., 2009; Hollis et al., 2012; Pross et al., 2012;

Cramwinckel et al., 2018), and SST estimates from Seymour Island were ~15°C (Ivany et al., 2011). These SST estimates produce early Paleogene equator-to-pole thermal gradients significantly lower than those of the modern ocean (e.g., Hollis et al., 2009; Lunt et al., 2012). Fully coupled model simulations using strong greenhouse gas radiative forcing yield seasonal thermal gradients generally consistent with the available proxy data (Huber and Caballero, 2011; Hollis et al., 2012; Lunt et al., 2012) but tend to produce meridional temperature gradients that remain somewhat too strong and typically underestimate high-latitude precipitation (Carmichael et al., 2016).

1.3. Ocean circulation

Oceanic meridional overturning circulation (MOC) is a crucial component of the climate system that impacts heat transport, nutrient transport, and global carbon cycling. The operating mode of the MOC was significantly different during the Late Cretaceous and early Paleogene (e.g., Thomas et al., 2014; Hutchinson et al., 2018). In the modern oceans, Antarctica is surrounded by the world's strongest ocean current, the Antarctic Circumpolar Current (ACC), which flows around Antarctica and reaches from the surface to abyssal depths. The current is sufficiently strong to cause erosion and sediment transport near its axis at 50°–55°S (e.g., Goodell et al., 1971; Watkins and Kennett, 1977; Hollister and Nowell, 1991; Barker and Thomas, 2004). In the early Paleogene, the Southern Ocean was divided into Pacific and Atlantic-Indian sectors because Australia and South America were joined to Antarctica. Each Southern Ocean sector developed a unique subpolar gyre; the Pacific sector gyre is known as the proto-Ross Gyre (Huber et al., 2004; Stickley et al., 2004).

An increasing catalog of water mass proxy data combined with state-of-the-art numerical simulations provides a reconstruction of MOC characterized by convection in the South Pacific and the North Pacific during the latest Cretaceous through early Paleogene. Nd isotope data also suggest that MOC in the Pacific Ocean was distinct and separate from that in the Atlantic Ocean (Thomas et al., 2014). This reconstruction is supported by fully coupled Global Circulation Model simulations that indicate the "age" of deep water in the Pacific Ocean increased from high to low latitudes in both the South and North Pacific (Hague et al., 2012).

Modern Antarctic circulation developed when deepwater passages were formed south of Australia (the Tasman Gateway) and through the Scotia arc (Drake Passage). Interestingly, abyssal hiatuses along the thermohaline flow path at the base of the Campbell Plateau developed at the time of the Eocene/Oligocene boundary, but shallow-water hiatuses developed perhaps 3 My later. Furthermore, data along the ACC flow path suggest that the ACC developed in the late Oligocene or at the Oligocene/Miocene boundary (Pfuhl and McCave, 2005; Lyle et al., 2007).

Data from Ocean Drilling Program (ODP) Leg 189 (Stickley et al., 2004; Bijl et al., 2013) suggest the earliest throughflow of a westbound ACC began at ~49–50 Ma through a southern opening of the Tasman Gateway in conjunction with the simultaneous onset of regional surface water and continental cooling (2°–4°C). The timing of subsequent deepening of the Tasman Gateway and Drake Passage is still not well constrained, and estimates range from the middle Eocene to the early Miocene for the development of circum-Antarctic deepwater passages and the formation of the full ACC (Lawver and Gahagan, 1998, 2003; Barker, 2001; Pfuhl and McCave, 2005; Scher and Martin, 2006). The impact of ACC formation on regional and global climate is still debated. The proposed sites in the pelagic southwestern Pacific will help constrain when the ACC formed and how it impacted climate evolution.

1.4. Water formation and hydrologic cycling

Deep and bottom water likely formed south of the Polar Front (e.g., van de Flierdt et al., 2004; Thomas et al., 2014), and the character of this deeper water can be assessed by measuring geochemical signals preserved in benthic foraminifers, fossil fish teeth and bones, and Fe-Mn oxide minerals at the proposed drill sites. Data from Site U1553 will enable us to assess existing models for the evolving mode of intermediate water formation through the Paleogene.

Proxy estimates of atmospheric CO_2, SSTs, and terrigenous organic matter inputs will contribute significantly to the understanding of Paleogene prevailing winds and hydrologic cycling. For

example, published model simulations and existing proxy data suggest that overall hydrologic cycling was more intense during the early Paleogene, resulting in higher precipitation in temperate and high latitudes (e.g., Pagani et al., 2006). Higher precipitation/humidity would have produced temperate- and high-latitude continental regions with greater vegetative cover than in drier periods. Lower aridity in these dust source regions would result in diminished dust transport to the ocean basins. Conversely, an enhanced hydrological cycle implies a drying of the arid-to-semiarid regions (Held and Soden, 2006) that may have enhanced the size of the subtropical dust source regions.

Only a few dust accumulation and provenance records exist for the Late Cretaceous and early Paleogene (e.g., Janecek and Rea, 1983; Hovan and Rea, 1992; Zhou and Kyte, 1992). In general, the compilation of long-term data indicates higher dust accumulation in the North Pacific (Deep Sea Drilling Project [DSDP] Site 576; piston Core LL44-GPC3) than the southern Indian Ocean (ODP Sites 756 and 757) during the Late Cretaceous and early Paleogene. Late Paleocene high-resolution data from Indian Ocean DSDP Site 215 show a transient increase in dust fluxes at ~59 Ma, but fluxes prior to and after the pulse seem to be consistent with the few other Southern Hemisphere locations (Hovan and Rea, 1992). Northern Hemisphere dust fluxes increased throughout the Neogene; however, the Indian Ocean sites record a slight decrease in flux throughout the Cenozoic. Site U1553 provides an opportunity to contribute to the record of dust deposition and provenance in the southwestern Pacific, and statistical analysis of bulk sediment elemental data will enable us to determine the accumulation rate of and distinguish between eolian dust and disseminated ash (e.g., Dunlea et al., 2015).

1.5. Chronostratigraphy

High-quality, multiple-hole Cenozoic sedimentary successions from the Atlantic (ODP Legs 171B, 207, and 208 and Integrated Ocean Drilling Program Expedition 342) and Pacific (ODP Legs 198 and 199 and Integrated Ocean Drilling Program Expeditions 320 and 321) drill sites yielded high-resolution geochemical records that also led to the development of astronomically calibrated age models (e.g., Röhl et al., 2007; Westerhold et al., 2011, 2018, 2020; Littler et al., 2014; Lauretano et al., 2016; Barnet et al., 2019). Expedition 378 will contribute a unique section that includes crucial time intervals for the South Pacific area and will be integrated into the global chronostratigraphy.

1.6. Previous drilling

The best-known Paleogene paleoceanographic site in the entire region is DSDP Site 277, which was drilled during Leg 29 in 1973. This site is located south of New Zealand, and the current water depth is ~1215 m. At that time, Leg 29 drilling recovered upper Oligocene to upper Paleocene carbonates by only rotary coring in a single hole; however, the Eocene portion of this hole was spot cored with low recovery (Kennett et al., 1975). The sediment sequence consists of ~10 m of Pliocene–Pleistocene carbonate ooze that is disconformably separated from an expanded middle Paleocene to upper Oligocene sequence with sedimentation rates of 19–22 m/My. The sediments spanning the upper Eocene to upper Oligocene are stiff carbonate oozes, and the ooze–chalk transition is nominally placed at 246 meters below seafloor (mbsf). Middle Paleocene to upper Eocene sediments are variably indurated but typically consist of chalks with low to moderate amounts of lithification (Kennett et al., 1975). Materials from this site provided most of the samples for two classic oxygen isotope curves that first defined the unusually warm early Eocene period (Shackleton and Kennett, 1975; Savin, 1977).

Improvements in advanced piston corer (APC) and half-length APC (HLAPC) technologies and better core-log integration have vastly improved the ability to develop triple-core stratigraphic splices and to correlate seismic reflection data. This capacity will allow us unprecedented insight into the details and timing of the major events preserved in the sedimentary record on the Campbell Plateau (Hollis et al., 2015).

1.7. Revised scientific objectives for Site U1553

Expedition 378, as laid out in International Ocean Discovery Program (IODP) Proposal 567-Full4, sought to elucidate the temperate to subpolar climate and oceanography of the very warm Eocene, as well as the late Paleogene and late Cenozoic, in the far southern Pacific Ocean. Drill sites are positioned along Anomaly 25 (56 Ma) between 56° and 70°S paleolatitudes (using the Ocean Drilling Stratigraphic Network web page backtrack scheme; **https://www.odsn.de**).

Revised drilling operations for Expedition 378 eliminated all the abyssal sites listed in the *Scientific Prospectus* and prompted a significant revision of the scientific objectives of the expedition. Much of the transit from Lautoka, Fiji, to Site U1553 was devoted to revisiting laboratory groups and individual science plans to ensure that each member of the science party had the ability to contribute to postcruise science. All of the science plans were crafted to exploit the new continuously cored, multiple-hole sediment section to achieve the following revised objectives:

1. To reconstruct the surface and deepwater temperatures, as well as vertical temperature gradients, through the Paleogene and Late Cretaceous, with particular emphasis on the major events that punctuate this long-term record (Eocene–Oligocene transition [EOT], Middle Eocene Climatic Optimum, Paleocene/Eocene Thermal Maximum [PETM], and Cretaceous/Paleogene [K/Pg] boundary);
2. To develop a common chronostratigraphic framework for Paleogene Southern Ocean magnetostratigraphy, biostratigraphy, and cyclostratigraphy;
3. To refine our understanding of the evolution of seawater chemistry;
4. To evaluate Paleogene biological productivity and determine nutrient exchange and mixing of surface and subsurface waters;
5. To track the development and variability of South Pacific intermediate-water composition and its role in overturning circulation during the Paleogene and Late Cretaceous, with emphasis on refining the timing and development of the ACC;
6. To determine, if possible, Paleogene and Neogene development of ice rafting from Antarctica;
7. To better determine Paleogene Pacific plate motion; and
8. To reconstruct the evolution of the Paleogene wind field.

1.8. Seismic studies and site survey data

The original siting for DSDP Site 277 was based solely on drilling vessel *Glomar Challenger* shipboard subbottom depth profiling (3.5 kHz) (Shipboard Scientific Party, 1975) (Figure **F1**); no modern seismic surveys exist in the immediate vicinity of Site U1553.

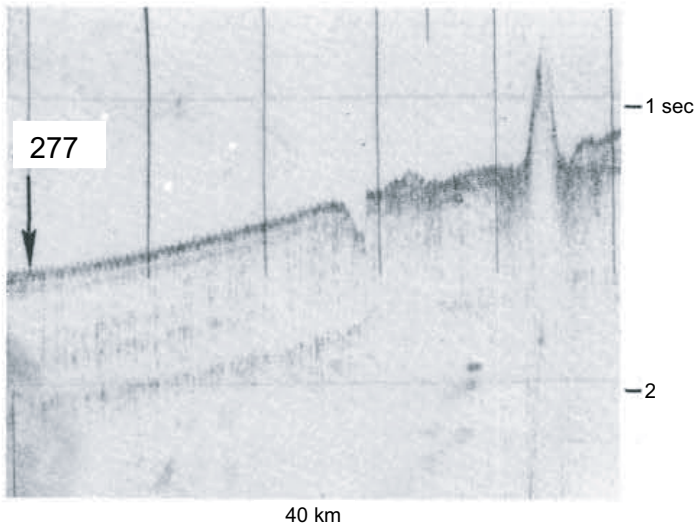

Figure F1. Shallow subbottom profiler record of DSDP Site 277 (Shipboard Scientific Party, 1975).

2. Operations

2.1. Port call

IODP Expedition 378 began in Lautoka, Fiji, at Queen's Wharf at 0800 h on 3 January 2020. The vessel had been tied up at Queen's Wharf for a maintenance period and to complete intermediate repairs on the piperacker skate and derrick. The Co-Chief Scientists, Expedition Project Manager (EPM), and *JOIDES Resolution* Science Operator (JRSO) technical staff boarded the vessel and began port call activities, including IODP JRSO crew change and crossover and Co-Chief Scientist orientations. The science party boarded the vessel on 4 January and began expedition preparations, including orientations on life at sea and safety. The science party continued safety training and received introductions in the laboratories during the rest of the port call.

During the 3 day port call, the ship crew change was completed, and some derrick repairs continued through 5 January. The welded areas of the derrick were inspected and painted, and rigdown of equipment was completed on 5 January. Two trucks of fresh produce were also loaded aboard the vessel.

The vessel was readied for departure, and the pilot came on board at 0656 h on 6 January. The last line was released at 0720 h to start the transit to Site U1553 (DSDP Site 277). The first fire and lifeboat safety drill was held for everyone on board. The Co-Chief Scientists and EPM met with each laboratory team to discuss requirements, tasks, and issues, and the teams began to prepare for their work.

2.2. Site U1553

Site U1553 was the only site occupied during Expedition 378. The research vessel *JOIDES Resolution* completed the 2249 nmi transit from Fiji to Site U1553 in 221.5 h (9.2 d). The vessel arrived on site at 1148 h on 15 January 2020. The thrusters were lowered, and the dynamic positioning system was engaged. At 1210 h, operations began for Site U1553.

Hole location, water depth, and the number of cores recovered are listed in Table **T1**. All times below are local ship time (UTC + 13 h) unless otherwise noted.

2.2.1. Hole U1553A

The APC/extended core barrel (XCB) bottom-hole assembly (BHA) was made up and deployed to 1187 meters below sea level (mbsl), and the top drive was picked up. Two "pigs" (pipe cleaning devices) were pumped through the drill string to remove some of the rust. Based on the precision depth recorder reading, the bit was spaced out to 1215 mbsl. The sinker bars and the core orientation tool were installed, and Hole U1553A was spudded at 2105 h on 15 January 2020. Mudline Core 1H arrived on deck at 2120 h, recovering 3.08 m. This established a seafloor depth of 1221.2 mbsl.

Coring continued with the APC system until a partial stroke was recorded on Core 15H at 127.5 mbsf. The XCB system was deployed for a single core (16X) to penetrate a 1.3 m hard interval. APC coring then continued until refusal at Core 20H, where a drillover and 100,000 lb of overpull were required to free the core barrel. The HLAPC system was then deployed until refusal at Core 22F, when a drillover and 100,000 lb of overpull were again required to free the core barrel.

The XCB was then deployed, reaching a total depth of 216.4 mbsf with Core 27X. This had been determined to be the final core for the hole prior to deploying the barrel. However, while cutting the core, the driller noticed an increase in top drive torque, and the hole was terminated prior to coring the full length. After recovering Core 27X, it was determined that the increase in torque was caused by a malfunction in the top drive shaft brake actuator. The brake had partially closed and overheated. The drill string was pulled to 1187 mbsl to allow the crew to replace the top drive brake. The bit cleared the seafloor at 2215 h on 16 January, ending Hole U1553A. The vessel was then offset 20 m east to prepare for Hole U1553B.

Table T1. Core summary, Site U1553. DRF = drilling depth below rig floor. Seafloor depth estimate method: APC_CALC = drill string length from rig floor to bit + length of extended APC core barrel – length of core recovered; OFFSET = seafloor depth adopted from previous hole. DSF = drilling depth below seafloor. Type: H = APC, F = half-length APC (HLAPC), X = extended core barrel (XCB), R = rotary core barrel (RCB). (Continued on next two pages.) **Download table in CSV format.**

Hole U1553A
Latitude: 52°13.4294′S
Longitude: 166°11.4801′E
Water depth (m): 1221.2
Date started (UTC): 2310 h; 14 January 2020
Date finished (UTC): 0915 h; 16 January 2020
Time on hole (days): 1.42
Seafloor depth DRF (m): 1232.5
Seafloor depth est. method: APC_CALC
Rig floor to sea level (m): 11.3
Penetration DSF (m): 216.4
Cored interval (m): 216.4
Recovered length (m): 214.03
Recovery (%): 98.9
Drilled interval (m): NA
Drilled interval (no.): 0
Total cores (no.): 27
APC cores (no.): 19
HLAPC cores (no.): 2
XCB cores (no.): 6
RCB cores (no.): 0
Other cores (no.): 0

Hole U1553B
Latitude: 52°13.4300′S
Longitude: 166°11.4964′E
Water depth (m): 1221.66
Date started (UTC): 0915 h; 16 January 2020
Date finished (UTC): 0345 h; 18 January 2020
Time on hole (days): 1.77
Seafloor depth DRF (m): 1233
Seafloor depth est. method: APC_CALC
Rig floor to sea level (m): 11.34
Penetration DSF (m): 243
Cored interval (m): 243
Recovered length (m): 231.91
Recovery (%): 95.44
Drilled interval (m): NA
Drilled interval (no.): 0
Total cores (no.): 29
APC cores (no.): 16
HLAPC cores (no.): 0
XCB cores (no.): 13
RCB cores (no.): 0
Other cores (no.): 0

Hole U1553C
Latitude: 52°13.4412′S
Longitude: 166°11.4975′E
Water depth (m): 1221.63
Date started (UTC): 0345 h; 18 January 2020
Date finished (UTC): 1430 h; 21 January 2020
Time on hole (days): 3.45
Seafloor depth DRF (m): 1233
Seafloor depth est. method: OFFSET
Rig floor to sea level (m): 11.37
Penetration DSF (m): 567.5
Cored interval (m): 333.5
Recovered length (m): 158.76
Recovery (%): 47.6
Drilled interval (m): 234
Drilled interval (no.): 1
Total cores (no.): 43
APC cores (no.): 0
HLAPC cores (no.): 0
XCB cores (no.): 0
RCB cores (no.): 43
Other cores (no.): 0

Hole U1553D
Latitude: 52°13.4403′S
Longitude: 166°11.4796′E
Water depth (m):1221.61
Date started (UTC): 1430 h; 21 January 2020
Date finished (UTC): 1255 h; 24 January 2020
Time on hole (days): 2.93
Seafloor depth DRF (m): 1233
Seafloor depth est. method: OFFSET
Rig floor to sea level (m): 11.39
Penetration DSF (m): 584.3
Cored interval (m): 184.9
Recovered length (m): 97.95
Recovery (%): 52.97
Drilled interval (m): 399.4
Drilled interval (no.): 1
Total cores (no.): 19
APC cores (no.): 0
HLAPC cores (no.): 0
XCB cores (no.): 0
RCB cores (no.): 19
Other cores (no.): 0

Hole U1553E
Latitude: 52°13.4409′S
Longitude: 166°11.4616′E
Water depth (m): 1221.26
Date started (UTC): 1255 h; 24 January 2020
Date finished (UTC): 2342 h; 25 January 2020
Time on hole (days): 1.45
Seafloor depth DRF (m): 1232.7
Seafloor depth est. method: APC_CALC
Rig floor to sea level (m): 11.44
Penetration DSF (m): 237.6
Cored interval (m): 237.6
Recovered length (m): 209.77
Recovery (%): 88.29
Drilled interval (m): NA
Drilled interval (no.): 0
Total cores (no.): 27
APC cores (no.): 15
HLAPC cores (no.): 0
XCB cores (no.): 12
RCB cores (no.): 0
Other cores (no.): 0

Core	Top of interval DSF (m)	Bottom of interval DSF (m)	Interval advanced (m)	Recovered length (m)	Curated length (m)	Core recovery (%)	Core on deck (2020)	Core on deck UTC (h)	Sections (*N*)
378-U1553A-									
1H	0.0	3.0	3.0	3.08	3.08	103	15 Jan	0820	3
2H	3.0	12.5	9.5	10.13	10.13	107	15 Jan	0900	8
3H	12.5	22.0	9.5	9.79	9.79	103	15 Jan	0940	8
4H	22.0	31.5	9.5	10.22	10.22	108	15 Jan	1030	8
5H	31.5	41.0	9.5	9.31	9.31	98	15 Jan	1130	8
6H	41.0	50.5	9.5	9.47	9.47	100	15 Jan	1210	8
7H	50.5	60.0	9.5	10.09	10.09	106	15 Jan	1310	8
8H	60.0	69.5	9.5	10.00	10.00	105	15 Jan	1355	8
9H	69.5	79.0	9.5	9.65	9.65	102	15 Jan	1440	8
10H	79.0	88.5	9.5	10.05	10.05	106	15 Jan	1545	8
11H	88.5	98.0	9.5	9.84	9.84	104	15 Jan	1630	8
12H	98.0	107.5	9.5	9.23	9.23	97	15 Jan	1715	8
13H	107.5	117.0	9.5	9.82	9.82	103	15 Jan	1800	8
14H	117.0	126.5	9.5	9.95	9.95	105	15 Jan	1915	8
15H	126.5	127.5	1.0	6.76	6.76	676	15 Jan	2000	6
16X	127.5	128.8	1.3	0.26	0.26	20	15 Jan	2055	1
17H	128.8	138.3	9.5	9.98	9.98	105	15 Jan	2130	8
18H	138.3	147.8	9.5	9.99	9.99	105	15 Jan	2215	8
19H	147.8	157.3	9.5	9.64	9.64	101	15 Jan	2255	8
20H	157.3	166.8	9.5	9.94	9.94	105	16 Jan	0055	8
21F	166.8	171.5	4.7	4.75	4.75	101	16 Jan	0150	4

Table T1 (continued). (Continued on next page.)

Core	Top of interval DSF (m)	Bottom of interval DSF (m)	Interval advanced (m)	Recovered length (m)	Curated length (m)	Core recovery (%)	Core on deck (2020)	Core on deck UTC (h)	Sections (*N*)
22F	171.5	176.2	4.7	4.59	4.59	98	16 Jan	0255	4
23X	176.2	179.4	3.2	3.23	3.23	101	16 Jan	0345	3
24X	179.4	189.1	9.7	5.84	5.84	60	16 Jan	0450	5
25X	189.1	198.8	9.7	7.74	7.74	80	16 Jan	0545	6
26X	198.8	208.6	9.8	5.10	5.10	52	16 Jan	0645	5
27X	208.6	216.4	7.8	5.58	5.58	72	16 Jan	0800	5
		Hole U1553A totals:	216.4	214.03	214.03				178
378-U1553B-									
1H	0.0	6.0	6.0	6.13	6.13	102	16 Jan	2220	5
2H	6.0	15.5	9.5	9.23	9.23	97	16 Jan	2255	7
3H	15.5	25.0	9.5	8.89	8.89	94	17 Jan	0040	7
4H	25.0	34.5	9.5	10.07	10.07	106	17 Jan	0135	8
5H	34.5	44.0	9.5	9.54	9.54	100	17 Jan	0220	8
6H	44.0	53.5	9.5	9.86	9.86	104	17 Jan	0255	8
7H	53.5	58.3	4.8	5.27	5.27	110	17 Jan	0350	5
8H	58.3	67.8	9.5	9.68	9.68	102	17 Jan	0440	8
9H	67.8	77.3	9.5	9.87	9.87	104	17 Jan	0525	8
10H	77.3	86.8	9.5	9.67	9.67	102	17 Jan	0605	8
11H	86.8	96.3	9.5	10.08	10.08	106	17 Jan	0640	8
12H	96.3	105.8	9.5	9.47	9.47	100	17 Jan	0715	8
13H	105.8	115.3	9.5	9.46	9.46	100	17 Jan	0755	8
14H	115.3	124.8	9.5	9.86	9.86	104	17 Jan	0835	8
15X	124.8	131.0	6.2	4.78	4.78	77	17 Jan	0950	4
16H	131.0	140.5	9.5	9.76	9.76	103	17 Jan	1025	8
17H	140.5	150.0	9.5	10.04	10.04	106	17 Jan	1150	8
18X	150.0	159.5	9.5	7.36	7.36	77	17 Jan	1325	6
19X	159.5	169.2	9.7	8.01	8.01	83	17 Jan	1420	7
20X	169.2	178.9	9.7	5.90	5.90	61	17 Jan	1510	5
21X	178.9	183.6	4.7	4.03	4.03	86	17 Jan	1545	4
22X	183.6	188.6	5.0	5.90	5.90	118	17 Jan	1620	5
23X	188.6	193.3	4.7	3.99	3.99	85	17 Jan	1700	4
24X	193.3	198.3	5.0	5.52	5.52	110	17 Jan	1740	5
25X	198.3	208.1	9.8	9.92	9.92	101	17 Jan	1830	8
26X	208.1	217.8	9.7	9.47	9.47	98	17 Jan	1920	8
27X	217.8	227.6	9.8	7.35	7.35	75	17 Jan	2025	6
28X	227.6	237.3	9.7	8.11	8.11	84	17 Jan	2125	7
29X	237.3	243.0	5.7	4.69	4.69	82	17 Jan	2300	4
		Hole U1553B totals:	243.0	231.91	231.91				193
378-U1553C-									
11	0.0	234.0	234.0		*****Drilled interval*****		18 Jan	2115	0
2R	234.0	243.7	9.7	2.90	2.90	30	18 Jan	2255	3
3R	243.7	253.4	9.7	2.17	2.17	22	19 Jan	0015	3
4R	253.4	263.2	9.8	2.33	2.33	24	19 Jan	0120	3
5R	263.2	273.0	9.8	2.65	2.65	27	19 Jan	0225	3
6R	273.0	278.0	5.0	4.80	4.80	96	19 Jan	0315	5
7R	278.0	282.7	4.7	2.00	2.00	43	19 Jan	0350	3
8R	282.7	292.4	9.7	3.34	3.34	34	19 Jan	0450	4
9R	292.4	297.6	5.2	3.20	3.20	62	19 Jan	0545	4
10R	297.6	302.1	4.5	1.63	1.63	36	19 Jan	0635	2
11R	302.1	306.9	4.8	0.45	0.45	9	19 Jan	0735	1
12R	306.9	311.9	5.0	2.85	2.85	57	19 Jan	0825	3
13R	311.9	316.7	4.8	4.20	4.20	88	19 Jan	0925	4
14R	316.7	321.6	4.9	2.52	2.52	51	19 Jan	1025	3
15R	321.6	326.3	4.7	3.93	3.93	84	19 Jan	1120	4
16R	326.3	331.3	5.0	4.46	4.46	89	19 Jan	1225	4
17R	331.3	341.0	9.7	7.29	7.29	75	19 Jan	1345	6
18R	341.0	350.7	9.7	3.42	3.42	35	19 Jan	1505	4
19R	350.7	355.4	4.7	2.06	2.06	44	19 Jan	1555	3
20R	355.4	360.4	5.0	0.17	0.17	3	19 Jan	1655	2
21R	360.4	370.2	9.8	4.25	4.25	43	19 Jan	1805	4
22R	370.2	379.9	9.7	4.25	4.25	44	19 Jan	1910	4
23R	379.9	389.6	9.7	3.45	3.45	36	19 Jan	2005	4
24R	389.6	399.4	9.8	2.27	2.27	23	19 Jan	2105	3
25R	399.4	409.1	9.7	4.58	4.58	47	19 Jan	2215	5
26R	409.1	418.8	9.7	3.37	3.37	35	19 Jan	2310	4
27R	418.8	428.6	9.8	2.95	2.95	30	20 Jan	0030	3
28R	428.6	438.3	9.7	8.90	8.90	92	20 Jan	0230	7
29R	438.3	443.0	4.7	5.37	5.37	114	20 Jan	0410	5
30R	443.0	448.0	5.0	4.95	4.95	99	20 Jan	0535	4

Table T1 (continued).

Core	Top of interval DSF (m)	Bottom of interval DSF (m)	Interval advanced (m)	Recovered length (m)	Curated length (m)	Core recovery (%)	Core on deck (2020)	Core on deck UTC (h)	Sections (*N*)
31R	448.0	452.8	4.8	3.37	3.37	70	20 Jan	0655	4
32R	452.8	457.8	5.0	5.31	5.31	106	20 Jan	0830	5
33R	457.8	467.5	9.7	4.36	4.36	45	20 Jan	1040	4
34R	467.5	477.2	9.7	2.36	2.36	24	20 Jan	1250	3
35R	477.2	487.0	9.8	3.75	3.75	38	20 Jan	1510	4
36R	487.0	496.7	9.7	1.13	1.13	12	20 Jan	1710	2
37R	496.7	506.4	9.7	1.25	1.25	13	20 Jan	1850	2
38R	506.4	516.1	9.7	1.20	1.20	12	20 Jan	2035	2
39R	516.1	525.9	9.8	1.88	1.88	19	20 Jan	2225	3
40R	525.9	535.6	9.7	2.26	2.26	23	21 Jan	0010	3
41R	535.6	545.4	9.8	7.10	7.10	72	21 Jan	0205	6
42R	545.4	555.1	9.7	10.45	10.45	108	21 Jan	0405	9
43R	555.1	564.8	9.7	12.40	12.40	128	21 Jan	0635	12
44R	564.8	567.5	2.7	1.23	1.23	46	21 Jan	0830	2
		Hole U1553C totals:	567.5	158.76	158.76				168
378-U1553D-									
11	0.0	399.4	399.4		*****Drilled interval*****		22 Jan	1840	0
2R	399.4	409.1	9.7	4.88	4.88	50	22 Jan	1950	5
3R	409.1	418.8	9.7	3.83	3.83	39	22 Jan	2110	4
4R	418.8	428.5	9.7	8.03	8.03	83	22 Jan	2230	7
5R	428.5	438.3	9.8	8.42	8.42	86	23 Jan	0010	7
6R	438.3	448.1	9.8	9.49	9.49	97	23 Jan	0250	8
7R	448.1	457.8	9.7	5.54	5.54	57	23 Jan	0550	5
8R	457.8	467.5	9.7	3.22	3.22	33	23 Jan	0805	3
9R	467.5	477.2	9.7	4.44	4.44	46	23 Jan	1025	4
10R	477.2	487.0	9.8	1.26	1.26	13	23 Jan	1250	2
11R	487.0	496.7	9.7	1.14	1.14	12	23 Jan	1520	2
12R	496.7	506.4	9.7	0.73	0.73	8	23 Jan	1715	2
13R	506.4	516.1	9.7	1.29	1.29	13	23 Jan	1900	2
14R	516.1	525.9	9.8	1.52	1.52	16	23 Jan	2040	2
15R	525.9	535.6	9.7	2.72	2.72	28	23 Jan	2225	3
16R	535.6	545.3	9.7	6.90	6.90	71	24 Jan	0000	6
17R	545.3	555.0	9.7	8.54	8.54	88	24 Jan	0150	7
18R	555.0	564.7	9.7	9.98	9.98	103	24 Jan	0345	8
19R	564.7	574.5	9.8	9.36	9.36	96	24 Jan	0550	8
20R	574.5	584.3	9.8	6.66	6.66	68	24 Jan	0830	6
		Hole U1553D totals:	584.3	97.95	97.95				91
378-U1553E-									
1H	0.0	8.3	8.3	8.29	8.29	100	24 Jan	2000	7
2H	8.3	17.8	9.5	9.84	9.84	104	24 Jan	2040	8
3H	17.8	27.3	9.5	9.05	9.05	95	24 Jan	2125	7
4H	27.3	36.8	9.5	9.43	9.43	99	24 Jan	2220	8
5H	36.8	41.6	4.8	5.57	5.57	116	24 Jan	2305	5
6H	41.6	51.1	9.5	9.50	9.50	100	24 Jan	2350	8
7H	51.1	57.4	6.3	4.53	4.53	72	25 Jan	0035	4
8H	57.4	66.9	9.5	9.36	9.36	99	25 Jan	0105	8
9H	66.9	76.4	9.5	9.56	9.56	101	25 Jan	0145	8
10H	76.4	85.9	9.5	9.64	9.64	101	25 Jan	0220	8
11H	85.9	90.9	5.0	4.90	4.90	98	25 Jan	0300	5
12H	90.9	100.4	9.5	9.49	9.49	100	25 Jan	0335	8
13H	100.4	109.9	9.5	8.56	8.56	90	25 Jan	0410	7
14H	109.9	119.4	9.5	9.92	9.92	104	25 Jan	0445	8
15X	119.4	129.1	9.7	6.08	6.08	63	25 Jan	0545	5
16H	129.1	138.6	9.5	10.02	10.02	105	25 Jan	0615	8
17X	138.6	148.4	9.8	8.38	8.38	86	25 Jan	0710	7
18X	148.4	158.2	9.8	9.66	9.66	99	25 Jan	0755	8
19X	158.2	168.0	9.8	5.35	5.35	55	25 Jan	0845	5
20X	168.0	177.8	9.8	4.85	4.85	49	25 Jan	0935	4
21X	177.8	183.3	5.5	5.39	5.39	98	25 Jan	1015	5
22X	183.3	188.8	5.5	4.38	4.38	80	25 Jan	1055	4
23X	188.8	198.6	9.8	6.59	6.59	67	25 Jan	1210	6
24X	198.6	208.4	9.8	7.56	7.56	77	25 Jan	1315	6
25X	208.4	218.1	9.7	5.90	5.90	61	25 Jan	1455	5
26X	218.1	227.9	9.8	9.82	9.82	100	25 Jan	1610	8
27X	227.9	237.6	9.7	8.15	8.15	84	25 Jan	1725	7
		Hole U1553E totals:	237.6	209.77	209.77				177
		Site U1553 totals:	1848.8	912.42	912.42				807

A total of 27 cores were taken from Hole U1553A over a 216.4 m interval with 98.9% recovery. Temperature measurements using the advanced piston corer temperature (APCT-3) tool were taken on Cores 4H, 7H, and 10H, and all full-length APC cores were oriented using the Icefield MI-5 core orientation tool. Total time on Hole U1553A was 34.00 h (1.4 days).

2.2.2. Hole U1553B

The top drive brake was repaired, and operations resumed at 0915 h on 17 January 2020. The top drive was picked up, and Hole U1553B was spudded at 1105 h on 17 January. The seafloor depth was calculated at 1221.7 mbsl based on recovery of the mudline in Core 378-U1553B-1H. Core 3H encountered a gravel layer and was a partial stroke. After a full 9.5 m advance, APC coring continued through Core 14H to 124.8 mbsf. The XCB system was then deployed for one core based on the hard interval encountered in Hole U1553A. Core 378-U1553B-15X advanced 6.2 m, and APC coring resumed through Core 17H to 150.0 mbsf.

To avoid stuck core barrels, which were encountered in Hole U1553A, the XCB system was deployed from 150.0 mbsf to the termination of coring at a total depth of 243.0 mbsf. The bit was then recovered, clearing the seafloor at 1350 h and the rig floor at 1645 h on 18 January and ending Hole U1553B. The vessel was then offset 20 m south for Hole U1553C.

A total of 29 cores were taken over a 243.0 m interval with 95.4% recovery. All full-length APC cores were oriented using the Icefield MI-5 core orientation tool. Total time on Hole U1553B was 42.50 h (1.8 days), with 10 h spent repairing the top drive.

2.2.3. Hole U1553C

With inclement weather systems moving in, the third APC/XCB hole was deferred in favor of an attempt to reach the deeper objectives with the rotary core barrel (RCB) system. A four-stand RCB BHA was made up and deployed to 1193 mbsl. Hole U1553C was spudded at 0010 h on 19 January 2020 and drilled ahead without core recovery to 234.0 mbsf. The center bit was pulled, and RCB coring began.

Half advances (~5 m) were used on Cores 378-U1553C-6R, 7R, 9R–16R, 19R, and 20R as a strategy to maximize recovery. Half advances also were used on Cores 29R–32R to optimize recovery of the PETM. Cores 40R–43R were cored without liners in the core barrel in an effort to improve recovery. An anomalously low C_1/C_2 hydrocarbon ratio in Core 43R caused Core 44R to be pulled after a 2.7 m advance to verify the values. With anomalously low C_1/C_2 ratios in consecutive cores, the decision was made to terminate coring at 567.5 mbsf. The bit was recovered to the surface and cleared the seafloor at 0105 h on 22 January, ending Hole U1553C. The vessel was offset 20 m west for Hole U1553D.

A total of 43 cores were taken over a 334.6 m interval with 47.4% recovery. Total depth for Hole U1553C was 567.5 mbsf, and total time was 82.75 h (3.4 days).

2.2.4. Hole U1553D

A new bit was installed on the RCB BHA, and it was deployed to 1193 mbsl to begin Hole U1553D. Hole U1553D was spudded at 0845 h on 22 January and drilled ahead to 178.3 mbsf. The center bit was pulled, and the Sediment Temperature 2 (SET2) tool was lowered to obtain a fourth temperature measurement with the goal of refining the thermal gradient at Site U1553.

After recovering the SET2 tool, the center bit was again deployed and the hole was drilled to 399.4 mbsf. The center bit was pulled, and the RCB system was deployed. Cores 378-U1553D-11R through 17R were cored without using liners to improve recovery.

During coring operations, clearance was provided by the Environmental Protection and Safety Panel to advance Hole U1553D deeper than Hole U1553C. This clearance was conditional and based on the need to wait for the results of headspace gas analysis prior to taking the next core. Coring was paused after Core 378-U1553D-19R to allow time for headspace gas analysis before proceeding. Coring was terminated at the Co-Chief Scientists' request after Core 20R at 584.3 mbsf to allow sufficient time for a fifth hole to provide triplicate recovery of the APC/XCB section recovered in Holes U1553A and U1553B. The bit was recovered and cleared the seafloor at 2355 h

on 24 January and the rotary table at 0255 h on 25 January, ending Hole U1553D. The vessel was offset 20 m west for Hole U1553E.

2.2.5. Hole U1553E

An APC/XCB BHA was made up and deployed to 1187 mbsl, and Hole U1553E was spudded at 0845 h on 25 January 2020. Based on recovery from Core 378-U1553E-1H, the seafloor was calculated at 1221.3 mbsl.

Coring continued with the APC system through Core 14H at 119.4 mbsf. One XCB core was taken from 119.4 to 129.1 mbsf to capture a hard interval encountered in Holes U1553A and U1553B. The APC system was then deployed for Core 378-U1553E-16H to 138.6 mbsf. The XCB was deployed from 138.6 to 237.6 mbsf, ending with Core 27X. Half advances were used on Cores 21X and 22X (177.8–188.8 mbsf) to improve recovery.

The drill string was recovered to the rig floor, and the bit cleared the seafloor at 0830 h on 26 January. The rig floor was secured for transit at 1215 h, and the vessel was switched from dynamic positioning mode at 1242 h, ending Hole U1553E and Site U1553.

A total of 27 cores were taken over a 237.6 m interval with 88.3% recovery. Total depth for Hole U1553E was 237.6 mbsf, and total time was 33.25 h (1.4 days). The total time spent at Site U1553 was 11.02 days, which includes 10 h lost because of breakdown.

The vessel then began the 531 nmi transit to Timaru, New Zealand, to pick up fuel filters before continuing to Papeete, Tahiti (French Polynesia). After the fuel filter transfer (tug *Hinewai*) at 1318 h on 28 January, the vessel began the 2564 nmi transit to Papeete. The detour to Timaru added ~13 h to the originally planned transit to Papeete. Expedition 378 officially ended with the first line ashore at 1312 h on 6 February local time (UTC – 10 h).

3. Lithostratigraphy

Coring at Site U1553 reached a maximum depth of 584.3 mbsf and recovered a 581.16 m long sedimentary succession of deep-sea sediment of Pleistocene and Oligocene to early Paleocene age from the Campbell Plateau. Five lithostratigraphic units were defined in the recovered sections on the basis of visual core description, smear slide and thin section analyses, and physical properties data (Figure **F2**). An interval of ~4 m of Pleistocene foraminifer-rich nannofossil ooze and foraminifer ooze (Unit I) overlies an expanded sequence (~200 m thick) of late Oligocene through early Oligocene nannofossil ooze with foraminifers (Unit II). The nannofossil ooze of Unit II gradually transitions into the nannofossil chalk of Unit III from ~175 to 225 mbsf. Lithification of carbonates increases downcore with chalk transitioning to limestone, defining Unit IV. Finally, the bottom ~100 m of the recovered sediment column contains siliciclastic Unit V, which is characterized by mudstone to dolomitic mudstone that is occasionally sandy. X-ray diffraction (XRD) analysis of samples from Holes U1553A–U1553D confirms the dominance of calcite at this site in the upper 470 m, followed by the dominance of quartz-bearing facies to the bottom of the hole.

3.1. Unit I

Intervals: 378-U1553A-1H-1, 0 cm, to 2H-1, 100 cm; 378-U1553B-1H-1, 0 cm, to 1H-3, 67 cm; 378-U1553E-1H-1, 0 cm, to 1H-3, 60 cm
Depths: Hole U1553A = 0–4.00 mbsf; Hole U1553B = 0–3.68 mbsf; Hole U1553E = 0–3.61 mbsf
Age: Pleistocene
Lithology: foraminifer-rich nannofossil ooze and nannofossil-rich foraminifer ooze

The top of Lithostratigraphic Unit I is defined by alternating white (and light greenish gray) foraminifer-rich nannofossil ooze and nannofossil-rich foraminifer ooze. A sharp color change from light greenish gray to white occurs in Section 378-U1553A-1H-1, 103 cm (Figure **F3**). In Section 1H-2, 30 cm, the sediment color begins to change from white and gray to (light) grayish olive, light olive-gray, and pale greenish yellow (Figure **F3**). This sediment color change is not associated with

a change in lithology; we infer that it likely reflects sedimentary redox conditions. Unit I is slightly bioturbated in some intervals. Smear slide observations found silt- to coarse sand–sized foraminifers and nannofossils (Figure **F4A**), the ratios of which fluctuated markedly with depth. XRD analysis of a bulk sediment sample (1H-2, 77–78 cm) reveals the presence of calcite and minor quartz and clay minerals (Figure **F5A**). In Holes U1553B and U1553E, Unit I is more disturbed (soupy) than in Hole U1553A and has fewer visible, sharp contacts between sediment color changes. The sharp, undulating boundary with Unit II is marked by a change in core color, which suggests an unconformity. This inference is supported by nannofossil species abundance, which indicates an abrupt transition from Pleistocene to Oligocene sediments at approximately 4 mbsf (see **Biostratigraphy and micropaleontology**).

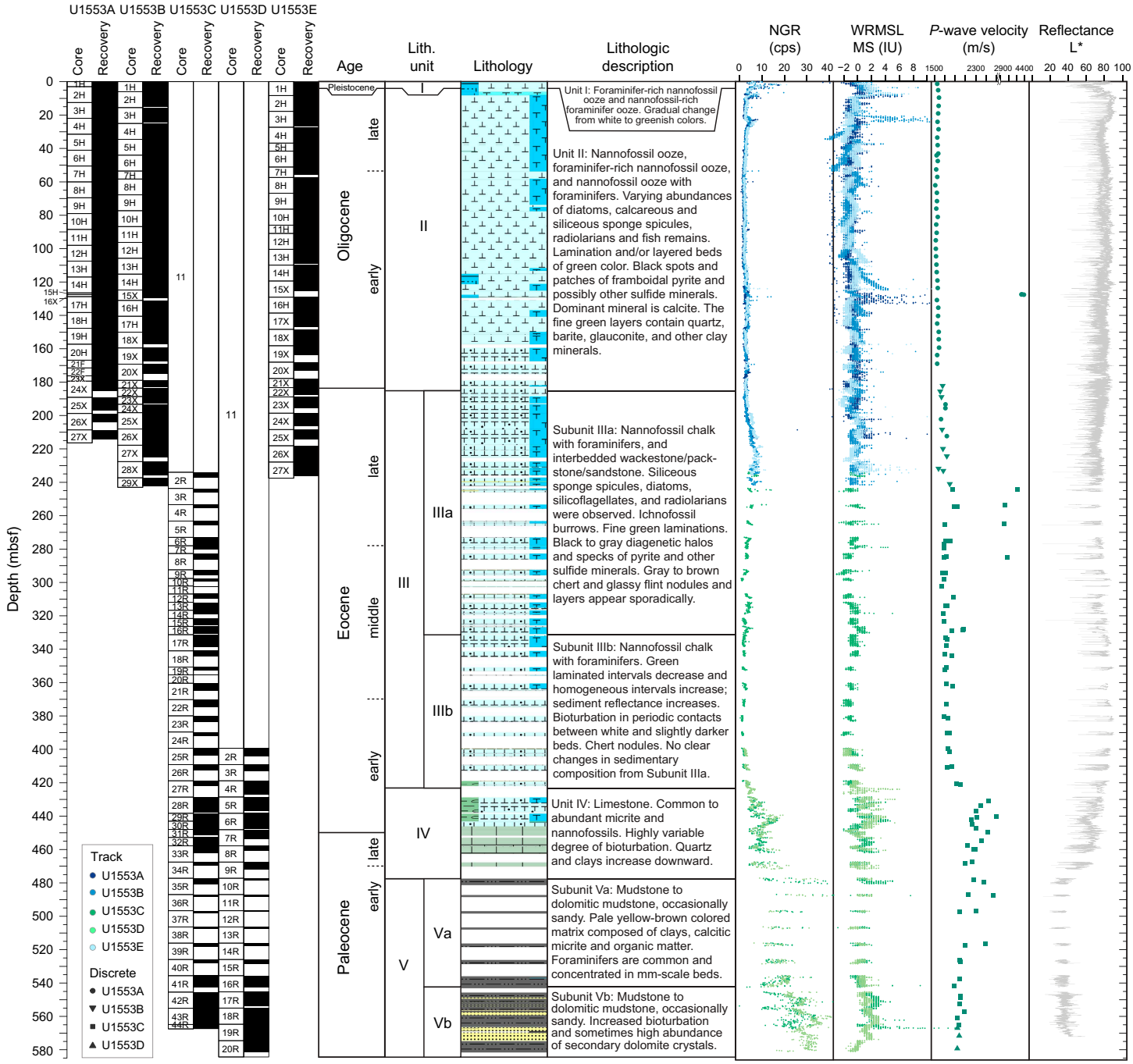

Figure F2. Lithologic summary, Site U1553. NGR = natural gamma radiation, WRMSL = Whole-Round Multisensor Logger, MS = magnetic susceptibility, cps = counts per second, IU = instrument units.

3.2. Unit II

Intervals: 378-U1553A-2H-1, 100 cm, to 24X-1, 58 cm; 378-U1553B-1H-3, 67 cm, to 22X-1, 150 cm; 378-U1553E-1H-3, 60 cm, to 20X-CC, 38 cm
Depths: Hole U1553A = 4.00–179.98 mbsf; Hole U1553B = 3.68–185.10 mbsf; Hole U1553E = 3.61–172.85 mbsf
Age: late Oligocene to early Oligocene (younger than 32.92 Ma)
Lithology: nannofossil ooze with varying abundances of foraminifers and radiolarians along with interbedded packstone/calcareous sandstone

Lithostratigraphic Unit II is a ~180 m thick succession of alternating nannofossil ooze, foraminifer-rich nannofossil ooze, and nannofossil ooze with foraminifers (Figures **F4B**, **F6**). The dominating colors in Unit II are light olive-gray, (light) greenish gray, and white. The most distinct features of Unit II are diffuse to well-defined millimeter- to centimeter-scale laminated and/or layered green beds that also display diagenetic alteration, which is manifested as colored halos (Figure **F6**). In Core 378-U1553E-3H, a transition occurs where yellow bands grade to the green color

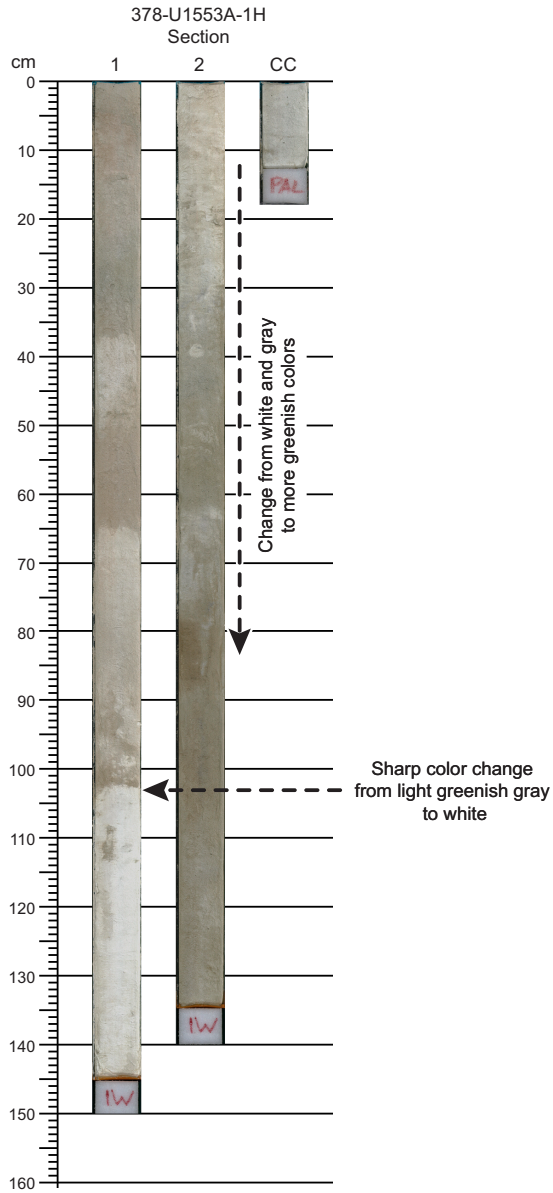

Figure F3. Characteristic lithology of Unit I, Core 378-U1553A-1H. Vertical dashed line = onset of sediment color change from white and gray to (light) grayish olive, light olive-gray, and pale greenish yellow.

seen throughout the rest of the hole (Figure F7). This feature is not present in Holes U1553A and U1553B. Smear slide observations found varying abundances of diatoms, calcareous and siliceous sponge spicules, radiolarians, and fish remains (Figure F8) and confirm that black spots and patches observable at the macroscopic scale can be attributed to the presence of pyrite framboids and possibly other sulfide minerals (Figure F9). Volcanic glass and rock fragments are found in smear slide analysis of Sample 378-U1553A-9H-1, 2 cm. From the top of Core 10H to the base of the unit, pyritized worm burrows and bioturbation are present. XRD analysis of bulk sediment samples from Unit II indicates that calcite dominates the minerals present. To increase the resolution of the secondary mineral assemblage present in this unit, a representative sample (378-U1553B-18X-CC, 15–17 cm) from a green layer was decalcified and analyzed using XRD (Figure F5B). Results indicate that the insoluble mineral fraction of the fine green layers includes quartz, barite, glauconite, and other clay minerals.

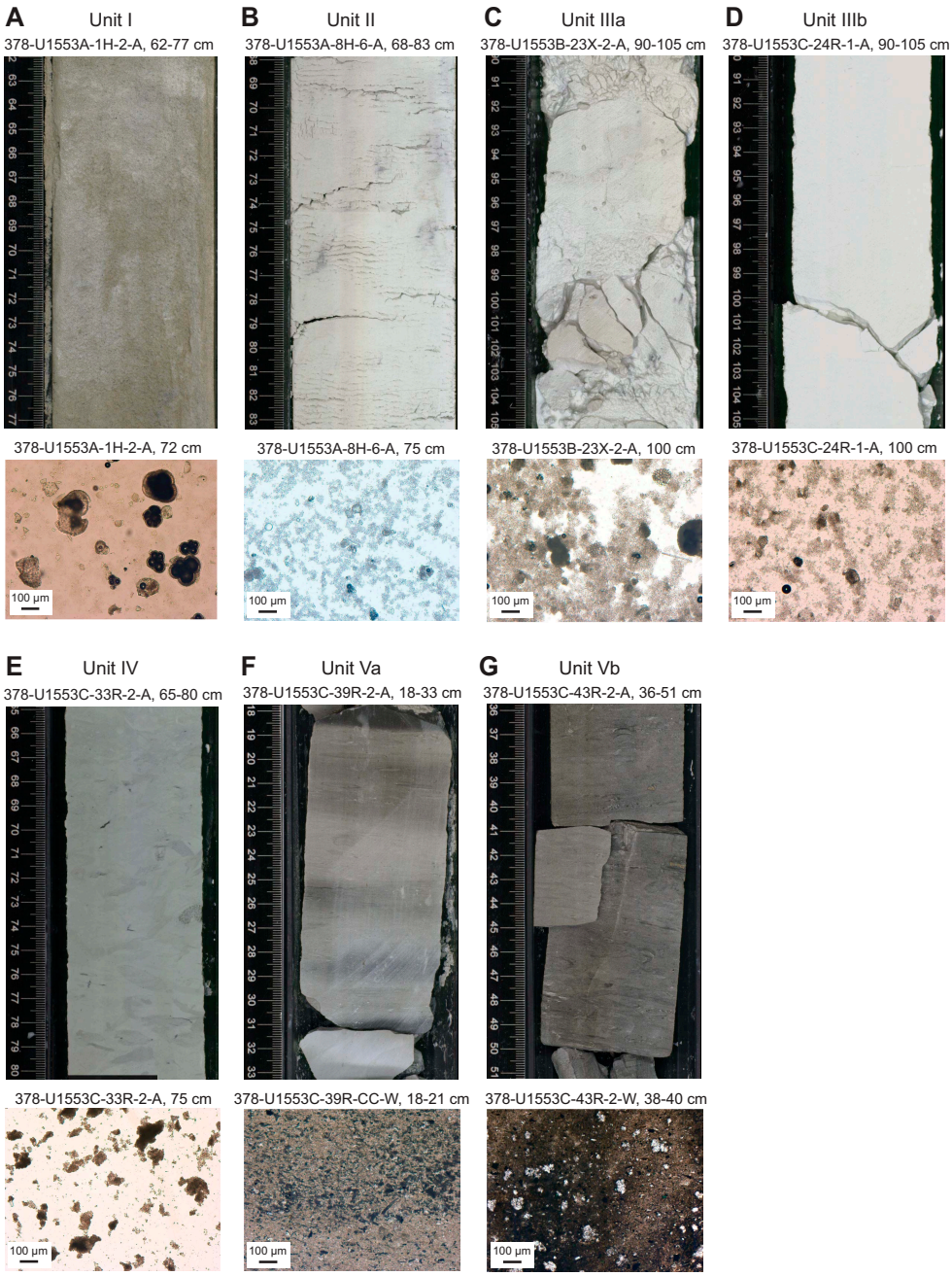

Figure F4. Representative lithologies of units and subunits, Holes U1553A–U1553C. (A–E) Smear slides and (F, G) thin sections in plane-polarized light.

In Unit II, a 10 cm bed of packstone and/or sandstone overlies a 5 cm bed of unlithified bluish gray medium sand between 128.97 and 129.02 mbsf in Hole U1553B (Core 15X) and between 124.00 and 124.16 mbsf in Hole U1553E (Core 15X) (Figure **F10A–F10C**). This early Oligocene (planktonic foraminifer Zone AO1) facies can be correlated between holes but was only partially recovered in Section 378-U1553A-16X-CC. The maximum magnetic susceptibility (MS) response is highest in medium sand (Figure **F10D**). The sand bed is composed of quartz, pyroxene, plagioclase, and rock fragments and is interpreted to be at least partially volcanic in origin. Thin section analysis of this facies in Section 16X-CC (127.52–127.76 mbsf) shows that this facies is

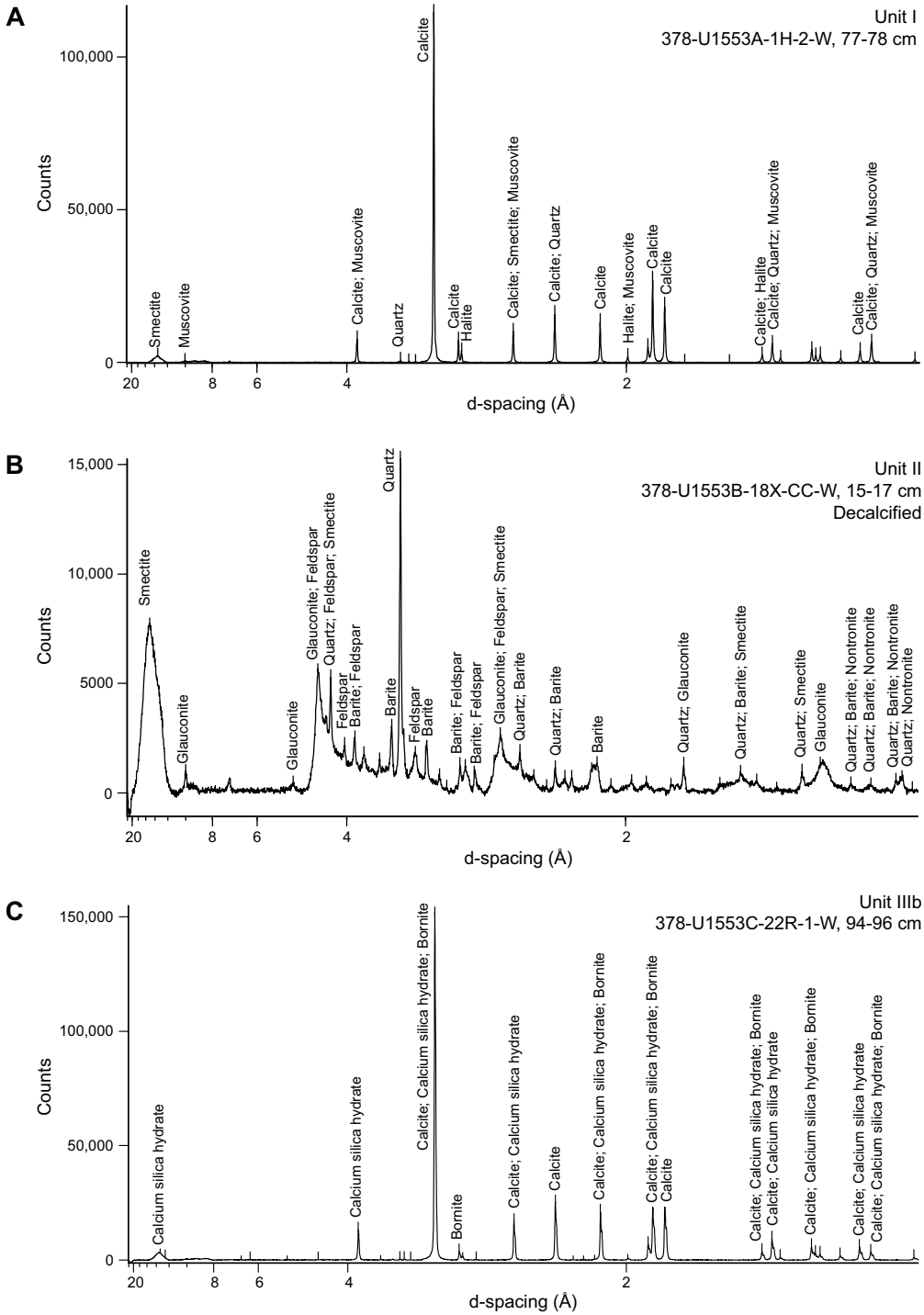

Figure F5. X-ray diffraction results for bulk sediment samples, Holes U1553A–U1553C. A. Unit I. B. Unit II. Sediment is decalcified. C. Subunit IIIb. (Continued on next page.)

packstone/sandstone. There is a gradational pattern between closely packed, rounded to subrounded sand-sized quartz grains (sandstone fabric) and a microfossil-rich packstone fabric across the three thin sections (127.50–127.73 mbsf). Foraminifer shells are abundant and are often filled with glauconite or pyrite/metal sulfide. Rounded glauconite grains are also visible in this facies. In thin sections from Sample 378-U1553B-15X-3, 110–112 cm (128.91–128.93 mbsf), a calcareous sandstone composed of mainly large, well-sorted, and rounded quartz grains (60%) superimposed on a fine matrix of unidentified calcareous fossils and clays is present (Figure **F10E**). Other framework grains include feldspar (mainly microcline) that is partially replaced by clay minerals and carbonate, zeolites as infilling of pore spaces, and minor quantities of muscovite.

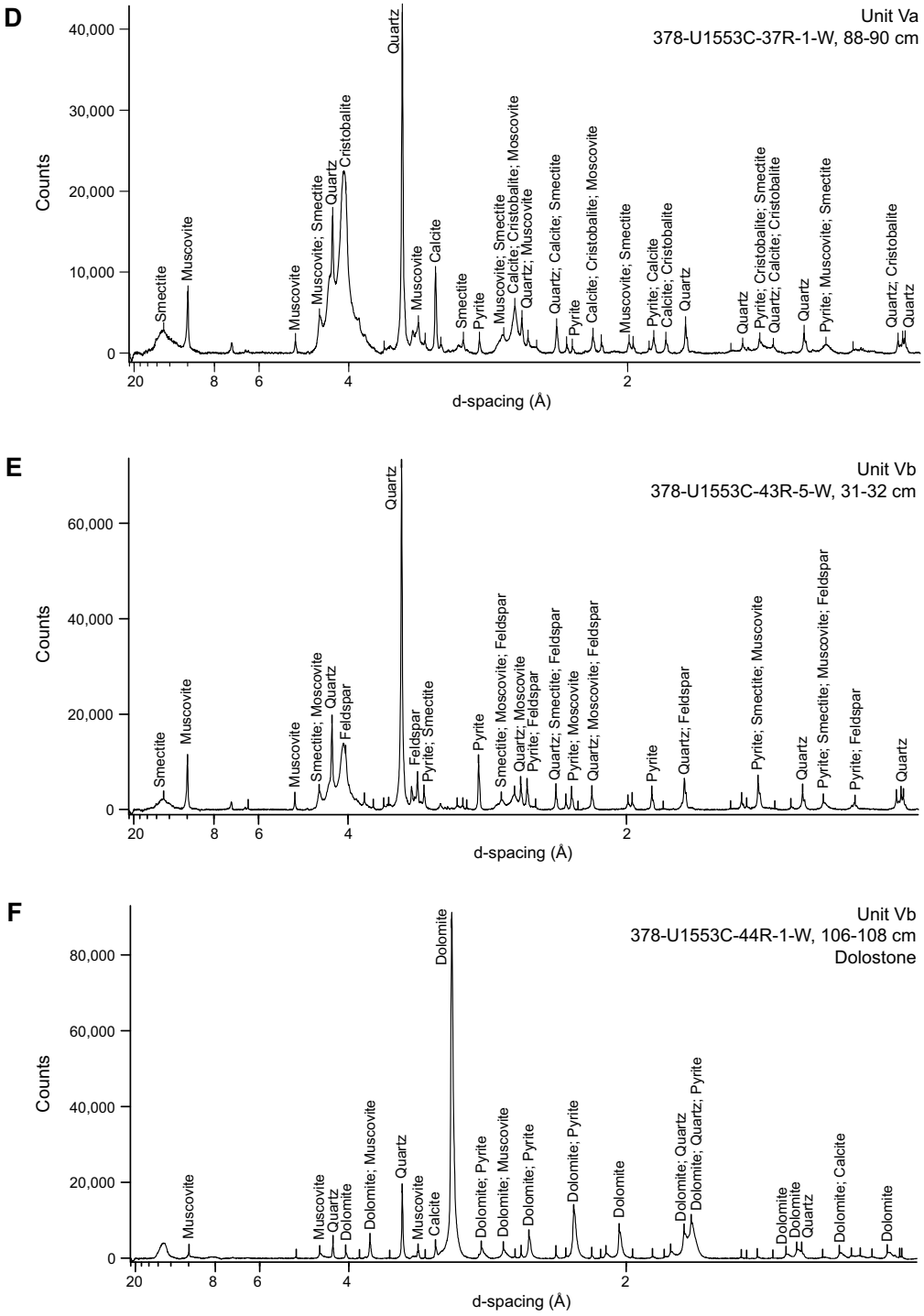

Figure F5 (continued). D. Subunit Va. E, F. Subunit Vb.

3.3. Unit III

Intervals: 378-U1553A-24X-1, 58 cm, to 27X-CC, 38 cm (bottom of hole [BOH]); 378-U1553B-22X-2, 0 cm, to 29X-CC, 34 cm (BOH); 378-U1553C-2R-1, 0 cm, to 27R-1, 46 cm; 378-U1553D-2R-1, 0 cm, to 4R-3, 82 cm; 378-U1553E-21X-1, 0 cm, to 27X-CC, 32 cm (BOH)
Depths: Hole U1553A = 179.98–214.18 mbsf; Hole U1553B = 185.10–241.99 mbsf; Hole U1553C = 234.00–419.26 mbsf (0–234 mbsf = drilled interval); Hole U1553D = 399.4–423.16 mbsf (0–399.4 mbsf = drilled interval); Hole U1553E = 177.80–236.00 mbsf
Age: late Eocene to early Eocene (~34 to ~52 Ma)
Lithology: nannofossil chalk with foraminifers along with interbedded wackestone/packstone/sandstone

Lithostratigraphic Unit III is defined as the transition from ooze to chalk, which occurs in foraminiferal Zone AO1 in the early Oligocene (see **Biostratigraphy and micropaleontology**). The exact boundary between Units II and III is based on physical properties (Figure **F2**). Reflectance data (a decrease in lightness [L*] and red-green-blue [RGB] color space values) were employed alongside *P*-wave velocity and natural gamma radiation (NGR) counts to define this boundary. This unit is divided into Subunits IIIa and IIIb at the top of Section 378-U1553C-17X-1. In Hole U1553D, Subunit IIIb was encountered in Section 2R-1.

3.3.1. Subunit IIIa

Intervals: 378-U1553A-24X-1, 58 cm, to 27X-CC, 38 cm (BOH); 378-U1553B-22X-2, 0 cm, to 29X-CC, 34 cm (BOH); 378-U1553C-2R-1, 0 cm, to 16R-CC, 19 cm; 378-U1553E-21X-1, 0 cm, to 27X-CC, 37 cm (BOH)
Depths: Hole U1553A = 179.98–214.18 mbsf; Hole U1553B = 183.6–241.99 mbsf; Hole U1553C = 234.00–330.76 mbsf; Hole U1553E = 177.80–236.05 mbsf
Age: late Eocene to middle Eocene (~34 to ~42 Ma)
Lithology: nannofossil chalk with foraminifers as well as interbedded wackestone/packstone/sandstone

The stiffness of Lithostratigraphic Subunit IIIa varies, ranging from soft and disturbed (drilling biscuits interbedded with softer disturbed sediment; Figure **F4C**) to a stiff fabric that required core splitting with a saw. Drilling disturbance increases downcore in Subunit IIIa and includes slight to severe fracturing and biscuiting of soft, brecciated material between harder sections of sediment (Figure **F11A–F11D**). Biscuiting is particularly severe in Hole U1553E. Lithification in-

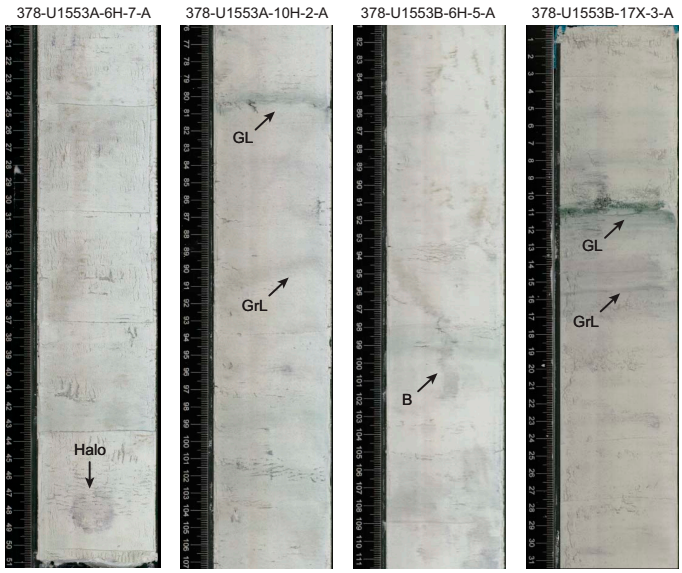

Figure F6. Characteristic lithologies in Unit II, Holes U1553A and U1553B. Halo = diagenetic halo, GL = green layers, GrL = gray layers, B = burrow.

creases downcore throughout Unit III and is associated with secondary calcite growth (see **Biostratigraphy and micropaleontology**) and the appearance of calcium silicate hydrate in XRD analysis (Figure **F5C**). Noncalcareous biogenic sediment containing siliceous sponge spicules, diatoms, silicoflagellates, and radiolarians was observed in low abundance in smear slides (1%–10%) throughout this subunit (Figure **F8**). Ichnofossil burrows (including *Teichichnus* type) are clearly visible in the lower portion of this subunit, indicating the degree of bioturbation (Figure **F11B**). Fine, millimeter-scale green laminations are also characteristic of this subunit, and they sometimes crosscut lateral ichnofossils (Figure **F12A**); other vertical burrows crosscut the laminations (Figure **F12B**). In addition, black to gray diagenetic halos and millimeter-sized specks of pyrite and other metal sulfides are visible throughout Subunit IIIa (Figure **F11B**). Gray to brown chert nodules and layers appear sporadically throughout this subunit (Figure **F11C**). The extent of silicification is variable, ranging from pale brown to gray, in which trace fossils are still visible (e.g., interval 378-U1553C-5R-2, 46–106 cm; 264.94–265.54 mbsf), to dark olive-gray, glassy flint (e.g., interval 9R-2, 73–76 cm; 294.63–294.66 mbsf).

Coarse-grained siliciclastics are interbedded in chalk in Holes U1553B and U1553C between ~230 and 255 mbsf (e.g., Figure **F11D**). A 3 cm thin section at the base of Hole U1553B in a thick layer

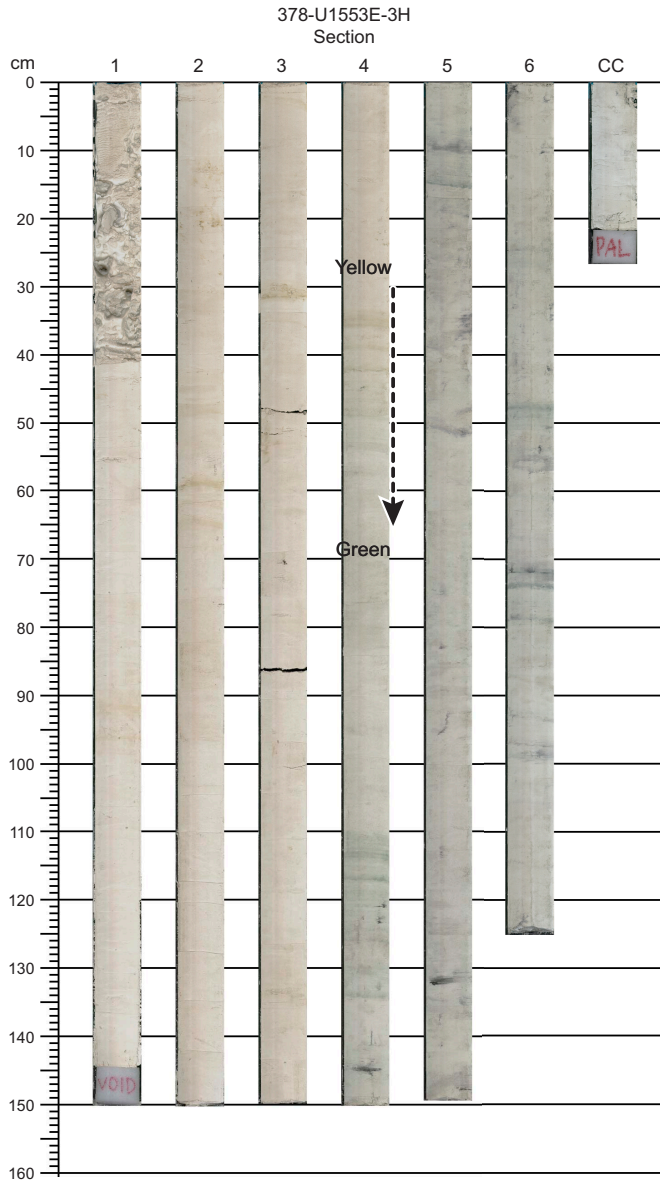

Figure F7. Sediment color change from yellow to green, Core 378-U1553E-3H.

of gray, fine-grained rock identified as wackestone (Sample 29X-CC, 31–34 cm; 241.96–241.99 mbsf) is dominantly carbonate bioclasts and jagged, angular quartz grains in a brownish matrix of micritic carbonate (Figure **F13**). In Hole U1553C, three packstone or sandstone intervals are present (Sections 3R-1, 3R-2, and 4R-1). In interval 3R-1, 75–108 cm (244.45–244.78 mbsf), a 14 cm thick packstone overlies a 19 cm thick carbonate-rich sandstone, and both are slightly bedded (Figure **F14A**). The packstone is very poorly sorted and contains carbonate bioclasts and quartz, plagioclase, chert, and glauconite. Some of the quartz grains are large (650 µm) and typically well rounded, but much of the matrix is highly angular. The medium-grained sandstone (Figure **F14A**) contains well-rounded and highly fractured and altered quartz, feldspar, chert, and carbonate bioclasts with a 1–3 µm micritic matrix (Figure **F14B–F14E**). An analogous 13 cm thick carbonate-rich sandstone is present in interval 3R-2, 36–49 cm (245.14–245.27 mbsf),and a comparable 18 cm thick packstone is present in interval 4R-1, 3–21 cm (253.43–253.61 mbsf).

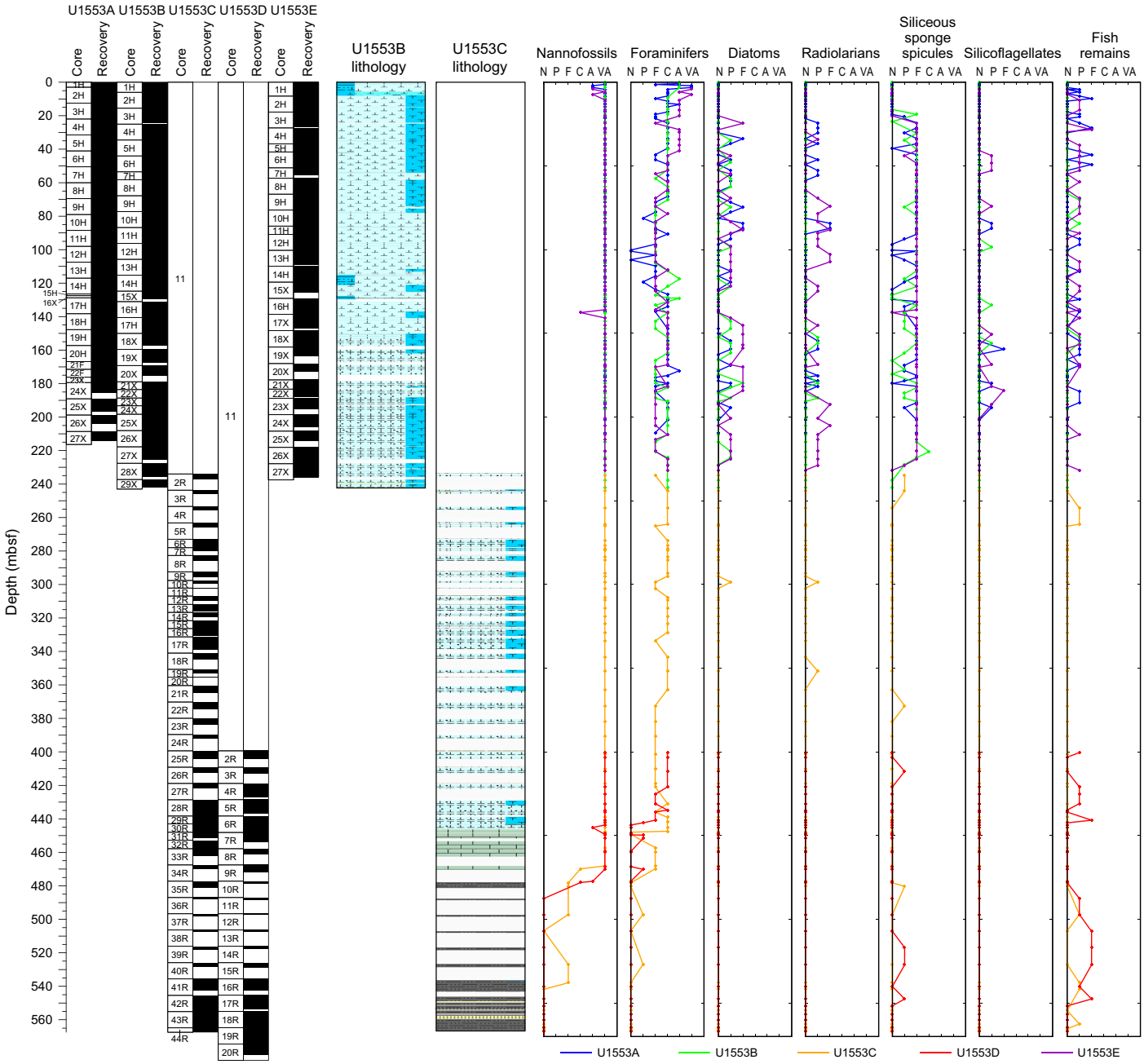

Figure F8. Abundance of selected components in smear slide observations, Site U1553. VA = very abundant (>50%), A = abundant (25%–50%), C = common (10%–25%), F = few (1%–10%), P = present (<1%), N = not observed (0%).

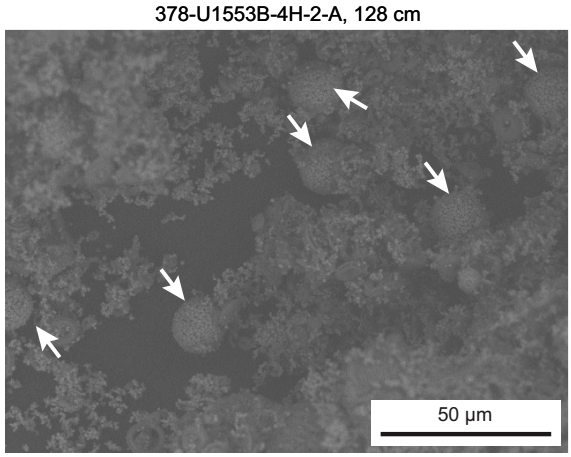

Figure F9. Framboidal pyrites (white arrows) in Unit II, Hole U1553B.

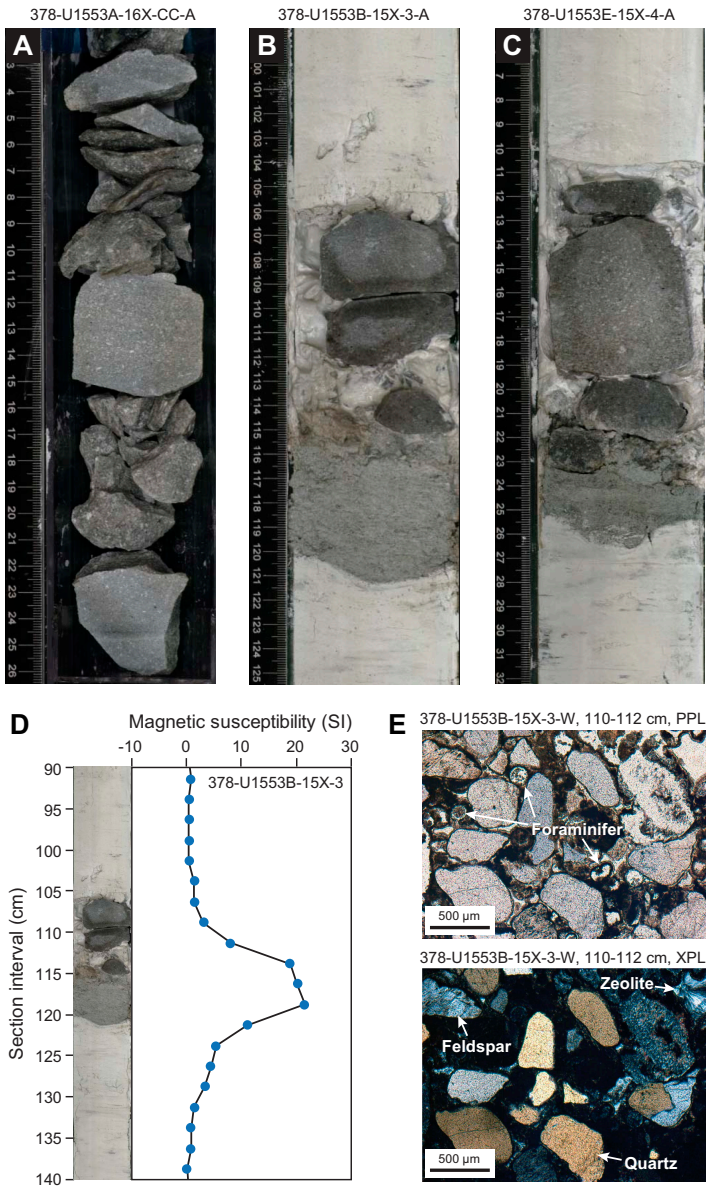

Figure F10. A–E. Indurated rocks (packstone and calcareous sandstone) in Unit II, Holes U1553A, U1553B, and U1553E. PPL = plane-polarized light, XPL = cross-polarized light.

3.3.2. Subunit IIIb

Intervals: 378-U1553C-17R-1, 0 cm, to 27R-1, 46 cm; 378-U1553D-2R-1, 0 cm, to 4R-3, 82 cm
Depths: Hole U1553C = 331.30–419.26 mbsf; Hole U1553D = 399.4–422.48 mbsf
Age: late Eocene to early Eocene (~42 to ~52 Ma)
Lithology: nannofossil chalk with foraminifers

Lithostratigraphic Subunit IIIb is distinguished by a reduction in green laminated intervals and an increase in intervals of bright white homogeneous sediments (Figure **F11F**). This increase in sediment lightness was visible using the Munsell color system and in RGB and L* values beginning at the top of Core 378-U1553C-17X (Figure **F2**). These white sediments are interrupted by periodic

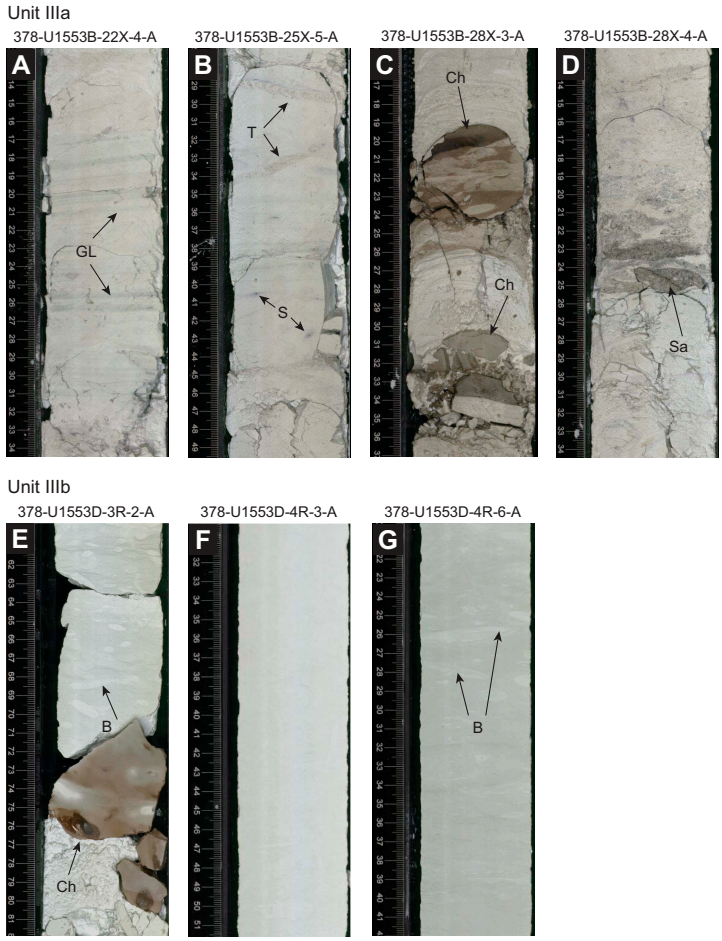

Figure F11. Characteristic lithologies in Unit III, Holes U1553B and U1553D. A–D. Subunit IIIa shows a consistent presence of green laminations (GL) and thin beds, *Teichichnus*-type trace fossils (T), sulfides (S), chert (Ch), and sandstone (Sa). E–G. Subunit IIIb is characterized by a transition to (F) bright white (N 9.5), homogeneous sediment in which bioturbation is expressed as green and white beds with burrows (B).

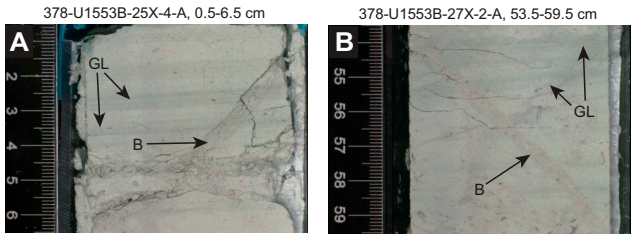

Figure F12. Trace fossil burrows (B) cutting green layers (GL) in Unit III, Hole U1553B. A. Green layers overprint the burrow, suggesting a diagenetic origin of the green layers. B. Burrow cuts across the green layers.

decimeter-scale beds of a slightly darker light greenish gray color. Bioturbation is visible in periodic contacts between white and slightly darker beds (Figure **F11G**). Tan to gray chert nodules are also present in this subunit (Figure **F11E**). Smear slide analyses do not indicate any clear changes in sedimentary composition in this subunit compared to Subunit IIIa (Figures **F4**, **F8**). However, X-ray fluorescence (XRF) analysis found an increase in Ca from 41.8% to 43.6% and minimum $CaCO_3$ weight percent (wt%) increases from Subunit IIIa (88 wt%) to Subunit IIIb (93 wt%) (see **Geochemistry**). XRD analysis of Unit III sediments validates the continued dominance of calcite. However, minor contributions from Fe-sulfides associated with other metals such as Cu (bornite) appear in XRD analyses (Figure **F5C**) in addition to glauconite and glaucophane.

3.4. Unit IV

Intervals: 378-U1553C-27R-1, 46 cm, to 34R-CC, 29 cm; 378-U1553D-4R-3, 82 cm, to 10R-1, 16 cm
Depths: Hole U1553C = 419.26–469.86 mbsf; Hole U1553D = 422.48–477.36 mbsf
Age: early Eocene to late Paleocene (~52–62 Ma)
Lithology: limestone

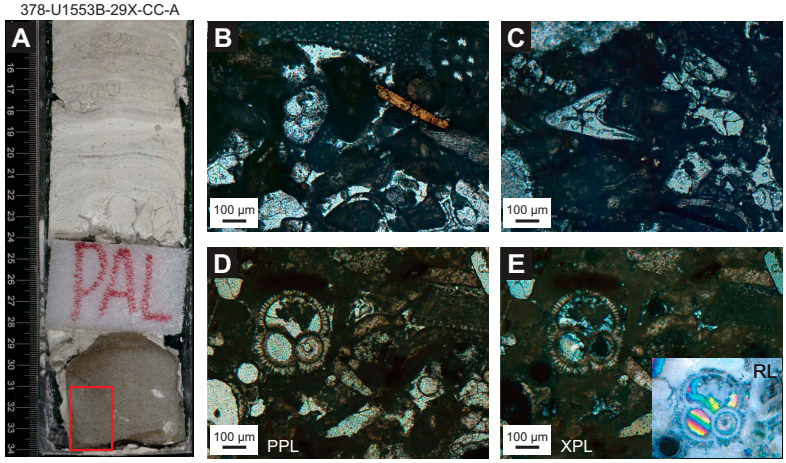

Figure F13. Wackestone, Sample 378-U1553B-29X-CC, 31–34 cm (241.96–241.99 mbsf). A. Location of wackestone thin section. B, C. Bioclasts in PPL. D, E. Foraminifer fossil in (D) PPL and (E) XPL. Inset in E shows the same fossil in reflected light (RL), highlighting the likely carbonate cement partially infilling the shell.

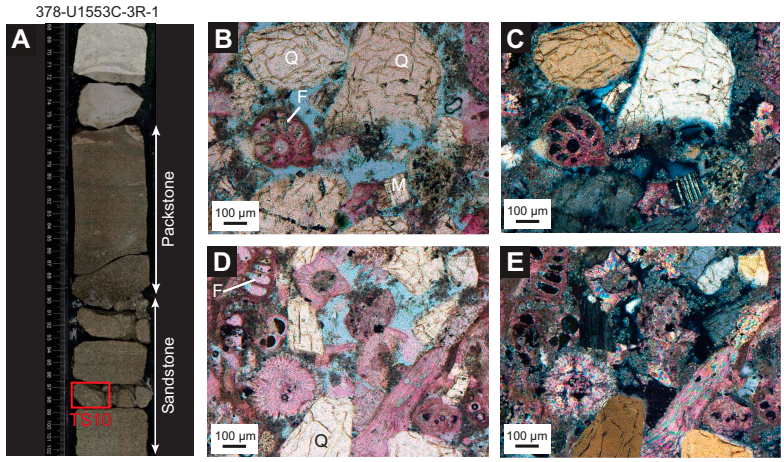

Figure F14. Sandstone, Sample 378-U1553C-3R-1, 96–98 cm (244.66–244.68 mbsf). The thin section was stained by potassium ferricyanide and Alizarin Red S to identify carbonates and impregnated with blue dye to show porosity. A. Thin section in the calcareous sandstone unit, which underlies 14 cm thick packstone. B–E. Bioclasts, including foraminifers (F) composed of calcite, rounded and fractured quartz grains (Q), microcline feldspar (M), and pale blue porosity between the framework grains. (B, D) PPL. (C, E) XPL.

Lithostratigraphic Unit IV is distinguished from Unit III by increased lithification of the limestone facies (Figure **F2**). Sediments are white to pale grayish green (Figure **F4E**) and tend to alternate in decimeter-scale beds. Boundary contacts range from sharp to gradational. A characteristic feature of this unit is the highly variable degree of bioturbation (slight to heavy; Figure **F15**). In Sections 378-U1553C-29R-2 and 378-U1553D-6R-4, sediments darken to a blue-gray hue and are increasingly lithified (Figure **F15**). Smear slide analyses from this interval show the presence of common to abundant micrite and nannofossils as well as quartz, micas, and ferromagnesian minerals (Figure **F8**). Throughout Unit IV, $CaCO_3$ values decrease from 90 to 63 wt% as the facies' color darkens (Figure **F15**) (see **Geochemistry**). XRD analysis also indicates an increase in quartz and other siliciclastic inputs, such as clays, toward the base of the unit, although calcite remains the dominant mineral. A thin section from a limestone in Section 378-U1553C-34R-1 stained with potas-

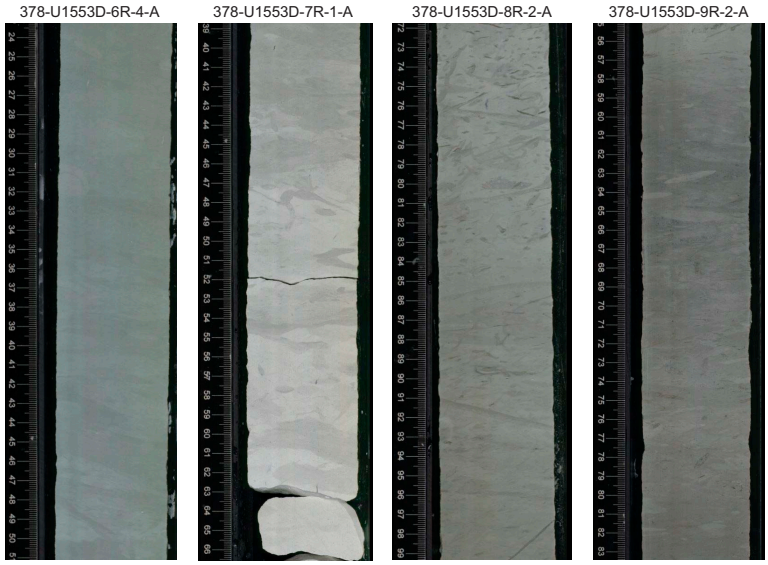

Figure F15. Characteristic lithologies in Unit IV, Hole U1553D. Gradation of colors from blue-gray and white to increasingly gray with decreased $CaCO_3$ wt% can be observed from left to right.

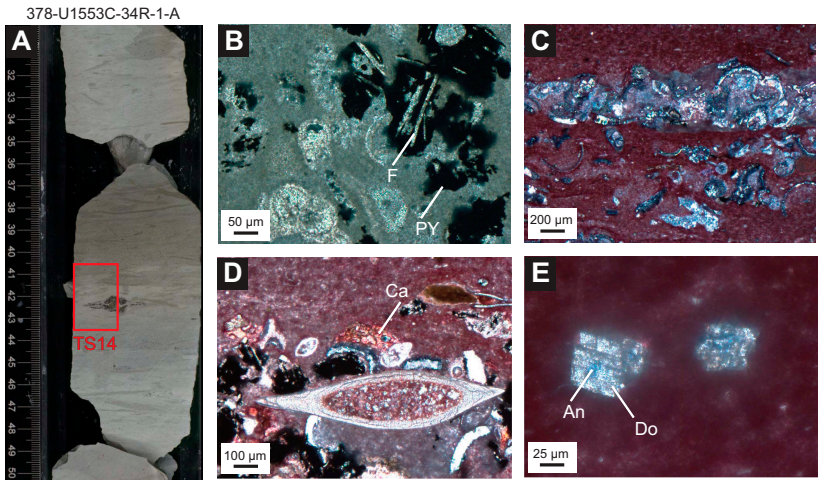

Figure F16. Limestone, Sample 378-U1553C-34R-1, 40–43 cm (467.90–467.93 mbsf). Thin section was partially stained by potassium ferricyanide and Alizarin Red S to identify carbonates. A. Location of limestone thin section (see Core descriptions). B. Unstained limestone with pyrite (PY) enclosing long fibrous mineral (F), which is colorless and has low birefringence (possibly zeolite?) (PPL). C. Matrix is stained purple, so it is ferroan calcite; microfossils mainly have no stain, so they are composed of dolomite (XPL). D. Lenticular bioclast composed of dolomite walls and ferroan calcite interior (XPL). Small areas of nonferroan calcite (Ca; pink) are also visible. E. Small (~50 µm) dolomite (Do) rhombs that have a ferroan dolomite or ankerite (An) core (turquoise) (PPL).

sium ferricyanide and Alizarin Red S shows that the matrix is composed of ferroan calcite and that most of the microfossils are composed of dolomite (Figure **F16**). There are some small (20–50 µm) secondary dolomite rhombs in the matrix, a few of which have a little blue color in their core from the carbonate stain, which indicates the presence of ferroan dolomite or ankerite (Figure **F16E**).

The onset of the PETM occurs in Unit IV in Cores 378-U1553C-31R and 378-U1553D-7R at approximately 449.5 mbsf. The PETM is tentatively related to the sharp boundary between a white, nonbioturbated interval and a darker green interval with white burrows (Figure **F17**).

3.5. Unit V

Intervals: 378-U1553C-35R-1, 0 cm, to 44R-CC, 5 cm (BOH); 378-U1553D-10R-1, 16 cm, to 20R-CC, 5 cm (BOH)
Depths: Hole U1553C = 477.20–566.03 mbsf; Hole U1553D = 477.36–581.16 mbsf
Age: Paleocene (older than 62 Ma)
Lithology: mudstone to dolomitic mudstone, occasionally sandy

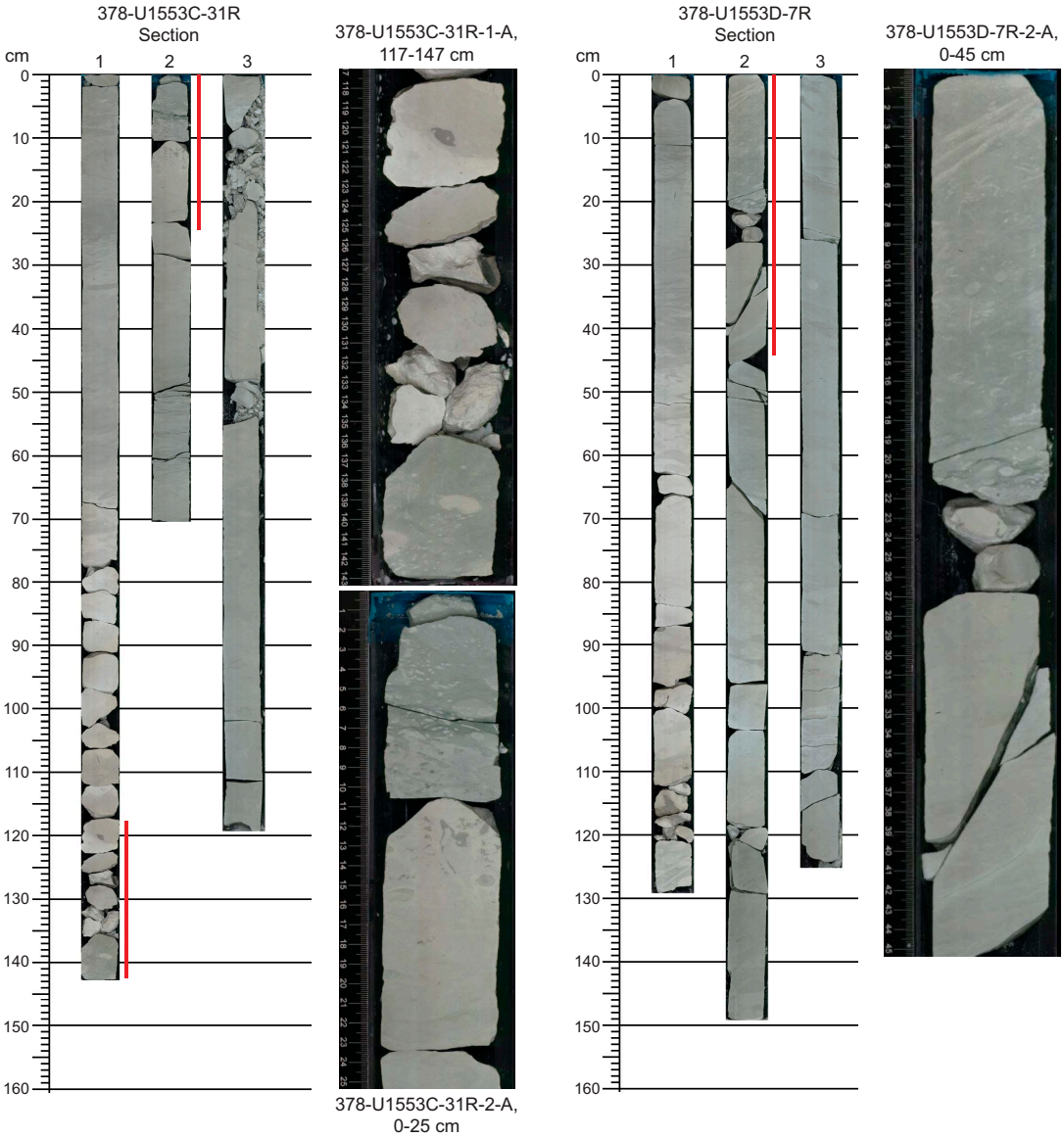

Figure F17. Paleocene/Eocene Thermal Maximum interval, Holes U1553C and U1553D. Red lines next to the cores indicate the enlarged area.

Splitting cores from Lithostratigraphic Unit V in Holes U1553C and U1553D resulted in a detectable hydrocarbon odor, which generally became more pronounced in the deeper cores. Directly after splitting Section 378-U1553D-20R-1 and before washing the split-core surfaces, an ultraviolet light revealed a bright purple fluorescence on the split-core surfaces (Figure **F18**).

The standard procedure for imaging archive section halves is to do so immediately after splitting once the surface water from the saw has dried (generally about 30 min) (see **Lithostratigraphy** in the Expedition 378 methods chapter [Röhl et al., 2022]). This procedure was followed for all Unit V cores, resulting in an initial set of very dark core images. It was noticed during core description that progressive drying of section halves from Unit V resulted in substantial color changes over a span of >24 h. The initially very dark core gradually became more reflective and variable in color, revealing more observable sedimentological features. Each section was consequently reimaged after drying for ~24 h (see **Lithostratigraphy** in the Expedition 378 methods chapter [Röhl et al., 2022]).

Unit V is a dominantly siliciclastic unit. Macroscopic determination of lithology for this unit is challenging, and shipboard assessment benefited from XRD and XRF analyses and thin section petrography. XRD analysis demonstrated a change in dominant mineral composition from calcite in Unit IV to quartz with associated clays and muscovite (Figure **F5**) that also was observable in smear slides and thin sections (Figure **F4F, F4G**). In accordance with the change in sediment color from the upper carbonate units, $CaCO_3$ abundance is low and varies from below the detection limit to 8.7 wt% with an average of 1.8 wt% (see **Geochemistry**). Microcrystalline pyrite is abundant throughout this unit and often forms on/in fracture surfaces, as confirmed by XRD analysis (Figure **F19**). Thin section analysis indicates a high heterogeneity of sediment fabrics and components in this unit. Unit V is generally characterized by a brownish silt to clay-sized matrix that supports varying numbers of pyrite crystals, quartz and other siliciclastics, glauconite, and siliceous and calcareous microfossils (Figure **F5D–F5F**). Clastic components range from silt to very fine sand sized. Dolomite crystals 50–200 µm in size are abundant (Figures **F19A**, **F20E**) and often appear as sand-sized grains in hand sample. Varying degrees of pink staining from potassium ferricyanide and Alizarin Red S indicate the presence of a varying but low abundance of calcite in the matrix, probably as micrite. Therefore, the dominant classification given to this unit is mudstone to dolomitic mudstone. Significant differences in bioturbation fabrics and the presence of large (centimeter-sized), diagenetically modified areas have motivated the distinction of Lithostratigraphic Subunits Va and Vb (Figure **F21**).

3.5.1. Subunit Va

Intervals: 378-U1553C-35R-1, 0 cm, to 41R-CC, 15 cm; 378-U1553D-10R-1, 16 cm, to 16R-CC, 16 cm
Depths: Hole U1553C = 477.20–542.7 mbsf; Hole U1553D = 477.36–542.5 mbsf
Age: Paleocene (older than 62 Ma)
Lithology: mudstone to dolomitic mudstone, occasionally sandy

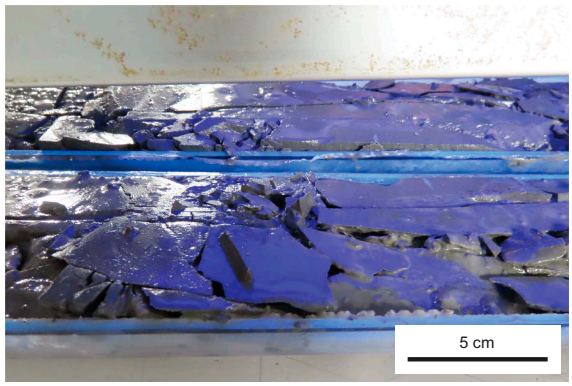

Figure F18. UV light illumination immediately after splitting, Section 378-U1553D-20R-1. Bright purple fluorescence is apparent on split core surfaces.

Lithostratigraphic Subunit Va is characterized as mudstone that is sometimes carbonate rich, with some fine to medium sandy intervals. After drying, the dominant color is medium gray to light gray (Figure **F21A–F21B**). Throughout this subunit, there are darker gray, centimeter-sized diagenetically modified areas against the lighter gray matrix. These are attributed to chert nodules. This was not confirmed by thin section microscopy, but it is supported by the XRD observation of amorphous SiO_2 (cristobalite) associated with opal-C (Figure **F5D**). Bioturbation is generally categorized as slight to moderate in Subunit Va. The $CaCO_3$ content averages 3.9 wt% for Subunit Va (see **Geochemistry**). This is supported by XRF (Ca = 2.0%) and XRD analyses, which identified a minor contribution from calcite (Figure **F5D**). The presence of *Bathysiphon* foraminifers indicates an upper bathyal depositional environment (see **Biostratigraphy and micropaleontology**). Foraminifers are common and can be concentrated in millimeter-scale beds, which is interpreted to indicate deposition by currents.

Thin section microscopy of three samples from Subunit Va indicates that the matrix of the mudstones is pale yellow brown (Figure **F20**) and mainly composed of clays, a calcitic micrite, and organic matter. Staining with potassium ferricyanide and Alizarin Red S produced a pale pink color in the matrix that is consistent with the presence of calcite (Figure **F20B**). Glauconite is usually present as distinct, isolated grains (Figure **F20A**) and has an abundance of <1%. In one location, a probable glauconite pellet (200 µm long) is surrounded by very clear black and orange alteration zones (Figure **F20D**). Small clusters of a pale, fibrous mineral that has low birefringence is present in Sections 378-U1553C-41R-1 and 378-U1553D-10R-1 and is tentatively identified as zeolite (Figure **F20F**). A thin interval in this subunit also contains small amounts (about 5%) of secondary dolomite crystals (interval 10R-1, 33–36 cm) (Figure **F20E**).

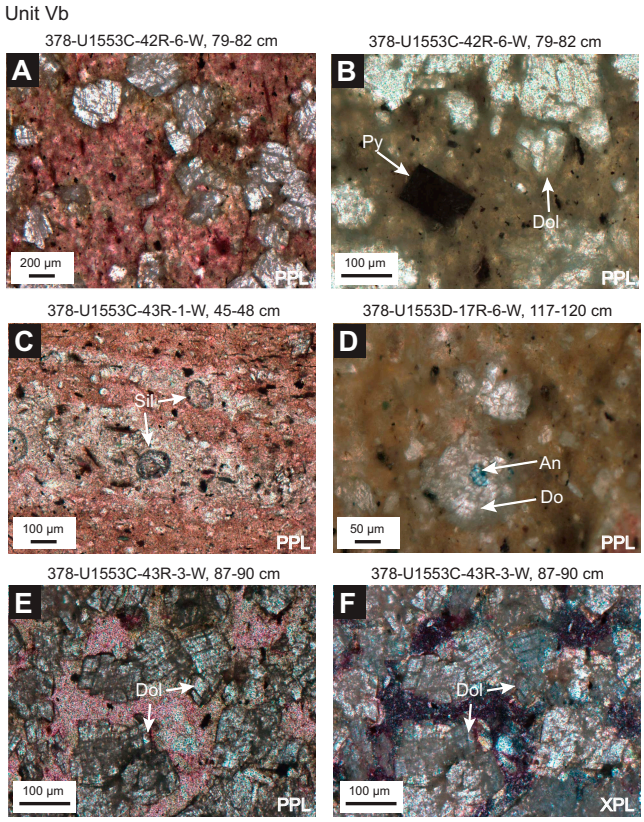

Figure F19. Thin section microphotographs from Subunit Vb, Holes U1553C and U1553D. All are stained by potassium ferricyanide and Alizarin Red S unless otherwise noted. A. Dolomitic mudstone that contains ~30% pale, secondary dolomite crystals with rhombohedral cleavage in a matrix that was pale brown before staining and in the photograph is stained pink, indicating the presence of clays and small amount of micritic calcite. B. Dolomite (Dol) and cubic pyrite (Py). C. Biogenic silica (Sil) surrounded by a matrix containing some calcite. D. Dolomite (Do) crystal with a ferroan dolomite or ankerite core (An) but little evidence of calcite in the matrix. E, F. Calcareous dolostone composed of an interlocking matrix of dolomite crystals cemented by calcite.

3.5.2. Subunit Vb

Intervals: 378-U1553C-42R-1, 0 cm, to 44R-CC, 5 cm (BOH); 378-U1553D-17R-1, 0 cm, to 20R-CC, 5 cm (BOH)
Depths: Hole U1553C = 545.40–566.03 mbsf; Hole U1553D = 545.30–581.16 mbsf
Age: unknown
Lithology: mudstone to dolomitic mudstone, occasionally sandy

Lithostratigraphic Subunit Vb is delineated by an increase in bioturbation as well as a sometimes high abundance of secondary dolomite crystals (Figure **F21C–F21E**). Bioturbation is ubiquitous, and many different types of ichnofossils are visible, tentatively including *Chondrites, Zoophycos, Phycosiphon*, and *Teichichnus*. Beds with mudstone containing large (average = 200 µm) dolomite crystals have a distinct dark gray color and medium-grained texture and are often interlayered with mudstone units. XRF, XRD, and coulometric analysis indicate a decrease in calcite in this subunit. Calcium concentration decreases from 2.0% in Subunit Va to 0.43% in Subunit Vb according to XRF analyses, and calcite can no longer be detected by XRD in Subunit Vb (Figure **F5E**). The $CaCO_3$ content from the coulometer averages 0.85 wt% for Subunit Vb (see **Geochemistry**). Iron increases in this subunit to a maximum of 7.2%, as measured by XRF. *Bathysiphon* foraminifers are also present in small layers to lenses throughout this subunit.

A ≥19 cm thick calcareous dolostone concretion with 85 wt% $CaCO_3$ and 0.44 wt% total organic carbon (TOC) is present at the bottom of Section 378-U1553C-44R-1 (565.79–565.98 mbsf) (see **Geochemistry**). XRD analysis indicates the concretion is dominantly composed of dolomite (Figure **F5F**) with a minor contribution from calcite in addition to pyrite and muscovite. XRF analysis reveals a fourfold increase in Mg (7.5%) and an order of magnitude increase in Mn concentration

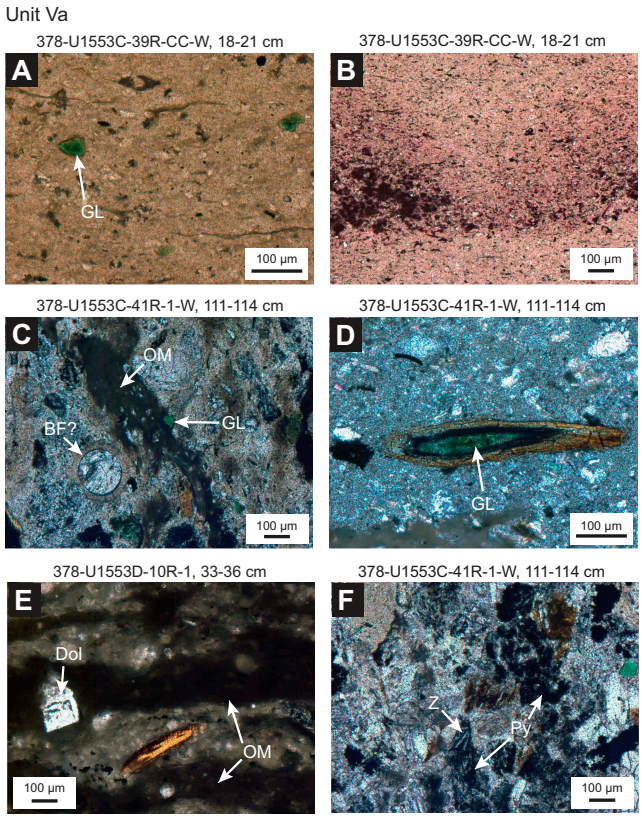

Figure F20. Thin section photomicrographs from Subunit Va, Holes U1553C and U1553D. All are stained by potassium ferricyanide and Alizarin Red S unless otherwise noted. All = PPL. A. Pale yellow-brown siltstone matrix and a glauconite grain (GL), not stained. B. Pale pink siltstone matrix that indicates the presence of calcitic micrite. C. Glauconite, a possible benthic foraminifer (BF), and a large stringer of organic matter (OM) that has a pale gray reflectance. D. Pellet, probably glauconite, surrounded by very clear black and orange alteration zones. E. Dolomite (Dol) crystal in mudstone matrix. F. Relationship between a pale, fibrous mineral that has low birefringence (tentatively zeolite; Z) and surrounding pyrite (PY).

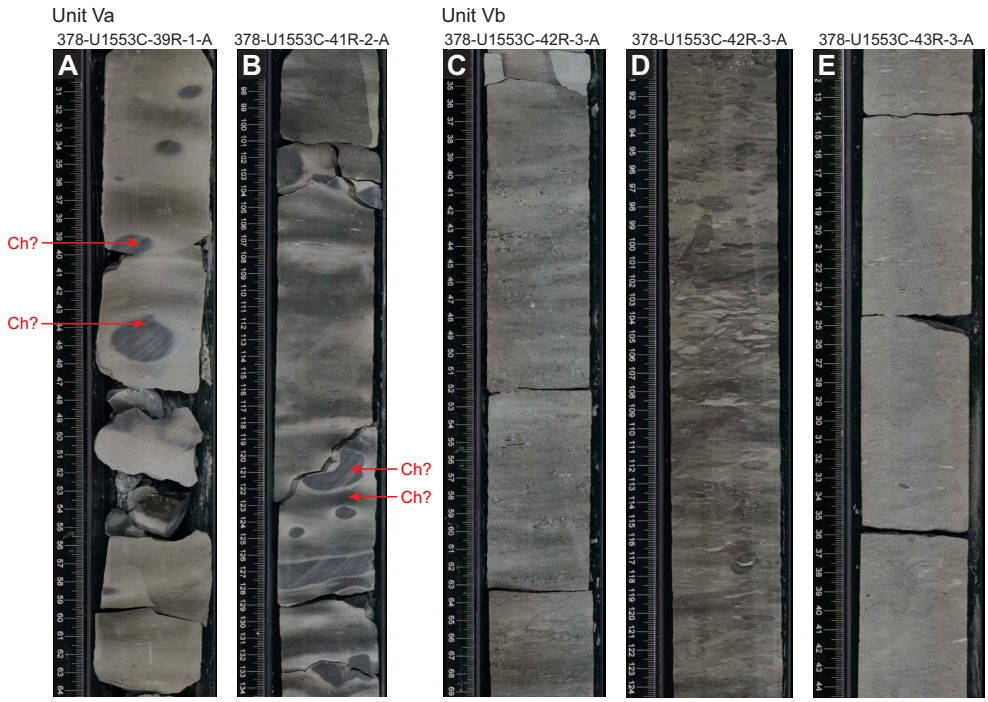

Figure F21. Characteristic lithologies in Unit V, Hole U1553C. Subunit Va: A. Dark and light bands and darker gray, centimeter-sized diagenetically modified areas resulting from chert nodule formation (Ch? = possible chert). B. Dark and light bands and darker gray, centimeter-sized diagenetically modified areas with paler halos as both nodules and bands. Subunit Vb: C. Moderate bioturbation. D. High bioturbation. E. Slight bioturbation.

(1877 ppm). An analogous 19 cm thick calcareous dolostone concretion is present in Section 378-U1553D-18R-4 (559.35–559.54 mbsf).

Thin section analysis of 13 samples from Subunit Vb shows that dolomite varies substantially in abundance throughout the cores and sometimes within a single thin section. For example, a thin section from Section 378-U1553C-42R-6 contains about 30% dolomite (Figure **F19A**). Dolomite can be easily distinguished from the pink-stained matrix of the mudstone, which is interpreted to be a mixture of clays and micritic calcite, although we note that $CaCO_3$ wt% indicates a low calcite contribution in this unit. However, other mudstones contain significantly less dolomite. One interval (43R-3, 87–96 cm; 558.39–558.48 mbsf) is mainly composed of an interlocking matrix of dolomite crystals cemented by calcite (Figure **F19E–F19F**) and is termed calcareous dolostone. The extent of dolostone in Subunit Vb could not be determined by macroscopic observation because it looks similar to the mudstone. In one thin section (Sample 378-U1553D-17R-6, 117–120 cm), a small amount of ferroan dolomite or ankerite that stained a turquoise color was detected in the center of a dolomite crystal (Figures **F19D**, **F21E**), but the vast majority of the dolomite in the thin section does not contain iron. Some biogenic silica is present (Figure **F19E**). Pyrite is sometimes present in cubic form, sometimes as clumps or in small lenses (Figure **F19B**).

4. Biostratigraphy and micropaleontology

The five holes drilled at Site U1553 recovered a 580 m thick succession of nannofossil ooze, chalk, limestone, and muddy sandstone to silty mudstone. Biostratigraphic results indicate that, apart from a thin veneer of Pleistocene sediments, the succession spans the early late Oligocene to early Paleocene and includes an expanded ~250 m thick Oligocene–late Eocene interval with good preservation of calcareous nannofossils, foraminifers, and radiolarians. Diatoms, silicoflagellates, and sponge spicules are also common and well preserved throughout this interval. The Eocene and Paleocene intervals are less expanded and have more variable microfossil abundance and preservation, but biostratigraphic and lithologic evidence indicates that both the EOT and Paleocene/Eocene (P/E) boundary are intact. Low calcareous and siliceous microfossil abundance and

generally poor preservation in the basal muddy sandstone unit (Lithostratigraphic Unit V) meant that we could not date this unit all the way down to the total depth of Holes U1553C and U1553D. Postcruise study of dinoflagellate assemblages has confirmed that the base of the cored interval is of early Paleocene age. A summary of abundance and preservation for calcareous nannofossils, foraminifers, and radiolarians for Site U1553 is shown in Figure **F22**.

All planktonic microfossil groups lack most of the low-latitude species that form the basis of standard zonation schemes. For this reason, correlation and age assignments are based primarily on Southern Ocean and Southwest Pacific zonations, as noted below. An integrated biozonation for the five holes shows overall good agreement between the observed bioevents in different microfossil groups (Figures **F23**, **F24**). Tables **T2**, **T3**, and **T4** list the datums that underpin the biozonations and are used, together with some paleomagnetic data, to develop the age-depth model for Site U1553 (see **Age-depth model and mass accumulation rates**).

4.1. Calcareous nannofossils

Shipboard calcareous nannofossil biostratigraphy focused primarily on age diagnostic species (Figure **F25**) in core catcher and additional working-half samples and therefore is not representative of complete assemblages. Table **T2** shows depth positions and age estimates of calcareous nannofossil biostratigraphic marker events identified at Site U1553. Calcareous nannofossil occurrence data are shown in Table **T5**. Calcareous nannofossils are abundant in the majority of samples from Holes U1553A, U1553B, and U1553E and are abundant to barren in Holes U1553C and U1553D (Figure **F22**). Abundance of calcareous nannofossils is related to lithology; abundance is high in Lithostratigraphic Unit I (foraminiferal ooze with calcareous nannofossils) and

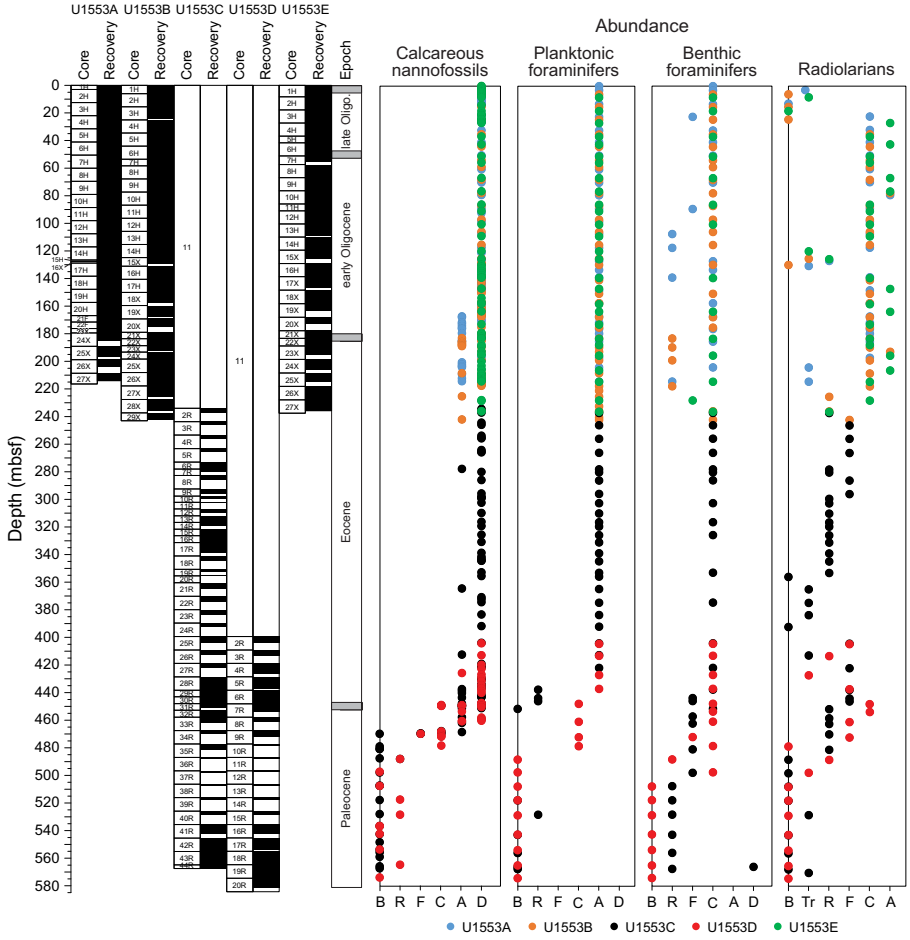

Figure F22. Microfossil abundance, Site U1553. Abundance: D = dominant, A = abundant, C = common, F = few, R = rare, B = barren. (Continued on next page.)

Unit II (nannofossil ooze with foraminifers) and decreases in Unit III (limestone). Abundance is very low or nannofossils are absent in Unit IV (muddy sandstone); carbonate content varies from 5% to 90% in the upper part of Unit IV, where only rare/sporadic nannofossils were recorded. Nannofossils are generally absent in the underlying interval, although rare occurrences of single specimens are noted. Preservation ranges from good to poor and is generally good to moderate in the entire succession of Holes U1553A, U1553B, and U1553E, corresponding to the very high carbonate content of Units I–III. Preservation generally starts to deteriorate around the Eocene/Oligocene (E/O) boundary, where nannofossils show signs of overgrowth or etching. Sediments of late Eocene to late Paleocene age generally have moderate to poor preservation due to calcite overgrowth, which sometimes obscures morphological features of the diagnostic taxa. This is especially problematic for the genus *Chiasmolithus* and can hinder confident species-level identification.

Calcareous nannofossil assemblages at Site U1553 are dominated throughout by typical high-latitude/cool-affinity genera (e.g., *Reticulofenestra* and *Chiasmolithus*) and are lower in diversity than lower latitude assemblages. Warm- and temperate-water *Sphenolithus* and *Discoaster* species are generally absent or very rare and scattered in Oligocene and late Eocene sediments at Site U1553. We therefore utilize the Southern Ocean biozonation scheme of Fioroni et al. (2012) for the calcareous nannofossil biostratigraphy of the middle Eocene–upper Oligocene sediments in Holes U1553A, U1553B, and U1553E. The high-latitude character is also reflected in the nannofossil assemblages observed in middle Eocene to lower Paleocene sediments, in which most of the markers from low- to mid-latitude biozonations are missing or sporadically occur. In this interval, however, the scheme of Martini (1971), with some integrations of the biohorizons indicated above, has been applied successfully.

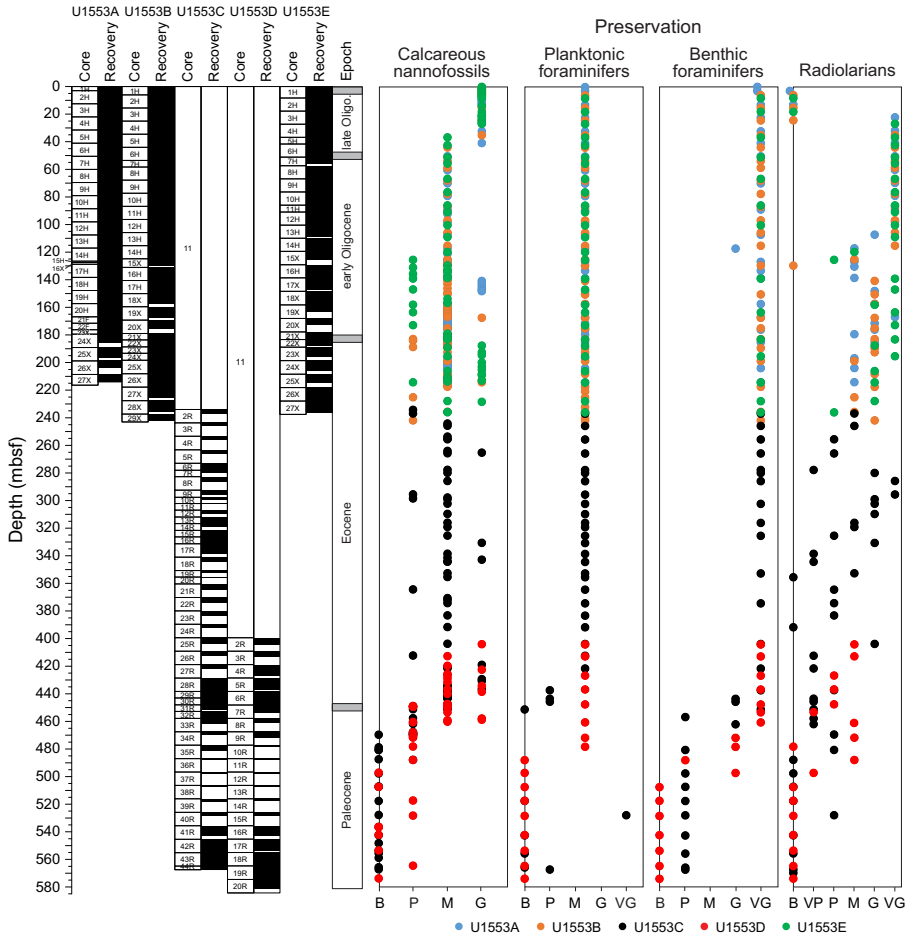

Figure F22 (continued). Microfossil preservation, Site 1553. Preservation: VG = very good, G = good, M = moderate, P = poor, VP = very poor, B = barren.

4.1.1. Pleistocene

The uppermost sediment at Site U1553 contains abundant nannofossils of Pleistocene Biozones NN20–NN21, as indicated by the presence of abundant *Gephyrocapsa* spp. and the presence of *Pseudoemiliania lacunosa* in Samples 378-U1553A-1H-CC; 378-U1553B-1H-2, 100 cm; and 378-U1553E-1H-3, 50 cm. A major hiatus is inferred between Sample 378-U1553A-1H-CC, which contains upper Pleistocene taxa including *P. lacunosa*, and Sample 2H-1, 110 cm, which can be placed in the upper Oligocene *Chiasmolithus altus* Zone (which corresponds to Biozone NP25). This hiatus is observed in Hole U1553B between Samples 1H-3, 50 cm, and 1H-3, 100 cm, and in Hole U1553E between Samples 1H-3, 50 cm, and 1H-3, 100 cm. The hiatus indicated by the calcareous nannofossil biostratigraphy corresponds to the sharp lithologic transition at 4.0 mbsf in Hole U1553A, 3.68 mbsf in Hole U1553B, and 3.61 mbsf in Hole U1553C. The position of the top of *P. lacunosa* (0.44 Ma), precisely recorded in Hole U1553B at 2.25 mbsf, is consistent with the paleomagnetic data that place the Brunhes/Matuyama reversal at 2.2 mbsf in Hole U1553A. The assemblage composition of the samples immediately below the hiatus shows evidence of mixing/reworking; there are specimens of, for example, late Eocene *Chiasmolithus expansus, Discoaster saipanensis, Neococcolithes dubius*, and *Reticulofenestra oamaruensis*

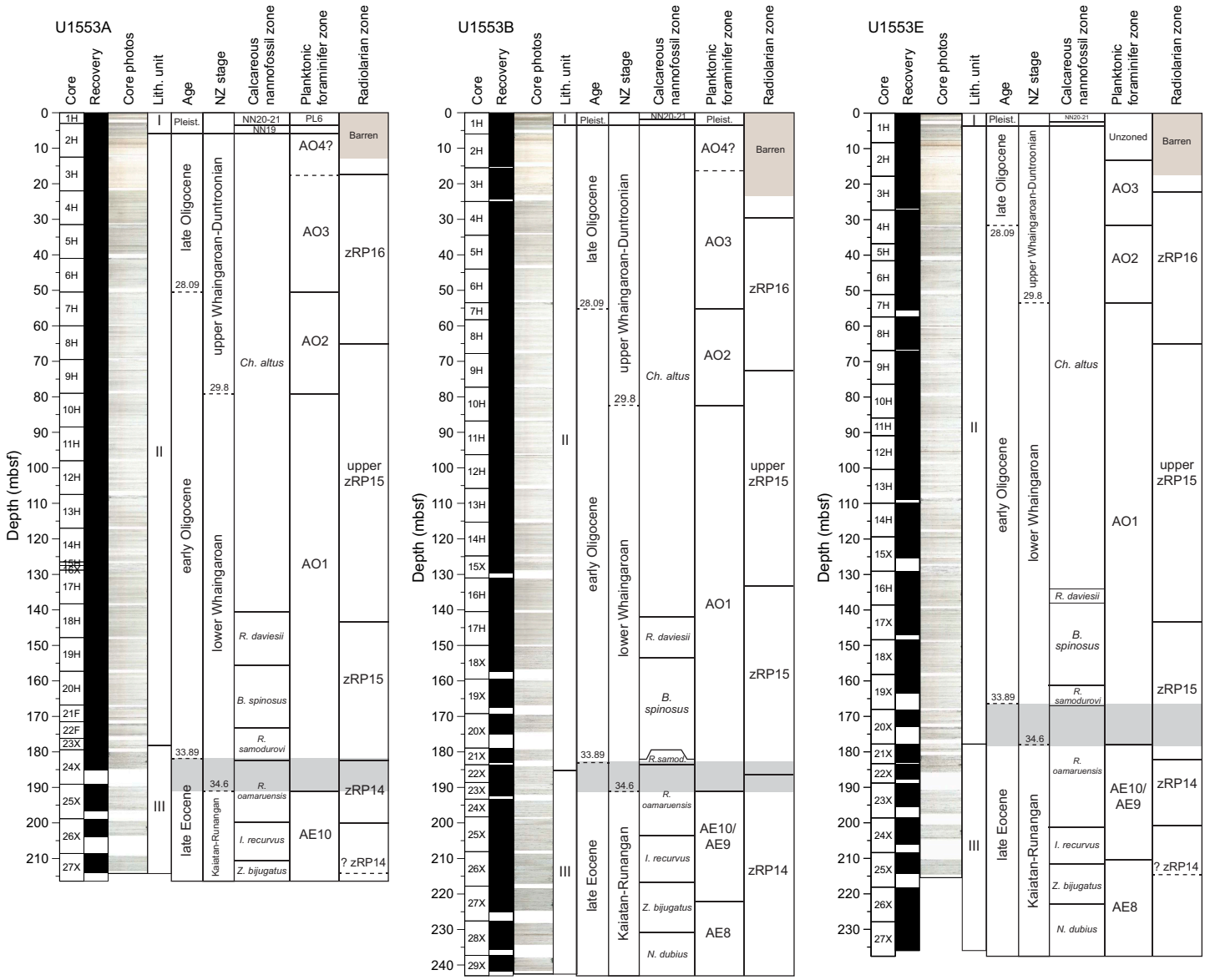

Figure F23. Distribution of biostratigraphic zones and datum events for calcareous nannofossils, planktonic foraminifers, and radiolarians, Holes U1553A, U1553B, and U1553E.

within samples of late Oligocene age in Cores 378-U1553A-2H, 378-U1553B-1H, and 378-U1553E-1H.

4.1.2. Oligocene

Cores 378-U1553A-2H through 23H, 378-U1553B-1H through 21H, and 378-U1553E-1H through 19X are Oligocene in age. Application of the zonation scheme of Fioroni et al. (2012) enables differentiation of biozones only in the lower part of the early Oligocene, owing to the very low biostratigraphic resolution that characterizes the overlying Oligocene interval. This interval is correlated to the late–early Oligocene *C. altus* Zone. The underlying interval extends 140.82–182.45 mbsf in Hole U1553A, 141.91–186.95 mbsf in Hole U1553B, and 134.89–167.81 mbsf in Hole U1553E (Figure **F23**). The top common occurrence of *Reticulofenestra umbilicus* (between Samples 378-U1553A-18H-1, 100 cm, and 18H-2, 100 cm [140.06 mbsf]; 378-U1553B-16H-CC and 17H-2, 110 cm [141.91 mbsf]; and 378-U1553E-16H-4, 50 cm, and 16H-5, 50 cm [134.89 mbsf]) marks the base of the *C. altus* Zone (early Oligocene). The top of *Isthmolithus recurvus* (between Samples 378-U1553A-19H-5, 80 cm, and 19H-6, 80 cm [155.36 mbsf]; 378-U1553B-17H-CC and 18X-5, 72 cm [153.64 mbsf]; and 378-U1553E-16X-6, 50 cm, and 16X-7, 50 cm [137.90 mbsf]) marks the base of the *Reticulofenestra daviesii* Zone. Oligocene assemblages have common to abundant *Reticulofenestra* spp., *Chiasmolithus* spp., *Cyclicargolithus* spp., and *Coccolithus pelagicus* and few *Zygrhablithus bijugatus, Sphenolithus moriformis*,

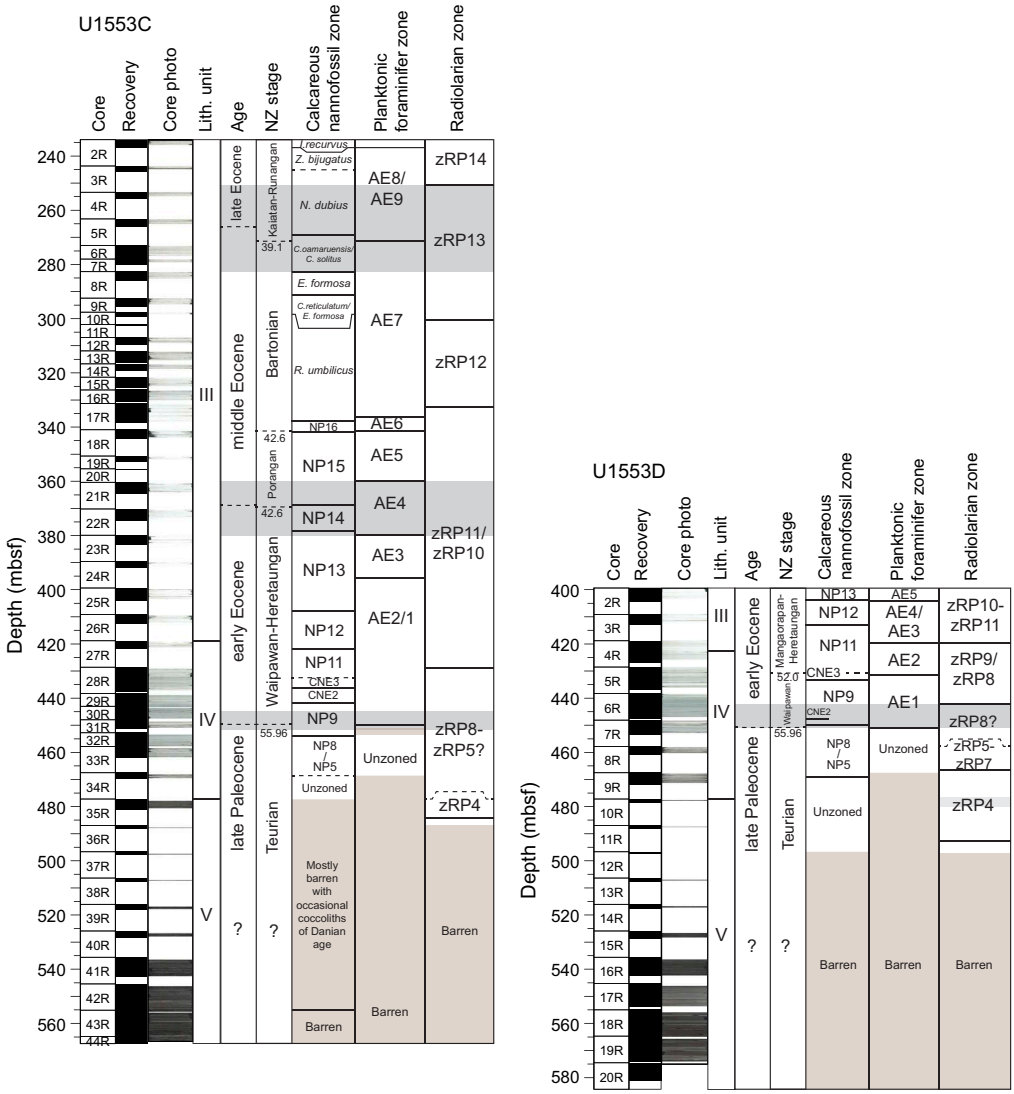

Figure F24. Distribution of biostratigraphic zones and datum events for calcareous nannofossils, planktonic foraminifers, and radiolarians, Holes U1553C and U1553D.

and *I. recurvus*. *Discoaster* spp. are generally very rare and occur sporadically in samples throughout the early Oligocene to late Eocene. The base of *C. altus* (between Samples 378-U1553A-22F-2, 100 cm, and 22F-3, 100 cm [174.76 mbsf]; 378-U1553B-21X-3, 42 cm, and 21X-CC [182.63 mbsf]; 378-U1553E-18X-CC and 19X-CC [160.79 mbsf]) marks the base of the *Blackites spinosus* Subzone. An interval characterized by an increase in the abundance of *Clausicoccus subdistichus* is observed in Cores 378-U1553A-20H and 21F and between Samples 378-U1553B-19H-CC and 20H-CC. This event (base common occurrence) may indicate proximity to the E/O boundary, as observed at low- and mid-latitude sites where it has been calibrated to

Table T2. Calcareous nannofossil datums, Site U1553. T = top, Tc = top common, B = base, Bc = base common. (Continued on next page.) **Download table in CSV format.**

Age/zone (base)	Datum	Age (Ma)	Core, section, interval (cm)		Depth CSF-A (mbsf)			
			Top	Bottom	Top	Bottom	Midpoint	±
Pleistocene			378-U1553A-	378-U1553A-				
NN20	T *Pseudoemiliania lacunosa*	0.44	1H-CC	2H-1, 110	3.03	4.11	3.57	0.54
Hiatus			2H-2, 50	2H-2, 110	5.01	5.62	5.32	0.31
	Chiasmolithus altus last occurrence		2H-2, 50	2H-2, 110	5.01	5.62	5.32	0.31
Chiasmolithus altus Zone	Tc *Reticulofenestra umbilicus* (>14 µm)	31.51	18H-1, 100	18H-2, 100	139.30	140.82	140.06	0.76
Reticulofenestra daviesii Zone	T *Isthmolithus recurvus*	32.49	19H-5, 80	19H-6, 80	154.60	156.11	155.36	0.75
Additional biovent	B increase *Clausicoccus subdistichtus*		21F-2, 100	21F-3, 100	169.30	170.81	170.06	0.75
Blackites spinosus Zone	B *Chiamolithus altus*	33.31	22F-2, 100	22F-3, 100	174.01	175.51	174.76	0.75
Additional bioevent in *R. samodurovi* Zone	B increase *Reticulofenestra daviesii*	33.71	23X-CC	24X-1, 80	179.38	180.20	179.79	0.41
Eocene/Oligocene Boundary		33.89						
Reticulofenestra samodurovi Zone	T *Reticulofenestra oamaruensis*	33.97	24X-2, 80	24X-3, 80	181.70	183.20	182.45	0.75
Reticulofenestra oamaruensis Zone	B *Reticulofenestra oamaruensis*	35.54	26X-1, 20	26X-2, 20	199.00	200.50	199.75	0.75
Additional bioevent in *Z. bijugatus* Subzone	T *Reticulofenestra reticulata*	35.92	26X-CC	27X-1, 46	203.88	209.06	206.47	2.59
Isthmolithus recurvus Zone	Bc *Isthmolithus recurvus*	36.01	27X-1, 46	27X-3, 54	209.06	212.14	210.60	1.54
Zygrablithus bijugatus Subzone	T *Neococcolithes dubius*	36.7	Below Core 27X-CC — bottom Hole A					
Eocene			378-U1553C-	378-U1553C-				
Additional bioevent in *Z. bijugatus* Subzone	T *Reticulofenestra reticulata*	35.92	2R-1, 30	2R-CC	234.31	236.88	235.60	1.29
Isthmolithus recurvus Zone	Bc *Isthmolithus recurvus*	36.01	2R-1, 30	2R-CC	234.31	236.88	235.60	1.29
Zygrablithus bijugatus Subzone	T *Neococcolithes dubius*	36.70	2R-1, 30	2R-CC	234.31	236.88	235.60	1.29
Neococcolithes dubius Subzone	T *Chiasmolithus solitus*	38.34	5R-CC	6R-1, 40	265.85	273.41	269.63	3.78
C. oamaruensis/C. solitus Subzone	B *Chiasmolithus oamaruensis*	38.80	7R-CC	8R-CC	279.98	285.85	282.92	2.94
Ericsonia formosus Subzone	Tc *Coccolithus formosus*	39.02	8R-CC	9R-CC	285.85	295.58	290.72	4.86
C. reticulatum/R. clatrata Subzone	B *Reticulofenestra reticulata*	40.69	10R-1, 30	10R-1, 100	297.90	298.61	298.26	0.36
Reticulofenestra umbilicus Zone	B *Reticulofenestra umbilicus*	42.48	17R-5, 60	17R-CC	337.87	338.54	338.21	0.33
NP16	T *Nannotetrina alata* gr. (*N. fulgens*)	42.87	18R-1, 50	18R-2, 50	341.50	342.94	342.22	0.72
NP15a	B *Nannotetrina alata* gr. (*N. fulgens*)	46.29	21R-CC	22R-CC	364.54	374.45	369.50	4.95
CNE7	T *Discoaster lodoensis*	47.41	22R-2, 60	22R-CC	372.31	374.40	373.36	1.04
NP14	B *Discoaster sublodoensis* (5-rayed)	49.11	22R-CC	23R-CC	374.40	383.33	378.86	4.46
NP13	T *Tribrachiatus orthostylus*	50.5	25R-CC	26R-CC	403.96	412.45	408.20	4.25
NP12	B *Discoaster lodoensis*	53.7	27R-2, 54	27R-CC	420.77	421.70	421.24	0.46
Additional bioevent for Base NP11	B *Sphenolithus radians*	54.17	28R-3, 70	28R-4, 85	432.26	433.92	433.09	0.83
NP11	T *Tribrachiatus contortus*	54.17	Not reliable					
CNE3	B *Tribrachiatus orthostylus*	54.37	28R-5, 36	28R-6, 85	434.95	436.87	435.91	0.96
CNE2	T *Fasciculithus typaniformis*	58.7	29R-2, 52	29R-3, 42	440.33	441.65	440.99	0.66
Paleocene/Eocene boundary		55.96	Within Core 31R					
NP9	B *Discoaster multiradiatus*	57.1	31R-CC	32R-CC	451.36	457.86	454.61	3.25
NP5	B *Fasciculithus typaniformis*	61.51	34R-1, 107	34R-1, 130	468.58	468.60	468.59	0.01
Pleistocene			378-U1553E-	378-U1553E-				
NN20	T *Pseudoemiliania lacunosa*	0.44	1H-2, 50	1H-2, 100	2.00	2.50	2.25	0.25
Hiatus			1H-3, 50	1H-3, 100	3.51	4.01	3.76	0.25
	Chiasmolithus altus last occurrence		1H-3, 50	1H-3, 100	3.51	4.01	3.76	0.25
Chiasmolithus altus Zone	Tc *Reticulofenestra umbilicus* (>14 µm)	31.51	16H-4, 50	16H-5, 50	134.15	135.63	134.89	0.74
Reticulofenestra daviesii Zone	T *Isthmolithus recurvus*	32.49	16H-6, 50	16H-7, 50	137.15	138.65	137.90	0.75
Blackites spinosus Zone	B *Chiasmolithus altus*	33.31	18X-CC	19X-CC	158.04	163.53	160.79	2.75
Eocene/Oligocene boundary		33.89	19X-CC	20X-CC				
Reticulofenestra samodurovi Zone	T *Reticulofenestra oamaruensis*	33.97	19X-CC	20X-CC	163.53	172.08	167.81	4.28
Reticulofenestra oamaruensis Zone	B *Reticulofenestra oamaruensis*	35.54	24X-1, 127	24X-3, 127	199.87	202.88	201.38	1.51
Additional bioevent in *Z. bijugatus* Subzone	T *Reticulofenestra reticulata*	35.92	25X-2, 67	25X-3, 67	210.57	212.07	211.32	0.75
Isthmolithus recurvus Zone	Bc *Isthmolithus recurvus*	36.01	25X-3, 67	25X-4, 10	212.07	213.00	212.54	0.47
Z. bijugatus Subzone	T *Neococcolithes dubius*	36.7	26X-4, 30	26X-4, 111	222.89	223.70	223.30	0.41
Additional bioevent in *N. dubius* Subzone	B *Isthmolithus recurvus*	37.98	27X-CC, 18	27X-CC, 37	235.86	236.03	235.94	0.08

33.88 Ma (Agnini et al., 2014). The E/O boundary is approximated by the top of *R. oamaruensis* (Wei and Thierstein, 1991) near the top of Chron C13r, as calibrated at other Southern Ocean sites (Fioroni et al., 2012). This biohorizon occurs between Samples 378-U1553A-24X-2, 80 cm, and 24X-3, 80 cm (182.45 mbsf); 378-U1553B-21X-CC and 22X-1, 48 cm (183.51 mbsf); and 378-U1553E-19X-CC and 20X-CC (167.81 mbsf) and marks the base of the *Reticulofenestra samodurovi* Zone. The top of *R. oamaruensis* is widely used in high-latitude sequences as an alternative biohorizon to the highest occurrence of rosette-shaped discoasterids (top of *D. saipanensis*; base of Biozone NP21; 34.44 Ma) and occurs just before the E/O boundary at lower latitudes (Fioroni et al., 2012).

Table T2 (continued).

Age/zone (base)	Datum	Age (Ma)	Core, section, interval (cm)		Depth CSF-A (mbsf)			
			Top	Bottom	Top	Bottom	Midpoint	±
Pleistocene			378-U1553B-	378-U1553B-				
NN20	T *Pseudoemiliania lacunosa*	0.44	1H-2, 50	1H-2, 100	2.00	2.50	2.25	0.25
Hiatus			1H-3, 50	11H-3, 100	3.51	4.01	3.76	0.25
	Chiasmolithus altus last occurrence							
Chiasmolithus altus Zone	Tc *Reticulofenestra umbilicus* (>14 µm)	31.51	16H, CC	17H-2, 110	140.71	143.11	141.91	1.20
Reticulofenestra daviesii Zone	T *Isthmolithus recurvus*	32.49	17X-CC	18X-5, 72	150.54	156.74	153.64	3.10
Additional biovent	B increase *Clausicoccus subdistichtus*		19X-CC	20X-CC	167.51	175.10	171.31	3.79
Blackites spinosus Zone	B *Chiamolithus altus*	33.31	21X-3, 42	21X-CC	182.33	182.93	182.63	0.30
Additional bioevent in *R. samodurovi* Zone	B increase *Reticulofenestra daviesii*	33.71						
Eocene/Oligocene Boundary		33.89						
Reticulofenestra samodurovi Zone	T *Reticulofenestra oamaruensis*	33.97	21X-CC	22X-1, 48	182.93	184.09	183.51	0.58
Reticulofenestra oamaruensis Zone	B *Reticulofenestra oamaruensis*	35.54	24X-CC	25X-CC	198.82	208.22	203.52	4.70
Additional bioevent in *Z. bijugatus* Subzone	T *Reticulofenestra reticulata*	35.92	26X-6, 20	26X-7, 20	215.85	216.85	216.35	0.50
Isthmolithus recurvus Zone	Bc *Isthmolithus recurvus*	36.01	26X-6, 20	26X-7, 20	215.85	216.85	216.35	0.50
Zygrablithus bijugatus Subzone	T *Neococcolithes dubius*	36.7	27X-CC	28X-CC	225.10	235.66	230.38	5.28
Eocene			378-U1553D-	378-U1553D-				
Additional bioevent in *Z. bijugatus* Subzone	T *Reticulofenestra reticulata*	35.92						
Isthmolithus recurvus Zone	Bc *Isthmolithus recurvus*	36.01						
Zygrablithus bijugatus Subzone	T *Neococcolithes dubius*	36.70						
Neococcolithes dubius Subzone	T *Chiasmolithus solitus*	38.34						
C. oamaruensis/C. solitus Subzone	B *Chiasmolithus oamaruensis*	38.80						
Ericsonia formosus Subzone	Tc *Coccolithus formosus*	39.02						
C. reticulatum/R. clatrata Subzone	B *Reticulofenestra reticulata*	40.69						
Reticulofenestra umbilicus Zone	B *Reticulofenestra umbilicus*	42.48						
NP16	T *Nannotetrina alata* gr. (*N. fulgens*)	42.87						
NP15a	B *Nannotetrina alata* gr. (*N. fulgens*)	46.29						
CNE7	T *Discoaster lodoensis*	47.41						
NP14	B *Discoaster sublodoensis* (5-rayed)	49.11						
NP13	T *Tribrachiatus orthostylus*	50.5	2R-CC	3R-CC	404.23	412.93	408.58	4.35
NP12	B *Discoaster lodoensis*	53.7	3R-CC	4R-1, 110	412.93	419.90	416.42	3.49
Additional bioevent for Base NP11	B *Sphenolithus radians*	54.17	5R-3, 50	5R-5, 50	431.68	434.46	433.07	1.39
NP11	T *Tribrachiatus contortus*	54.17	5R-5, 50	5R-CC	434.46	436.92	435.69	1.23
CNE3	B *Tribrachiatus orthostylus*	54.37	5R-5, 50	5R-CC	434.46	436.91	435.68	1.22
CNE2	T *Fasciculithus typaniformis*	58.7	6R-7, 45	6R-CC	447.48	447.79	447.64	0.16
Paleocene/Eocene Boundary		55.96	Within Section 7R-2					
NP9	B *Discoaster multiradiatus*	57.1	7R-CC	8R-1, 33	453.64	458.13	455.89	2.25
NP5	B *Fasciculithus typaniformis*	61.51	9R-1, 68	9R-2, 93	468.18	469.92	469.05	0.87
Pleistocene								
NN20	T *Pseudoemiliania lacunosa*	0.44						
Hiatus								
	Chiasmolithus altus last occurrence							
Chiasmolithus altus Zone	Tc *Reticulofenestra umbilicus* (>14 µm)	31.51						
Reticulofenestra daviesii Zone	T *Isthmolithus recurvus*	32.49						
Blackites spinosus Zone	B *Chiasmolithus altus*	33.31						
Eocene/Oligocene boundary		33.89						
Reticulofenestra samodurovi Zone	T *Reticulofenestra oamaruensis*	33.97						
Reticulofenestra oamaruensis Zone	B *Reticulofenestra oamaruensis*	35.54						
Additional bioevent in *Z. bijugatus* Subzone	T *Reticulofenestra reticulata*	35.92						
Isthmolithus recurvus Zone	Bc *Isthmolithus recurvus*	36.01						
Z. bijugatus Subzone	T *Neococcolithes dubius*	36.7						
Additional bioevent in *N. dubius* Subzone	B *Isthmolithus recurvus*	37.98						

4.1.3. Eocene

In the late Eocene, nannofossil assemblages largely resemble early Oligocene assemblages, including taxa such as *Reticulofenestra* spp. (common to abundant), *Cyclicargolithus* spp., *Chiasmolithus* spp., and *C. pelagicus*. In the late Eocene, the interval characterized by the presence of *R. oamaruensis* was recovered in Hole U1553A from 182.45 to 199.75 mbsf, in Hole U1553B from 183.51 to 203.52 mbsf, and in Hole U1553E from 167.81 to 201.38 mbsf. It corresponds to the latest Eocene *R. oamaruensis* Zone (Figure **F23**). The underlying upper Eocene biozones are defined by the following biohorizons: the base of common and continuous *I. recurvus* (between Samples 378-U1553A-27X-1, 46 cm, and 27X-3, 54 cm, [210.60 mbsf]; 378-U1553B-26X-6, 20 cm, and 26X-7, 20 cm [216.35 mbsf]; and 378-U1553E-25X- 3, 67 cm, and 25X-4, 10 cm [212.15 mbsf]), which marks the base of the *I. recurvus* Zone, and the top of *Reticulofenestra reticulata*, an additional biohorizon occurring between Samples 378-U1553A-26X-CC and 27X-1, 46 cm (206.47 mbsf); 378-U1553B-26X-6, 20 cm, and 26X-7, 20 cm (216.35 mbsf); and 378-U1553E-25X-2, 67 cm, and 25X-3, 67 cm (211.32 mbsf). The top of *Neococcolithus dubius* in Samples 378-U1553B-27X-CC and 28X-CC places the bottom of Hole U1553B (Core 28X) in the *Chiasmolithus oamaruensis* Zone, which straddles the middle–late Eocene time interval. This biohorizon was not identified in Holes U1553A and U1553E, presumably because these holes were shallower than Hole U1553B.

Holes U1553C and U1553D recovered sediments Eocene to early Paleocene in age (Figure **F24**). The biohorizon top of *R. reticulata* and base of common *I. recurvus* are recorded at the top of the Hole U1553C succession in Section 2R, confirming a late Eocene age (*I. recurvus* Zone). This interval overlaps with the sediments in Core 378-U1553A-27X, the upper part of Core 378-U1553B-27X, and the lower part of Core 378-U1553E-24X. The presence of *N. dubius* in Core

Table T3. Foraminifer datums, Site U1553. B = bottom, T = top, HCO = highest common occurrence. **Download table in CSV format.**

Age/zone (base)	Datum	Age (Ma)	Core, section, interval (cm)		Depth CSF-A (mbsf)			
			Top	Bottom	Top	Bottom	Midpoint	±
Pliocene			378-U1553A-	378-U1553A-				
Upper PL6	B *T. crassula*	Not calibrated	1H-CC	2H-CC	3.03	3.08	3.06	0.03
Oligocene								
AO4?	B *G. bulloides*	Not calibrated	1H-CC	2H-CC	3.03	13.08	8.06	5.03
AO4	T *Globoturborotalita labiacrassata*	26.50	2H-CC	3H-CC	13.08	22.24	17.66	4.58
AO3	T HCO *Chiloguembelina cubensis*	28.1	5H-CC	6H-CC	40.76	50.42	45.59	4.83
AO2	T *Subbotina angiporoides*	29.8	9H-CC	10H-CC	79.10	89.00	84.05	4.95
AO1	T *Globigerinatheka index*	34.60	24X-CC	25H-CC	185.19	196.79	190.99	5.80
Eocene								
AE10	*Globigerinatheka index* occurrence		Below 25H-CC	Bottom Hole A				
AE10/AE9	T *Globigerinatheka barri*	Not calibrated						
AE8								
Oligocene			378-U1553C-	378-U1553C-				
AO1	T *Globigerinatheka index*	34.6	2R-CC	3R-CC	236.85	236.90	236.88	0.03
Eocene								
AE9	T *Globigerinatheka barri*	Not calibrated	4R-CC	5R-CC	255.56	265.80	260.68	5.12
AE8	T *Acarinina primitiva*	39.10	5R-CC	6R-CC	265.80	277.74	271.77	5.97
AE7	B *Subbotina angiporoides*	42.11	16R-CC	17R-CC	330.71	338.54	334.63	3.92
AE6	B *Globigerinatheka index*	42.60	17R-CC	18R-CC	338.54	344.37	341.46	2.91
AE5	T *Cassigerinelloita amekiensis*	46.13	20R-CC	21R-CC	355.52	364.54	360.03	4.51
	T *Morozovella crater*	45.70	21R-CC	22R-CC	364.54	374.40	369.47	4.93
AE4	B *Cassigerinelloita amekiensis*	50.04	22R-CC	23R-CC	374.40	383.30	378.85	4.45
AE3	B *Acarinina primitiva*	51.43	27R-CC*	28R-CC	421.70	437.45	429.58	7.88
	B *Morozovella crater*	52.00						
AE2	T *Chiloguembelina wilcoxensis*	53.94						
AE1	B *Globanomalina australiformis*	55.96						
AP4								
Oligocene			378-1553E-	378-1553E-				
AO4	T *Globoturborotalita labiacrassata*	26.5	1H-CC	2H-CC	8.24	8.29	8.27	0.02
AO3	T HCO *Chiloguembelina cubensis*	28.1	3H-CC	4H-CC	26.80	36.68	31.74	4.94
AO2	T *Subbotina angiporoides*	29.8	6H-CC	7H-CC	51.05	55.58	53.32	2.27
AO1	T *Globigerinatheka index*	34.6	20X-CC	21X-CC	172.80	183.14	177.97	5.17
Eocene								
AE10/AE9	T *Globigerinatheka barri*	Not calibrated	24X-CC	25X-CC	206.11	214.25	210.18	4.07
AE8			Below 25X-CC	Bottom Hole E				

378-U1553C-3R-CC indicates the late–middle Eocene *N. dubius* Subzone of the *C. oamaruensis* Zone. The overlying *Z. bijugatus* Subzone seems restricted to the very top of Core 2R-CC. Below the *N. dubius* Subzone, the *C. oamaruensis*/*Chiasmolithus solitus* Subzone (the lowermost subzone of the *C. oamaruensis* Zone) is recognized in the interval between the top of *C. solitus* (273.41 mbsf) and the base of *C. oamaruensis* (282.92 mbsf). It has been identified despite calcite overgrowth that obscured the diagnostic morphologic features of the central area of many *Chiasmolithus* spp. specimens throughout this interval. The interval spanning the middle Eocene between 282.92 and 298.61 mbsf in Hole U1553C corresponds to the *Ericsonia formosa* Zone, the *Chiasmolithus reticulatum*/*E. formosa* Zone, and the *R. umbilicus* Zone. The biohorizons recorded are the top of common occurrence of *Coccolithus formosus* (= *E. formosa*) between Samples 8R-CC and 9R-CC (290.72 mbsf); the base of *R. reticulata* between Samples 10R-1, 30 cm, and 10R-1, 100 cm (298.26 mbsf); and the base of *R. umbilicus* between Samples 17R-5, 60 cm, and 17R-CC (338.21 mbsf). This datum has an age of 42.48 Ma (Fioroni et al., 2012).

For the early middle Eocene and Paleocene, the zonation scheme of Martini (1971) was applied because no higher latitude schemes have been devised for the Paleocene to early Eocene time period. Although we see a general shift toward an increased but irregular presence of warm water *Discoaster* specimens with increasing age downcore, warm water taxa are persistently sparse throughout the recovered intervals of Holes U1553C and U1553D, except for occasional samples in which nannofossil assemblages show greater abundances of taxa typical of low-latitude assemblages. Additionally, some biostratigraphically meaningful taxa in the lower Eocene and upper Paleocene sediments, such as *Tribrachiatus* spp., are generally rare, and *Rhomboaster* spp. are not observed at all. Because the majority of early Eocene and late Paleocene biohorizons are based on these three genera, it is challenging to define biohorizons with complete confidence based purely

Table T3 (continued).

Age/zone (base)	Datum	Age (Ma)	Core, section, interval (cm)		Depth CSF-A (mbsf)			
			Top	Bottom	Top	Bottom	Midpoint	±
Pliocene			378-U1553B-	378-U1553B-				
Upper PL6	B *T. crassula*	Not calibrated						
Oligocene								
AO4?	B *G. bulloides*	Not calibrated						
AO4	T *Globoturborotalita labiacrassata*	26.50	1H-CC	2H-CC	6.08	15.18	10.63	4.55
AO3	T HCO *Chiloguembelina cubensis*	28.1	6H-CC	7H-CC	53.81	58.72	56.27	2.46
AO2	T *Subbotina angiporoides*	29.8	9H-CC	10H-CC	77.62	86.92	82.27	4.65
AO1	T *Globigerinatheka index*	34.60	22X-CC	23X-CC	189.45	192.54	191.00	1.54
Eocene								
AE10	*Globigerinatheka index* occurrence							
AE10/AE9	T *Globigerinatheka barri*	Not calibrated	27X-CC	28X-CC	192.57	235.69	214.13	21.56
AE8			Below 28X-CC	Bottom Hole B				
Oligocene			378-U1553D-	378-U1553D-				
AO1	T *Globigerinatheka index*	34.6						
Eocene								
AE9	T *Globigerinatheka barri*	Not calibrated						
AE8	T *Acarinina primitiva*	39.10						
AE7	B *Subbotina angiporoides*	42.11						
AE6	B *Globigerinatheka index*	42.60						
AE5	T *Cassigerinelloita amekiensis*	46.13	2R-CC	3R-CC	404.23	404.28	404.26	0.02
	T *Morozovella crater*	45.70	2R-CC	3R-CC	404.28	412.88	408.56	4.32
AE4	B *Cassigerinelloita amekiensis*	50.04						
AE3	B *Acarinina primitiva*	51.43	3R-CC	4R-CC	412.88	426.78	419.83	6.95
	B *Morozovella crater*	52.00	4R-CC	5R-CC	426.78	436.89	431.84	5.06
AE2	T *Chiloguembelina wilcoxensis*	53.94	4R-CC	5R-CC	426.78	436.89	431.84	5.06
AE1	B *Globanomalina australiformis*	55.96	6R-CC	7R-CC	447.76	453.46	450.61	2.85
AP4			Below 7R-CC					
Oligocene								
AO4	T *Globoturborotalita labiacrassata*	26.5						
AO3	T HCO *Chiloguembelina cubensis*	28.1						
AO2	T *Subbotina angiporoides*	29.8						
AO1	T *Globigerinatheka index*	34.6						
Eocene								
AE10/AE9	T *Globigerinatheka barri*	Not calibrated						
AE8								

on shipboard observation. However, we identify the top of *Tribrachiatus orthostylus* between Samples 378-U1553C-25R-CC and 26R-CC (408.20 mbsf) and 378-U1553D-2R-CC and 3R-CC (408.58 mbsf) (Figure **F26**). This datum defines the base of lower Eocene Biozone NP13 and has an age of 50.5 Ma. Overgrown specimens of *Tribrachiatus contortus* and *Tribrachiatus bramlettei* are observed, rare and scattered, in Cores 378-U1553C-28R through 30R and 378-U1553D-5R and 6R, but their identification should be considered tentative (e.g., the presence of overgrown specimens of *T. bramlettei* recorded in Sample 378-U1553C-30R-1, 41 cm). The other bioevents that typically approximate the P/E boundary, the base of *Rhomboaster* spp. and the top of the *Fasciculithus richardii* group, could not be defined because specimens of these taxa were not observed. The absence of *Rhomboaster* spp. and *Tribrachiatus* spp. has been reported at onshore New Zealand sites of the same age (Kulhanek et al., 2015). The P/E boundary was therefore determined to be approximately within Sections 378-U1553C-31R-1 and 31R-2 and Section 378-U1553D-7R-1 in Biozone CNE1 (Agnini et al., 2014). The top of *Fasciculithus tympaniformis* (between Samples 378-U1553C-29R-2, 52 cm, and 29R-3, 42 cm [440.99 mbsf], and 378-U1553D-6R-7, 45 cm, and 6R-CC [447.64 mbsf]) and the presence of common to abundant *Discoaster multiradiatus* (between Samples 378-

Table T4. Radiolarian datums, Site U1553. T = top, B = bottom. (Continued on next page.) **Download table in CSV format.**

Datum	Age/Zone (base)	Age (Ma)	Core, section, interval (cm)		Depth CSF-A (mbsf)			
			Top	Bottom	Top	Bottom	Midpoint	±
			378-U1553A-	378-U1553A-				
	Barren Oligocene		2H-CC	3H-CC	12.79	22.121	17.46	4.67
T *Axoprunum? irregularis*	zRP17	26.12	2H-CC	3H-CC	12.79	22.12	17.46	4.67
T *Eucyrtidium antiquum*		27.68	6H-CC	7H-CC	50.45	60.27	55.36	4.91
B *Lychnocanium* aff. *conicum*	zRP16	29.52	7H-CC	8H-CC	60.27	69.73	65.00	4.73
B *Lamprocyclas matakohe*		30.00	11H-CC	12H-CC	98.15	107.21	102.68	4.53
B *Axoprunum? irregularis*	upper zRP15	31.50	17H-CC	18X-CC	138.52	148.02	143.27	4.75
T *Aphetocyrtis rossi*		31.50	17H-CC	18X-CC	138.52	148.02	143.27	4.75
T *Eucyrtidium spinosum*		32.00	19H-CC	20H-CC	157.35	167.00	162.17	4.83
B *Eucyrtidium antiquum*	zRP15 Eocene	33.50	23X-CC	24X-CC	179.39	185.22	182.31	2.91
B *Aphetocyrtis rossi*		37.00	23X-CC	24X-CC	179.39	185.22	182.30	2.91
B *Eucyrtidium spinosum*	zRP14	38.15	25X-CC	26X-CC	196.82	203.88	200.35	3.53
B *Lophocyrtis longiventer*		39.00	27X-CC		214.6		214.6	0.00
	Eocene		378-U1553C-	378-U1553C-				
B *Eucyrtidium spinosum*	zRP14	38.15	3R-CC	4R-CC	245.85	255.58	250.71	4.87
B *Lophocyrtis longiventer*		39.00	16R-CC	17R-CC	330.74	338.57	334.65	3.92
B *Zealithapium mitra*	zRP13	39.50	11R-CC	21R-CC	302.36	309.73	306.04	3.69
B *Eusyringium fistuligerum*	zRP12	42.85	16R-CC	17R-CC	330.74	338.57	334.65	3.92
T *Phormocyrtis striata striata*		47.00	23R-CC	25R-CC	383.33	403.96	393.64	10.31
T *Amphicraspedum prolixum* s.s.		48.80	19R-CC	21R-CC	352.74	364.57	358.65	5.91
B *Artobotrys auriculaleporis*		49.70	19R-CC	21R-CC	352.74	364.57	358.65	5.91
T *Buryella tetradica*	zRP10	51.00	27R-CC	28R-CC	421.73	437.48	429.60	7.88
B *Lychnocanium bellum*		53.20	23R-CC	25R-CC	403.96	412.45	408.20	4.25
B *Amphicraspedum prolixum* s.s.	zRP8 Paleocene	55.96	28R-CC	29R-CC	437.48	443.66	440.57	3.09
B *Buryella tetradica*	zRP5	62.40	29R-CC	30R-CC	443.66	445.79	444.72	1.06
B *Amphisphaera coronata* gr.		63.50	35R-CC	36R-CC	480.79	487.99	484.39	3.60
B *Buryella foremanae*	zRP4	64.00	35R-CC	36R-CC	480.79	487.99	484.39	3.60
B *Buryella granulata*	zRP3	64.90	35R-CC	36R-CC	480.79	487.99	484.39	3.60
			378-U1553E-	378-U1553E-				
	Barren Oligocene		2H-CC	3H-CC	18.115	26.825	22.47	4.36
T *Axoprunum? irregularis*	zRP17	26.12	2H-CC	3H-CC	18.12	26.83	22.47	4.36
T *Eucyrtidium antiquum*		27.68	3H-CC	4H-CC	26.83	36.71	31.77	4.94
B *Lychnocanium* aff. *conicum*	zRP16	29.52	8H-CC	9H-CC	66.74	76.44	71.59	4.85
B *Lamprocyclas matakohe*		30.00	13H-CC	14H-CC	108.94	119.80	114.37	5.43
B *Axoprunum? irregularis*	upper zRP15	31.50	16H-CC	17H-CC	139.10	146.96	143.03	3.93
T *Aphetocyrtis rossi*		31.50	18X-CC	19X-CC	158.04	163.53	160.78	2.75
T *Eucyrtidium spinosum*		32.00	18X-CC	19X-CC	158.04	163.53	160.78	2.75
B *Eucyrtidium antiquum*	zRP15 Eocene	33.50	20X-CC	21X-CC	172.83	183.17	178.00	5.17
B *Aphetocyrtis rossi*		37.00	24X-CC	25X-CC	206.14	214.28	210.21	4.07
B *Eucyrtidium spinosum*	zRP14	38.15	26X-CC	27X-CC	227.90	236.03	231.96	4.07
B *Lophocyrtis longiventer*	zRP13	39.00	27X-CC		236.03		236.03	0.00

U1553C-31R-2, 49 cm, and 31R-CC [449.93 and 451 mbsf] and Samples 378-U1553D-7R-1, 101 cm, and 7R-1, 128 cm [449.11 and 449.38 mbsf]) were used to constrain the P/E boundary. The nannofossil assemblage observed in this interval shows the characteristics of assemblages of the P/E transition interval already observed at the high-latitude reference section of ODP Site 690 (Bralower, 2002).

4.1.4. Paleocene

Nannofossil-bearing Paleocene sediments were recovered from 450 to ~470 mbsf in Hole U1553C (Cores 31R–34R) and from ~450 to ~470 mbsf in Hole U1553D (Cores 8R–10R). Nannofossil assemblages are generally poorly preserved (severe overgrowth and fragmentation) and scarce. The scattered presence or absence of most of the typical Paleocene marker species, such as the species belonging to *Discoaster* and *Heliolithus*, prevents a detailed biostratigraphic classification of the sediments (Figure **F24**). For example, the sporadic presence of *D. multiradiatus* in many samples in its range hampered the location of its first occurrence; therefore, the biohorizon base of *D. multiradiatus* (between Samples 378-U1553C-31R-CC and 32R-CC [454.61 mbsf] and 378-

Table T4 (continued).

Datum	Age / Zone (base)	Age (Ma)	Core, section, interval (cm)		Depth CSF-A (mbsf)			
			Top	Bottom	Top	Bottom	Midpoint	±
			378-U1553B-					
	Barren		3H-CC	4H-CC	24.37	35.05	29.71	5.34
	Oligocene							
T *Axoprunum? irregularis*	zRP17	26.12	3H-CC	4H-CC	24.37	35.05	29.71	5.34
T *Eucyrtidium antiquum*		27.68	3H-CC	4H-CC	24.37	35.05	29.71	5.34
B *Lychnocanium* aff. *conicum*	zRP16	29.52	8H-CC	9H-CC	67.96	77.65	72.81	4.84
B *Lamprocyclas matakohe*		30.00	11H-CC	12H-CC	96.86	105.75	101.30	4.45
B *Axoprunum? irregularis*	upper zRP15	31.50	14H-CC	16X-CC	125.14	140.74	132.94	7.80
T *Aphetocyrtis rossi*		31.50	14H-CC	16X-CC	125.14	140.74	132.94	7.80
T *Eucyrtidium spinosum*		32.00	17H-CC	18X-CC	150.52	157.34	153.93	3.41
B *Eucyrtidium antiquum*	zRP15	33.50	21X-CC	22X-CC	182.91	189.48	186.20	3.28
	Eocene							
B *Aphetocyrtis rossi*		37.00	24X-CC	25X-CC	198.80	208.20	203.50	4.70
B *Eucyrtidium spinosum*	zRP14	38.15	29X-CC		241.92		241.92	0.00
B *Lophocyrtis longiventer*		39.00						
	Eocene		378-U1553D-					
B *Eucyrtidium spinosum*	zRP14	38.15						
B *Lophocyrtis longiventer*		39.00						
B *Zealithapium mitra*	zRP13	39.50						
B *Eusyringium fistuligerum*	zRP12	42.85						
T *Phormocyrtis striata striata*		47.00						
T *Amphicraspedum prolixum* s.s.		48.80						
B *Artobotrys auriculaleporis*		49.70						
T *Buryella tetradica*	zRP10	51.00	3R-CC	4R-CC	412.91	426.81	419.86	6.95
B *Lychnocanium bellum*		53.20						
B *Amphicraspedum prolixum* s.s.	zRP8	55.96	5R-CC	6R-CC	436.91	447.78	442.34	5.44
	Paleocene							
B *Buryella tetradica*	zRP5	62.40	8R-CC	9R-CC	460.76	471.93	466.34	5.58
B *Amphisphaera coronata* gr.		63.50	11R-CC	12R-CC	488.13	497.42	492.77	4.64
B *Buryella foremanae*	zRP4	64.00	11R-CC	12R-CC	488.13	497.42	492.77	4.64
B *Buryella granulata*	zRP3	64.90	11R-CC	12R-CC	488.13	497.42	492.77	4.64
	Barren							
	Oligocene							
T *Axoprunum? irregularis*	zRP17	26.12						
T *Eucyrtidium antiquum*		27.68						
B *Lychnocanium* aff. *conicum*	zRP16	29.52						
B *Lamprocyclas matakohe*		30.00						
B *Axoprunum? Irregularis*	upper zRP15	31.50						
T *Aphetocyrtis rossi*		31.50						
T *Eucyrtidium spinosum*		32.00						
B *Eucyrtidium antiquum*	zRP15	33.50						
	Eocene							
B *Aphetocyrtis rossi*		37.00						
B *Eucyrtidium spinosum*	zRP14	38.15						
B *Lophocyrtis longiventer*	zRP13	39.00						

U1553D-7R-2, 27 cm, and 7R-2, 104 cm [450.06 mbsf]) should be considered to be poorly constrained at Site U1553. Nevertheless, the sediments between 450 and 470 mbsf in Holes U1553C and U1553D were assigned to a late and middle Paleocene age based on the presence of specimens of Paleocene species *Toweius*, the sporadic but sometimes common occurrence of *F. tympaniformis*, and the absence of *Heliolithus* spp. The presence of *F. tympaniformis* below the base of *D. multiradiatus* (base of Biozone NP9) implies a correlation to Biozones NP5–NP8 in the interval between ~450 and ~468 mbsf in Holes U1553C and U1553D, but these biozones cannot be differentiated because of the above-mentioned absence of any marker species of *Heliolithus*. Below 470 mbsf in Holes U1553C and U1553D, calcareous nannofossil abundance is very sparse, corresponding to a lithologic transition at ~480 mbsf from limestone (Unit IV) to muddy sandstone (Unit V) with low carbonate content (average = 2.2%). *Fasciculithus* spp. are present in Sample 378-U1553D-8R-CC, which implies a zonation of NP4 or younger, but they are absent in Sample 9R-CC, implying a correlation with lower NP4 or earlier biozones. The limited thickness (~20 m) of the recovered sediments from between 450 and 470 mbsf, which should correspond to Biozones NP8/9–NP5, relative to the estimated sedimentation rates of this interval (Figure **F60**), suggests the presence of a hiatus in the sedimentation at Site U1553 between the middle–late Paleocene Biozones NP8 and NP5. This is in agreement with the hiatus representing Biozones NP7 and NP8 proposed in Hollis et al. (2015) that resulted from detailed calcareous nannofossil investigation of DSDP Site 277 sediments. Deeper than 480 mbsf in Hole U1553C, in the dark grayish black siliciclastic Unit V (see **Lithostratigraphy**), single nannofossil specimens were occasionally observed, as at 548.57 mbsf (Sample 42R-3, 33 cm), where early Paleocene *Zeugrhabdotus sigmoides, Chiasmolithus danicus, Futyania petalosa*, and small *Prinsius* spp. occur. Two individual specimens of Cretaceous *Watznaueria* spp. were observed in Samples 36R-CC and 42R-3, 33 cm. The rareness of lower Paleocene and Cretaceous specimens suggests that these presences result from reworking within the siliciclastic Unit V. It is therefore not possible to constrain the stratigraphic position of

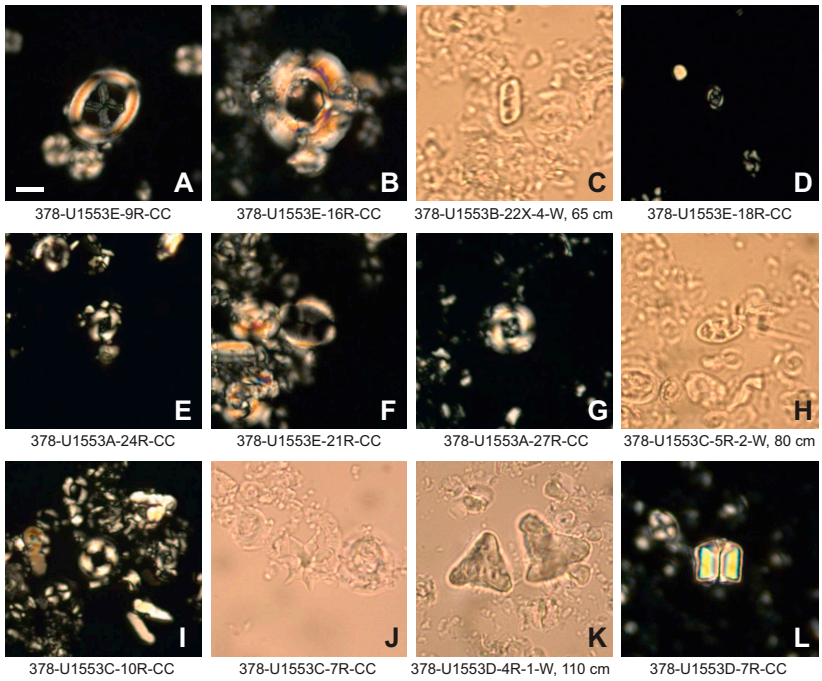

Figure F25. Selected calcareous nannofossil index species, Site U1553. Samples shown under crossed nicols unless otherwise noted. Scale bar = 5 µm. A. *Chiasmolithus altus*. B. *Reticulofenestra umbilicus*. Morphotype > 14 µm. C. *Isthmolithus recurvus*. D. *Clausicoccus subdistichus*. E. *Reticulofenestra daviesii*. F. *Reticulofenestra oamaruensis*. G. *Reticulofenestra reticulata*. H. *Neococcolithus dubius*. I. *Coccolithus formosus*. J. *Discoaster saipanensis*. Parallel light. K. *Tribrachiatus orthostylus*. Parallel light. L. *Fasciculithus tympaniformis*. For taxonomic information see Table T5 in the Expedition 378 Methods chapter (Röhl et al., 2022).

Table T5. Calcareous nannofossil distribution, Site U1553. **Download table in CSV format.**

Cores 378-U1553C-35R through 44R and 378-U1553D-12R through 20R and their proximity to the K/Pg boundary.

4.2. Planktonic foraminifers

At Site U1553, planktonic foraminifers are abundant and have moderate to good preservation in Holes U1553A, U1553B, and U1553E (Figure **F22**), whereas they are abundant in the upper part of Holes U1553C and U1553D and absent from both holes below ~460 mbsf, apart from an isolated occurrence in Sample 378-U1553C-40R-CC (see below). Test preservation is moderate in the upper part of Holes U1553C and U1553D and becomes poorer downhole starting at around 400 mbsf (Figure **F22**). Several biozones spanning the middle Oligocene to the late Paleocene were recognized at Site U1553 based on planktonic foraminifers (Figures **F23**, **F24**). Overall, planktonic foraminifers display low diversity assemblages and species compositions typical of high-latitude areas in the Oligocene to late Eocene, with notably small test sizes in some intervals in the Oligocene. In the middle to early Eocene, assemblages are more diverse and contain common muricate forms. Muricate planktonic foraminifers, such as *Acarinina* and *Morozovella*, are typical of tropical to subtropical latitudes but extend southward to the paleolocation of Site U1553 in the middle to early Eocene. The average planktonic:benthic (P:B) ratio is approximately 98%. In spite of the high P:B ratio, benthic foraminifers are relatively common at Site U1553 and have good preservation. Most of the species identified are epifaunal calcareous taxa, but there is an increased contribution of agglutinated taxa below 428 mbsf. The benthic foraminiferal species identified are useful for constraining the paleobathymetry at the site.

4.2.1. Overview of planktonic foraminifer biostratigraphy

We analyzed planktonic foraminifer assemblages for biostratigraphy in each core catcher sample from Site U1553, the deepest of which was from 581 mbsf (Sample 378-U1553D-20R-CC) (Figures **F23**, **F24**). Planktonic foraminifer marker species for the tropical zonation (Wade et al., 2011) are absent throughout. Thus, ages assigned to the investigated samples used the Austral zonation scheme of Huber and Quillévéré (2005). Four biozones were identified at the midpoint depths in Hole U1553A: middle Oligocene Biozones AO3 (44.59 ± 4.83 mbsf) and AO2 (84.05 ± 4.95 mbsf), early Oligocene Biozone AO1 (190.99 ± 5.8 mbsf), and late Eocene Biozone AE10 (below 196.79 mbsf to the bottom of Hole A) (Figure **F23**). Sample 1H-CC contains species ranging from the late

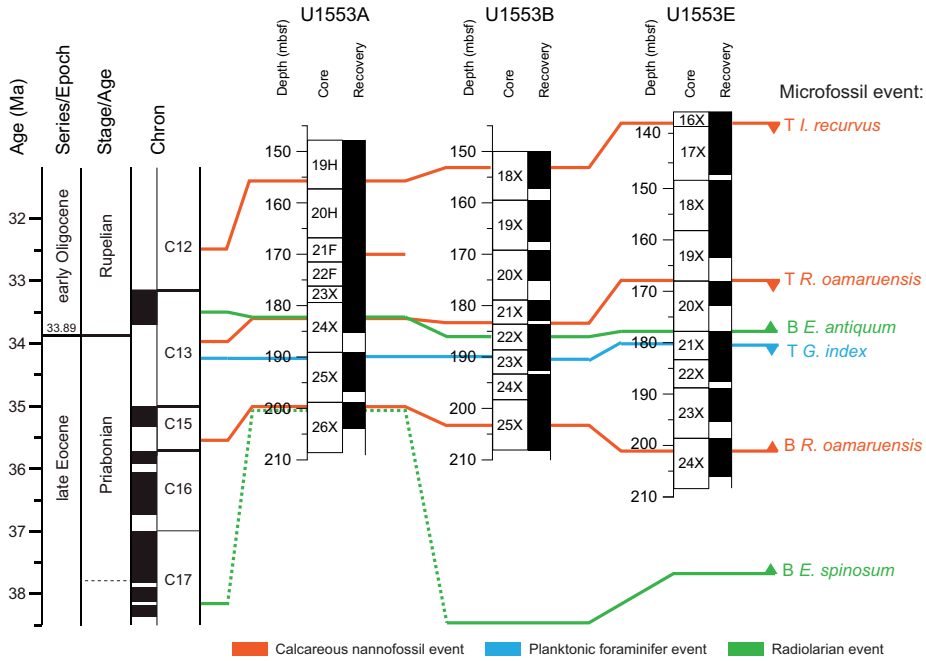

Figure F26. Biostratigraphy across the Eocene–Oligocene transition, Site U1553. Correlation is based on biohorizons by calcareous nannofossils, planktonic foraminifers, and radiolarians. T = top, B = base.

Pliocene to the Pliocene/Pleistocene boundary, such as *Truncorotalia crassula*, and forms that are transitional between *Globoconella puncticulata* and *Globoconella inflata* and were assigned to Biozone PL6. In Sample 2H-CC, reworked Pliocene–Pleistocene planktonic foraminifers are common and can be distinguished from the Oligocene assemblage by differences in preservation. Five biozones were identified at the midpoint depths in Hole U1553B: middle and early Oligocene Biozones AO3 (56.27 ± 2.46 mbsf), AO2 (82.27 ± 4.65 mbsf), and AO1 (191 ± 1.54 mbsf) and late Eocene Biozones AE10/AE9 (214.13 ± 21.56 mbsf) and AE8 (below 235.69 mbsf to the bottom of Hole B). Hole U1553E spans Biozones AO3 to AE8 considering the midpoint depths: middle and early Oligocene Biozones AO3 (31.74 ± 4.94 mbsf), AO2 (53.32 ± 2.27 mbsf), AO1 (117.97 ± 5.17 mbsf), and AE10/9 (210.18 ± 4.07 mbsf) and late Eocene Biozone AE8 (below 214.25 mbsf to the bottom of Hole E). The uppermost occurrence of *Globigerinatheka index* is recorded in Samples 378-U1553A-25X-CC, 378-U1553B-23X-CC, and 378-U1553E-21X-CC, indicating a latest Eocene age (top of AE10), and it is used to locate the E/O boundary in these holes. Thus, the E/O boundary occurs between Cores 378-U1553A-24X and 25X (185.19–196.79 mbsf), 378-U1553B-22X and 23X (189.45–192.54 mbsf), and 378-U1553E-20X and 21X (172.80–183.14 mbsf) (Figure **F26**), and it is poorly constrained based on only core catcher samples. Further sampling at higher resolution is required to pinpoint the E/O boundary in these holes. Holes U1553C and U1553D recovered sediments spanning the late Eocene to early Paleocene (Figure **F24**). Considering the midpoint depths, six biozones were recovered in Hole U1553C: middle Eocene Biozones AE8 (271.11 ± 5.97 mbsf), AE7 (334.63 ± 3.92 mbsf), AE6 (341.46 ± 2.91 mbsf), and AE5 (360.03 ± 4.51 mbsf); middle to early Eocene Biozone AE4 (378.85 ± 4.45 mbsf); and early Eocene Biozone AE3 (429.58 ± 7.88 mbsf). Four biozones were recovered in Hole U1553D (Figure **F24**): middle to early Eocene Biozone AE4/AE3 (419.83 ± 6.95 mbsf), early Eocene Biozones AE2 (431.84 ± 5.06 mbsf) and AE1 (450.61 ± 2.85 mbsf), and late Paleocene Biozone AP4 (below 453.46 mbsf). Samples 378-U1553C-30R-CC, 31R-CC, 378-U1553D-6R-CC, and 7R-CC span the P/E boundary at Site U1553 (Figure **F27**). Samples 378-U1553C-30R-CC and 31R-CC are heavily affected by dissolution, and the P/E boundary could not be located based on planktonic foraminifer biostratigraphy. We confirm the occurrence of the P/E boundary between Samples 378-U1553D-6R-CC and 7R-CC (447.76–453.46 mbsf) based on the base of *Globanomalina australiformis* (55.96 Ma) in Sample 6R-CC, which defines the top of the Paleocene in the Austral zonation of Huber and Quillévéré (2005).

4.2.2. Oligocene

The uppermost interval of Site U1553 comprises sediments of late Oligocene or younger age based on the absence of *Globoturborotalita labiacrassata*, the top of which defines the base of late Oligo-

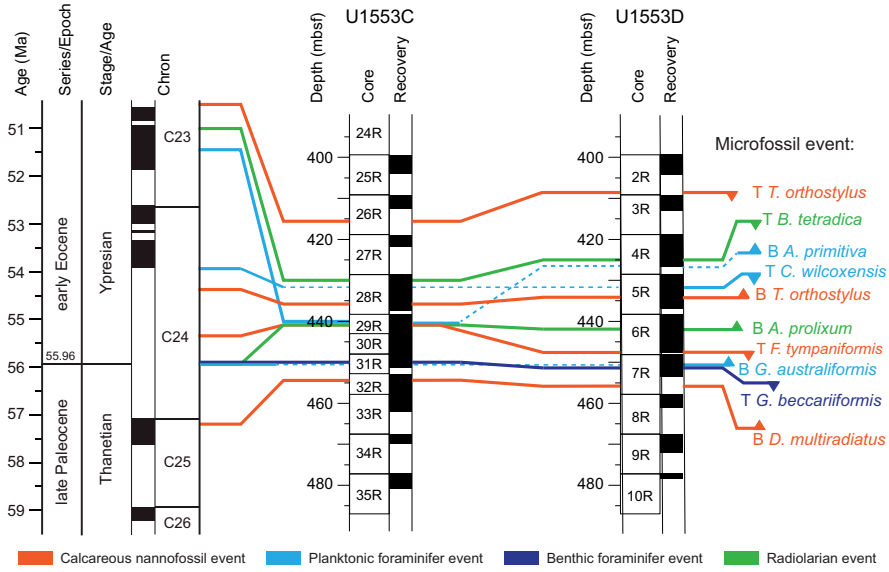

Figure F27. Biostratigraphy across the Paleocene–Eocene transition, Site U1553. Correlation is based on biohorizons by calcareous nannofossils, planktonic and benthic foraminifers, and radiolarians. T = top, B = base.

cene Biozone AO4. This datum lies between Samples 378-U1553A-3H-CC (22.24–22.29 mbsf) and 378-U1553B-2H-CC (15.18–15.23 mbsf) (Figure **F28**; Table **T6**). At Site U1553, common species in Biozone AO3 include *Subbotina eocaena, Subbotina corpulenta, Globoturborotalita paracancellata, Globoturborotalita eolabiacrassata, G. labiacrassata, Paragloborotalia nana, Paragloborotalia opima, Paragloborotalia pseudocontinuosa*, and *Globigerinella obesa*.

Chiloguembelina cubensis is a species commonly observed in high-latitude areas in the early to middle Oligocene, and its highest common (top common [Tc]) occurrence marks the base of Bio-

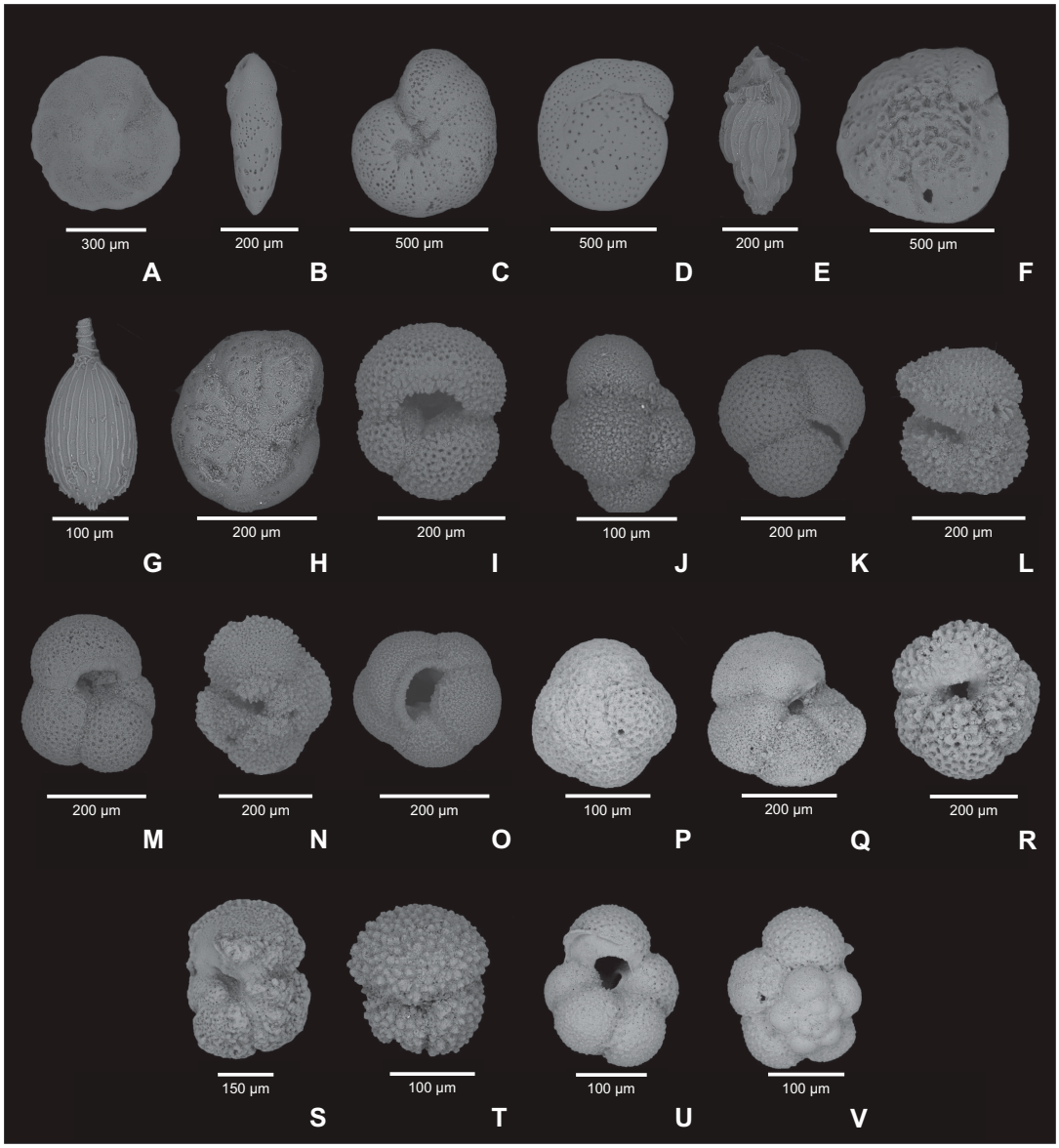

Figure F28. Foraminifer species. A. *Nuttalides truempyi* (U1553D-7R-CC). B. *Buliminoides chattonensis* (U1553B-2H-CC). C. *Anomalinoides orbiculus* (U1553D-7R-CC). D. *Cibicides maculatus* (U1553A-22X-CC). E. *Uvigerina bortotara* (U1553B-2H-CC). F. *Cibicides parki* (U1553B-29X-CC). G. *Lagena sulcata* (U1553B-2H-CC). H. *Gavelinella beccariiformis* (U1553C-31R-CC). I. *Globigerinatheka index* (U1553A-26X-CC). J. *Cassigerinelloita amekiensis* (U1553C-21R-CC). K. *Subbotina angiporoides* (U1553A-20H-CC). L. *Acarinina coalingensis* (U1553C-22R-CC). M. *Globoturborotalita labiacrassata* (U1553C-4R-CC). N. *Morozovella subbotinae* (U1553C-21R-CC). O, P. cf. *Neogloboquadrina pachyderma* (U1553C-40R-CC). Q. *Globanomalina australiformis* (U1553D-2R-CC). R. *Globigerinatheka senni* (U1553D-2R-CC). S. *Morozovella crater* (U1553D-2R-CC). T. *Acarinina primitiva* (U1553D-2R-CC). U, V. Unidentified planktonic foraminifers (U1553-40R-CC). For taxonomic information, see Table T19.

Table T6. Planktonic foraminifer distribution, Site U1553. **Download table in CSV format.**

zone AO3 (28.1 Ma). The Tc of *C. cubensis* is identified in Samples 378-U1553A-6H, 378-U1553B-7H, and 378-U1553E-4H (50.42–50.47, 58.72–58.77, and 36.68–36.73 mbsf, respectively). Planktonic foraminifer species observed in this interval include *P. nana, S. eocaena, Subbotina utilisindex*, and *G. labiacrassata*. Below this datum, the highest occurrence (top) of *Subbotina angiporoides* in Samples 378-U1553A-11H-CC, 378-U1553B-10H-CC, and 378-U1553E-7R-CC defines the base of Biozone AO2 (29.8 Ma). In this biozone, we observe common *S. utilisindex, G. labiacrassata, Globigerinella archaeobulloides*, and *Parasubbotina varianta*. In Biozone AO1, species diversity tends to decrease downhole, possibly linked to the stratigraphic and temporal proximity of the E/O boundary. Several samples in Biozone AO1 have planktonic foraminifer assemblages dominated by small planktonic taxa such as *C. cubensis, Tenuitella* spp., and *Pseudohastigerina* spp. This may indicate the presence of blooms linked to upwelling or shifts of the sub-Polar Front resulting in more nutrient-rich surface waters and higher productivity. See Table **T3** for the list of Oligocene planktonic foraminifer datums used in this study.

4.2.3. Eocene

The top of *Hantkenina alabamensis* (33.89 Ma) is the planktonic foraminifer datum that most closely approximates the E/O boundary. However, *H. alabamensis* does not occur in the investigated core catcher samples, likely because this species was restricted to lower latitudes in the Eocene. Shipboard biostratigraphy using only core catcher samples has a relatively coarse resolution, however, and subsequent higher resolution studies might reveal the occurrence of *H. alabamensis*, allowing a more precise definition of the E/O boundary. Following the Austral zonation scheme of Huber and Quillévéré (2005), we use the top of *G. index* (34.60 Ma) between Samples 378-U1553A-24H-CC and 25H-CC, 378-U1553B-22H-CC and 23X-CC, and 378-U1553E-20R-CC and 21R-CC to provide an estimate of the stratigraphic position of the E/O boundary (Figures **F26**, **F28I**). The top of *G. index* marks the boundary between Biozones AO1 and AE10. Biozone AE10 has a short duration, and it was not possible to detect the base of this biozone, which is marked by the top of *Tenuitella insolita*. We therefore could not distinguish the boundary between Biozones AE10 and AE9. Common species observed in this interval are *G. index, S. angiporoides, Subbotina linaperta, Turborotalia ampliapertura, Catapsydrax unicavus*, and *Pseudohastigerina wilcoxensis*. We estimated the base of late Eocene Biozone AE9 based on the top of *Globigerinatheka barri* in Samples 378-U1553B-28X-CC, 378-U1553E-25X-CC, and 378-U1553C-5R-CC. This species and the majority of *Globigerinatheka* species (other than *G. index*) are reported to range up to the upper part of Biozone AE8 (Pearson et al., 2006). Common planktonic foraminifers in underlying Biozone AE8 include *G. index, Subbotina gortanii, S. linaperta, S. eocaena,* and *S. angiporoides*.

The uppermost part of Hole U1553C (265.8–255.56 mbsf) consists of late Eocene samples, which were assigned to Biozone AE8 (see above). The top of *Acarinina primitiva* (39.1 Ma) marks the boundary between Biozones AE8 and AE7 between Samples 5R-CC and 6R-CC. Biozone AE7 spans the mid-Bartonian to early Lutetian (39.1–42.11 Ma), defining the transition from the late to the middle Eocene at Site U1553. It is characterized by a distinct increase in species diversity and test size compared to the sediments spanning the late Eocene to early Oligocene. Large *Globigerinatheka* typical of middle Eocene tropical to subtropical assemblages—*G. index, G. barri*, and *Globigerinatheka subconglobata*—are common in this biozone, together with *A. primitiva* and *Acarinina collactea* and subbotinids such as *S. angiporoides, S. linaperta, S. eocaena*, and large *Turborotalia frontosa*. A similar assemblage characterizes Biozones AE6 and AE5. AE6 is a short duration biozone that extends from the base of *S. angiporoides* in Sample 17R-CC to the base of *G. index* in Sample 18R-CC. The base of Biozone AE5 is defined by the top of *Cassigerinelloita amekiensis* in Samples 378-U1553C-21R-CC and 378-U1553D-2R-CC. This extremely small species (Figure **F28J**) was reported as a distinctive and common stratigraphic marker in middle Eocene planktonic foraminifer assemblages on the Kerguelen Plateau in the Indian sector of the Southern Ocean (Huber and Quillévéré, 2005). Because of its small size, we performed a dedicated search for this species in Hole U1553A. This allowed us to report it for the first time in the ocean region offshore New Zealand, confirming its stratigraphic utility for the southern subpolar region. Biozone AE4 marks the transition to the upper Ypresian and is characterized by the uppermost occurrence of the genus *Morozovella* at Site U1553. In particular, the top of *Morozovella crater* is recorded in Samples 378-U1553C-22R-CC and 378-U1553D-3R-CC. Magneotobiochronology in

the mid-Waipara section (New Zealand) indicates an age of 45.7 Ma for this datum (Raine et al., 2015; Dallanave et al., 2016). However, its uppermost occurrence at Site U1553 (within the core catcher samples) appears to be no younger than 46.13 Ma and not older than 50.04 Ma based on planktonic foraminifer datum events in adjacent cores. Between Samples 378-U1553C-22R-CC and 23R-CC, we identify the base of *C. amekiensis*, which marks the boundary between Biozones AE4 and AE3. Species commonly observed in Biozone AE3 are *A. primitiva, A. collactea, Subbotina lineaperta, Subbotina rosnaesensis, S. eocaena, Subbotina senni, Subbotina crociapertura, S. corpulenta*, and *G. australiformis*. We identified the boundary between Biozones AE3 and AE2 between Samples 378-U1553C-27R-CC and 28R-CC and 378-U1553D-3R-CC and 4R-CC where we place the biohorizon base *A. primitiva*. This species (Figure **F28T**) evolved from *Acarinina coalingensis* (Figure **F28L**) in the early Eocene, and the two species coexisted for roughly 2 My and exhibit strong morphological intergradation. Our identification of the base of *A. primitiva* in the above intervals is based on the occurrence of the lowermost convincing specimens of *A. primitiva* in Samples 378-U1553C-27R-CC and 378-U1553D-3R-CC and the occurrence of the uppermost definitive specimens of *A. coalingensis* in Samples 378-U1553C-28R-CC and 378-U1553D-4R-CC. Other species common in this interval are *Acarinina esnehensis, Acarinina pseudotopilensis, A. collactea, P. wilcoxensis, S. linaperta, S. eocaena, Chiloguembelina wilcoxensis*, and *G. australiformis*. Species belonging to the genus *Morozovella* commonly occur between Samples 378-U1553C-22R-CC and 26R-CC and 378-U1553D-2R-CC and 4R-CC, confirming previous studies that indicate this genus, generally reported as confined to tropical to subtropical latitudes (Pearson et al., 2006), extends its range poleward to subpolar latitudes during the acme of the Cenozoic warmth (Jenkins, 1975; Hollis et al., 1997). *Morozovella* species commonly observed within this interval in Holes U1553C and U1553D are *M. crater, Morozovella gracilis, Morozovella subbotinae*, and *Morozovella lensiformis*. Rare *Morozovella aragonensis* were also observed.

Between 46 and 52 Ma, planktonic foraminifer preservation decreases substantially. Between Samples 378-U1553C-27R-CC and 30R-CC and 378-U1553D-5R-CC and 7R-CC, there are clear signs of dissolution. Planktonic foraminifer assemblages are dominated by subbotinids, and dissolution-prone muricate forms decrease in abundance and diversity. The upper part of this interval, around 400 mbsf, coincides with a decrease in bulk sediment $CaCO_3$ wt% in Holes U1553C and U1553D. We cannot assign a biozone to Samples 378-U1553C-29R-CC to 32R-CC because of the scarcity of specimens and their poor preservation. The decrease in preservation in Hole U1553D starts about 15 m deeper than in Hole U1553C, and we tentatively place the Biozone AE2/AE1 boundary between Samples 378-U1553D-4R-CC and 378-U1553C-5R-CC. This is based on the disappearance of *C. wilcoxensis*, which occurs in the samples immediately above that biozone and which may represent biohorizon top *C. wilcoxensis* (53.94 Ma). A higher resolution study will be required to confirm the presence of the Biozone AE2/AE1 boundary at Site U1553.

See Table **T3** for the list of Eocene planktonic foraminifer datums used in this study.

4.2.4. Paleocene

Calcareous nannofossil and benthic foraminifer data indicate the occurrence of the P/E boundary between Cores 378-U1553C-30R and 31R and Samples 378-U1553D-6R-CC and 7R-CC. Planktonic foraminifers are rare and poorly preserved in Samples 378-U1553C-30R-CC and 31R-CC, and Sample 32R-CC is barren of planktonic foraminifers. We therefore could not confirm this interpretation using planktonic foraminifers. We assigned a late Paleocene age to Sample 378-U1553D-7R-CC based on the absence of *G. australiformis*. The top of *G. australiformis* marks the boundary between Biozones AE1 and AP4 and is calibrated at 55.96 Ma. This species consistently occurs in the Eocene samples from Hole U1553D despite the decrease in preservation. We therefore consider the disappearance of *G. australiformis* a reliable datum in Hole U1553D and confirm the occurrence of the P/E boundary between Samples 6R-CC and 7R-CC (447.76–453.46 mbsf) (Figure **F26**). We observed an increase in species diversity along with an improvement of planktonic foraminifer preservation in Sample 8R-CC. This sample is characterized by a Paleocene assemblage with common *Acarinina nitida, A. coalingensis, A. collactea, Acarinina subglobosa, Igorina pusilla, Subbotina velascoensis, Subbotina triangularis, Parasubbotina variospira*, and *P. wilcoxensis*, and we assign it to Biozone AP4. In this sample, we also observed a decrease in the P:B ratio to 77%. This points to a decrease in paleodepth

rather than an increase in dissolution because preservation improves in this sample and planktonic foraminifers are more abundant than in the previous, poorly preserved samples. Also, this decrease is consistent with a benthic foraminifer assemblage indicative of a shallower paleodepth than overlies in, for example, middle bathyal (see below). Sample 8R-CC may indicate the transition to a time interval characterized by a paleodepth remarkably shallower in this area because core catcher samples are barren in planktonic foraminifers to the bottom of Hole U1553D. This transition also coincides with the abrupt change in lithology from chalk to mudstone observed at the same depth (Figure **F24**; see **Lithostratigraphy**). In the dark grayish black siliciclastic Unit V, which starts at about 477 mbsf in Holes U1553C and U1553D, the only sample containing planktonic foraminifers is Sample 378-U1553C-40R-CC at 528.11 mbsf. This sample contains few specimens of well-preserved planktonic foraminifers, two specimens of unidentified microperforate form (Figure **F28U, F28V**), and six specimens that resemble *Neogloboquadrina pachyderma* (Figure **F28O, F28P**). The presence of *N. pachyderma*, whose first or lowest occurrence is in the late Miocene, possibly indicates downhole contamination within this unit.

4.3. Benthic foraminifers

Benthic foraminifer abundance and preservation were qualitatively analyzed for Site U1553 (Figure **F22**). The abundance ranges from few to rare; only in Sample 378-U1553C-44R-CC were they abundant. Benthic foraminifers are barren below 500 mbsf in Hole U1553D. Preservation is very good in the Pleistocene, Oligocene, and Eocene and ranges from very good to poor in the Paleocene. Samples are mostly dominated by calcareous taxa (Table **T7**; Figure **F28**). Although few agglutinated taxa, such as *Bathysiphon, Gaudryina*, and *Siphotextularia*, are recorded in the latest Paleocene, agglutinated taxa are an important component of assemblages in the earlier Paleocene.

During the Pleistocene, Oligocene, and Eocene, epifaunal taxa are dominant, and the assemblages include *Anomalinoides* sp., *Cibicides* sp., *Gyroidinoides* sp., *Hanzawaia scopus*, and *Nuttallides* sp. Although epifaunal dominance indicates a highly oxygenated environment, the constant presence of infaunal taxa (such as bolivinids, buliminids, *Globocassidulina* sp., *Lagena sulcata*, *Lenticulina* sp., nodosariids, *Oridorsalis umbonatus*, *Pullenia* sp., *Trifarina* sp., and *Uvigerina* sp.) suggests relatively high productivity.

The assemblages in Samples 378-U1553C-31R-CC and 378-U1553D-7R-CC are also dominated by epifaunal taxa and have greater relative abundances of infaunal species such as *Bathysiphon* spp. and *Loxostomoides* sp. The last appearance of *Gavelinella beccariiformis* occurs in these two samples, indicating that the P/E boundary lies in Cores 378-U1553C-31R and 378-U1553D-7R. Underlying Paleocene assemblages are dominated by infaunal taxa and agglutinated species (such as *Bathysiphon* spp. and *Spiroplectammina* sp.), the presence of which may suggest deposition in low oxygen conditions and a mesotrophic paleoenvironment.

The continuous presence of *Laticarina pauperata* in the Oligocene interval and the abundance of *Gyroidinoides neosoldanii, Pullenia bulloides, Anomalinoides aotea*, and *O. umbonatus* during the Eocene confirms sediment deposition at lower bathyal depths (Hollis et al., 1997; Hayward et al., 2010). In the Paleocene interval (Samples 378-U1553C-31R-CC to 44R-CC and 378-U1553D-7R-CC to 12R-CC), a mid–lower bathyal paleodepth is inferred by the occurrence of *Bathysiphon* spp., *G. beccariiformis*, and *Nuttallides truempyi* (Tjalsma and Lohmann 1983; Hornibrook et al., 1989; Alegret and Thomas, 2013). Redeposition of Paleocene or older sediments is suggested by the frequent presence of large, broken specimens of the genus *Lenticulina*, which is inferred to have been derived from shelf environments (e.g., in Samples 378-U1553C-35R-CC and 378-U1553D-9R-CC to 12R-CC). A similar occurrence of this genus in deepwater settings was reported by Sutherland et al. (2019) for IODP Expedition 371 sediments. The presence of bryozoan fragments in Samples 378-U1553C-35R-CC and 378-U1553D-11R-CC also suggests downslope redeposition of shelf sediments.

Table T7. Benthic foraminifer distribution, Site U1153. **Download table in CSV format.**

4.4. Radiolarians

Radiolarians are abundant and very well preserved in the Oligocene and late Eocene at Site U1553. They are rare but still well preserved in the middle Eocene. In the early Eocene and Paleocene, radiolarian occurrence is sporadic, many samples are barren, and preservation is poor. In some early Eocene samples, however, radiolarians are very abundant but very poorly preserved. Trends in radiolarian abundance and preservation in Holes U1553A and U1553B are shown in Figure **F22**. In several samples in the lower Oligocene and upper Eocene, black overgrowths are present on some radiolarian tests and sponge spicules and are inferred to be pyrite (Figure **F29O**).

Because low-latitude index species are absent or very rare, radiolarian assemblages have been correlated to the Southwest Pacific zonation, which has been recently revised (Hollis et al., 2017; C.J. Hollis, unpubl. data; Sutherland et al., 2019). This zonation incorporates the Oligocene–late Eocene Southern Ocean zonation of Funakawa and Nishi (2005). The radiolarian succession has been correlated to Biozones zRP16–zRP3 (early late Oligocene to early Paleocene) (Table **T4**). The following description of the downhole biostratigraphy is based on preliminary assessment of core catcher samples in all five holes at Site U1553. The radiolarian occurrence tables for each hole (Table **T8**) and database information should not be considered to be a full census of species present because shipboard analysis focused on identifying key species (Figure **F29A–F29N**).

4.4.1. Neogene

The uppermost cores from Holes U1553A, U1553B, and U1553E are barren of radiolarians (i.e., Cores 378-U1553A-1H and 2H, 378-U1553B-1H through 3H, and 378-U1553E-1H and 2H) (Table **T4**).

4.4.2. Oligocene

Very well preserved and abundant Oligocene radiolarians occur in the upper part of Holes U1553A, U1553B, and U1553E from ~20 to ~125 mbsf (Cores 378-U1553A-3H through 13H, 378-U1553B-4H through 13H, and 378-U1553E-3H through 13H). Diatoms and sponge spicules are also abundant in this interval, and silicoflagellates are noted in most samples. Between ~120 and 130 mbsf (Cores 14H and 15H in Holes U1553A, U1553B, and U1553E), radiolarians and diatoms are very rare or absent. In the underlying Oligocene interval (~130 to ~180 mbsf), radiolarians are common and well preserved, but diatoms are relatively rare.

In Cores 378-U1553A-3H through 7H, the co-occurrence of *Lychnocanium* aff. *conicum* (*Lychnocanoma conica* in the sense of Abelmann, 1990) and *Axoprunum*? *irregularis* indicates a correlation with early late Oligocene Biozone zRP16 (Table **T4**). It is possible that the index species for Biozone zRP17, *Clinorhabdus robusta*, occurs in this interval, but it has yet to be confidently identified. Assemblages in this biozone include numerous reworked radiolarians of middle Eocene age, including *Artobotrys auriculaleporis, Eusyringium fistuligerum, Periphaena decora*, and *Theocampe mongolfieri*. It is notable that although the first three species are common in the middle Eocene at this site, *T. mongolfieri* has yet to be discovered in situ in the middle Eocene assemblages. Two Cretaceous–Paleocene species were also encountered in this biozone: *Amphipyndax stocki* and *Amphipternis alamedaensis*. All reworked specimens are well preserved and, without knowledge of their upper range limits, cannot currently be differentiated from in situ Oligocene species.

For underlying Biozone zRP15, we use the lowest occurrence (base) of *A*? *irregularis* in Sample 378-U1553A-17H-CC to divide the biozone into upper and lower parts. The highest occurrences (tops) of *Aphetocyrtis rossi* and *Eucyrtidium spinosum* are coincident and slightly below this datum, respectively (Table **T4**). Another useful datum identified in this study is the base of *Lamprocyclas matakohe*, which occurs within the upper part of Biozone zRP15. This datum is not calibrated beyond the New Zealand region, but the age-depth model for DSDP Site 277 indicates an age of ~30 Ma (Hollis et al., 1997, 2017; C.J. Hollis, unpubl. data). The base of Biozone zRP15 is identified by the base of *Eucyrtidium antiquum* in Core 378-U1553A-23X. The event was previously found to occur at the Runangan/Whaingaroan local stage boundary at Site 277 (Hollis et al., 1997), which coincides with the base of nannofossil Biozone NP21 in the latest Eocene. Here, we use the datum to identify the approximate position of the E/O boundary at ~180 mbsf.

An equivalent downhole succession of Oligocene radiolarian datums is observed in Cores 378-U1553B-4H through 23X and 378-U1553E-3H through 20H (Table **T4**).

4.4.3. Eocene

Radiolarian-bearing Eocene sediments are present in all five holes at Site U1553. Radiolarians are common and well preserved in the late Eocene, rare but still relatively well preserved in the middle Eocene, and generally rare and poorly preserved in the early Eocene. Sponge spicules remain common in the Eocene, but diatoms are rare and silicoflagellates are seldom observed.

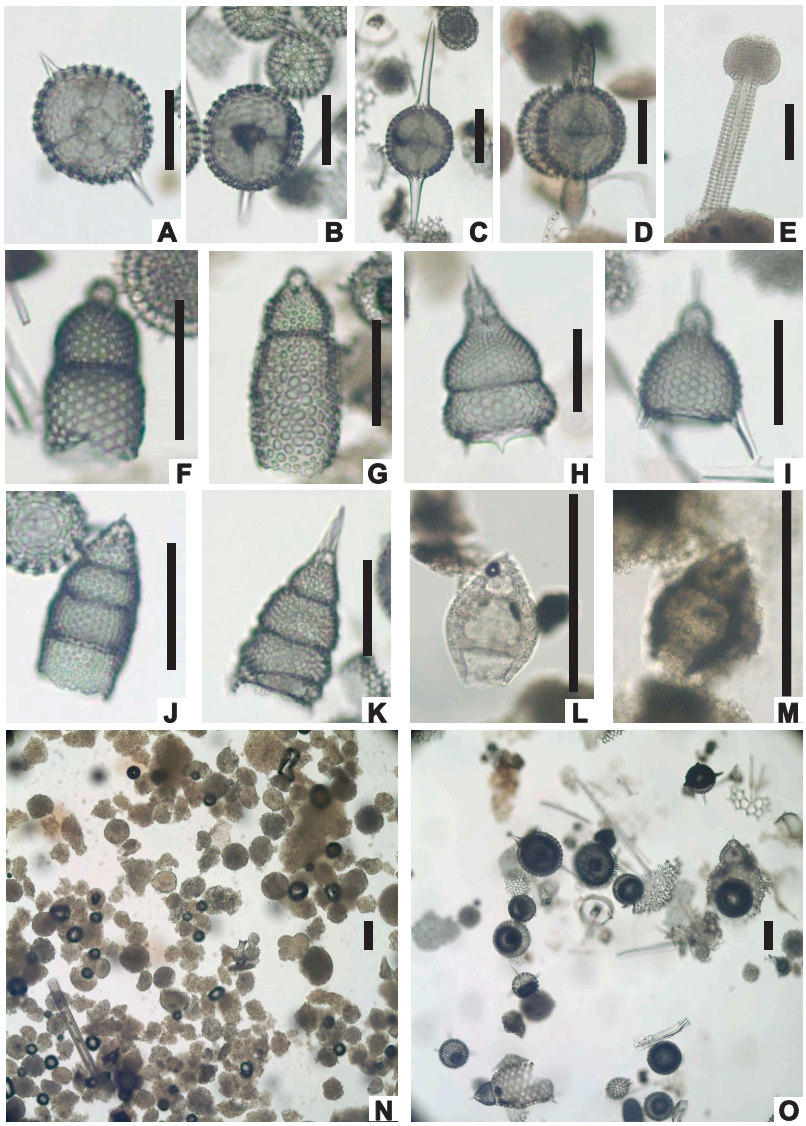

Figure F29. Selected radiolarian index species and radiolarian assemblages. Scale bar = 100 µm. Specimen locations are identified by slide letter and England Finder location. A. *Axoprunum? irregularis* (378-U1553E-4H-CC; B-M47/4). B. *Axoprunum bispiculum* (378-U1553D-7R-CC; A-S37/0). C. *Axoprunum pierinae* gr. (378-U1553E-23X-CC; B-W28/2). D. *Axoprunum* aff. *pierinae* (378-U1553E-26H-CC; A-D28/0). E. *Amphicraspedum prolixum* s.s. (378-U1553D-2R-CC; A-Q46/1). F. *Aphetocyrtis gnomabax* (378-U1553E-21X-CC; A-E40/1). G. *Aphetocyrtis rossi* (378-U1553E-23X-CC; A-W19/0). H. *Lamprocyclas matakohe* (378-U1553E-5H-CC; A-T11/1). I. *Lychnocanium* aff. *conicum* (378-U1553-7H-CC; A-E36/4). J. *Eucyrtidium antiquum* (378-U1553E-9H-CC; A-W41/1). K. *Eucyrtidium spinosum* (378-U1553-23X-CC; B-O4/1). L. *Buryella tetradica* (378-U1553D-5R-CC; A-W17/4). M. *Buryella foremanae* (378-U1553D-9R-CC; A-Y42/4). N. Radiolarians with poor preservation (378-U1553C-29R-CC). O. Pyritized radiolarians (378-U1553B-23X-CC). For taxonomic information, see Table T7 in the Expedition 378 methods chapter (Röhl et al., 2022).

Table T8. Radiolarian distribution, Site U1553. **Download table in CSV format.**

In Holes U1553A, U1553B, and U1553E, the top of the Eocene is placed at the base of *E. antiquum*, which corresponds to the top of Biozone zRP14 at ~180 mbsf. The base of Biozone zRP14 is identified by the base of *E. spinosum* in Core 378-U1553A-25X. This marker species was not encountered in the depauperate and poorly preserved assemblages in the underlying two cores in Hole U1553A. The samples are assigned to the Biozone zRP12–zRP14 interval based on the presence of *Lophocyrtis longiventer*, a species with a poorly defined base in the lower part of middle Eocene Biozone zRP12.

In Hole U1553B, the interval from Core 22X to the bottom of the hole in Core 29X is correlated with Biozone zRP14 based on the presence of *E. spinosum* and absence of *E. antiquum*. The observation that Biozone zRP14 extends to 241.92 mbsf in Hole U1553B suggests that the absence of *E. spinosum* in the lowest two samples in Hole U1553A is an artifact of the poor preservation and low abundance of radiolarians.

In Hole U1553E, Biozone zRP14 extends from Core 21X through Core 26X. As with Hole U1553A, a poorly preserved assemblage in basal Core 27X contains *L. longiventer* and is therefore provisionally assigned to Biozones zRP12–zRP14.

Radiolarians are relatively rare but well preserved in the middle Eocene in Hole U1553C (Cores 4R–16R). Middle Eocene Biozones zRP13 and zRP12 are identified by their primary datums: the base of *Zealithapium mitra* in Core 11R and the base of *E. fistuligerum* in Core 16R. Below this level, radiolarians are generally rare and poorly preserved, and early Eocene biozones are poorly constrained. The interval from the base of *E. fistuligerum* to the top of *Buryella tetradica* is correlated to Biozones zRP10 and zRP11 (Cores 17R–27R). The top of *B. tetradica* defines the top of Biozone zRP9. The primary marker for Biozone zRP11, *Eusyringium lagena*, was not found at Site U1553, nor was it recorded in DSDP Site 277 assemblages (Hollis et al., 1997; C.J. Hollis unpubl. data). Cores 28R–30R contain abundant, very poorly preserved spumellarians (Figure **F29N**), which are a feature of earliest Eocene assemblages of PETM sections in New Zealand (Mead Stream) (Hollis, 2006) and the northwest Atlantic (IODP Expedition 342) (Norris et al., 2014). We tentatively correlate these assemblages with earliest Eocene Biozone zRP8. A primary datum for the base of the biozone, the base of *Amphicraspedum prolixum* s.s., occurs in the uppermost core in this interval (Core 28R).

Hole U1553D contains an early Eocene radiolarian succession equivalent to that described for Hole U1553C. Sparse and relatively poorly preserved assemblages in the upper two cores (378-U1553D-2R and 3R) are correlated with Biozones zRP10 and zRP11 based on the absence of both *B. tetradica* and *E. fistuligerum*. The underlying two cores (4R and 5R) are correlated with Biozones zRP8 and zRP9 based on the co-occurrence of *A. prolixum* s.s. and *B. tetradica*. The next two underlying cores (6R and 7R) are tentatively correlated with Biozone zRP8 based on the abundance of poorly preserved spumellarians. Therefore, the P/E boundary is tentatively placed at the base of Core 7R.

4.4.4. Paleocene

Radiolarians are rare and relatively poorly preserved in the Paleocene in Holes U1553C and U1553D. Below the interval of abundant spumellarians in Hole U1553C, we tentatively correlate four cores (31R–34R) that contain poorly preserved assemblages with late Paleocene Biozones zRP5–zRP7 based on the low spumellarian abundance and the absence of early Paleocene marker species. Despite poor preservation, the assemblage in the lowest radiolarian-bearing core in Hole U1553C (35R) can be assigned to Biozone zRP4 based on the presence of the primary index species, *Buryella foremanae*, and the absence of the index species for the overlying biozone, *B. tetradica*.

Hole U1553D contains an equivalent Paleocene succession. Core 8R is correlated with Biozones zRP5–zRP7 based on the presence of *B. tetradica* and absence of early Paleocene index species. Cores 378-U1553D-9R through 11R are correlated with early Paleocene Biozone zRP4 based on the presence of the primary index species, *B. foremanae*, and the absence of *B. tetradica*. Because of the sparse and poorly preserved assemblages in this interval, we are unable to confirm the presence or absence of the late Paleocene unconformity identified by Hollis et al. (2014, 2015).

4.5. Ichthyoliths

Ichthyoliths (isolated fish teeth and shark scales) were found in low abundance throughout the sedimentary sequence at Site U1553. Specific occurrences were noted in the following foraminifer core catcher samples: 378-U1553A-4H-CC; 378-U1553B-3H-CC, 17H-CC, and 20X-CC; 378-U1553C-2R-CC, 3R-CC, 5R-CC, 19R-CC, 21R-CC, 22R-CC, 25R-CC, and 40R-CC; 378-U1553D-5R-CC, 6R-CC, and 9R-CC; and 378-U1553E-8H-CC, 19X-CC, 23X-CC, 25X-CC, and 27X-CC. These occurrences are likely to underestimate the frequency of ichthyolith occurrence because they are incidental findings in samples that were not processed specifically for ichthyoliths. Several large (>5 mm) ichthyoliths were found during core description upon inspection of archive half sections in Lithostratigraphic Units II and III.

Although ichthyoliths are relatively rare throughout the sequence, there is a concentrated horizon of ichthyoliths in Sample 378-U1553D-9R-CC. This sample is barren of planktonic foraminifers, but ichthyoliths are more abundant than anywhere else observed in the overlying units. This assemblage can be differentiated according to the morphological scheme of Sibert et al. (2018) into four age-diagnostic morphotypes:

- Large long curved bladed cone (Late Cretaceous to ~60 Ma);
- Pointy flare bottom, wide (Late Cretaceous to ~62 Ma);
- Clear, concave tooth, ¼ root, a rare morphotype that ranges from Early to Late Cretaceous (some evidence suggests that it ranges into the early Paleocene); and
- Bladed cone, curved, a morphotype restricted to the early Paleocene (~62 to ~60 Ma).

This assemblage is devoid of any morphotypes restricted to the Late Cretaceous, and the combination of age ranges converges on an age estimate of ~62 Ma, which is in broad agreement with radiolarian biostratigraphy for Hole U1553D, which places Sample 378-U1553D-9R-CC in the upper part of Biozone zRP4 (64–62.4 Ma; Table **T4**).

4.6. Dinoflagellate cysts

A shore-based study of dinoflagellate cysts (dinocysts) was undertaken to improve the age control of Paleocene Lithostratigraphic Unit V and, specifically, to determine if the unit spanned the K/Pg boundary. Thirteen core catcher samples from Site U1553D (8R-CC to 20R-CC) were examined. All samples contain relatively abundant dinocyst assemblages. Preservation is moderately good, although palynomorphs are pale and fragmented in some samples. The dinocyst succession examined from Site U1553D has been correlated to Biozones NZDP1 and NZDP2 to NZDP6 and NZDP7 (early to early late Paleocene) within the New Zealand zonation of Crouch et al. (2014).

4.6.1. Paleocene

Sample 378-U1553D-8R-CC (460.74–460.77 mbsf) is correlated with Biozones NZDP6 and NZDP7 based on the common presence of the *Eisenackia reticulata* group and the absence of key dinocyst taxa that are present in the underlying sample (9R-CC) that indicate Biozone NZDP5. This sample contains more abundant representatives of genera that indicate an open ocean, or more distal, setting, such as *Impagidinium*, *Cerebrocysta*, and *Spiniferites* (e.g., Sluijs et al., 2005), than samples stratigraphically below it (particularly from Sample 10R-CC and lower samples).

Samples 378-U1553D-9R-CC to 14R-CC (471.91–471.94 to 517.59–517.62 mbsf) are correlated with early Paleocene Biozones NZDP4 and NZDP5. The presence of *Deflandrea foveolata*, *Isabelidinium cingulatum*, and *Alterbidinium pentaradiatum* in Sample 9R-CC suggests Biozone NZDP5. The primary marker for the base of Biozone NZDP5, *D. foveolata*, is only recognized in Sample 9R-CC, making it difficult to confidently identify the NZDP4/NZDP5 biozone boundary. A secondary datum that occurs close to the NZDP4/NZDP5 zonal boundary is the top of *Palaeoperidinium pyrophorum*; this datum is recorded in Sample 11R-CC (488.11–488.14 mbsf), which provides a tentative correlation for the base of Biozone NZDP5. The base of *I. cingulatum* is recorded in Sample 13R-CC (507.66–507.69 mbsf), indicating lower Biozone NZDP4, and *A. pentaradiatum* is present through the interval correlated to Biozones NZDP4 and NZDP5 (Samples 9R-CC to 14R-CC). Through most of this interval, the dinocyst assemblage contains common to frequent occurrences of taxa more indicative of coastal to neritic settings, such as *Areoligera* and

Glaphyrocysta spp. A peak in the abundance of the peridinioid genus *Spinidinium* is observed in Samples 12R-CC and 13R-CC (497.40–497.43 and 507.66–507.69 mbsf, respectively).

Samples 378-U1553D-15R-CC to 17R-CC (528.57–528.62 to 553.79–553.84 mbsf) are correlated with Biozone NZDP3 based on the presence of *Senoniasphaera inornata*, common to abundant occurrence of *P. pyrophorum*, and the top of *Vozzhennikovia angulata* in Sample 16R-CC. The top of *S. inornata*, the primary marker for the NZDP3/NZDP4 zonal boundary, is seen in Sample 15R-CC. Taxa indicative of coastal to neritic settings, *Areoligera* and *Cordosphaeridium* spp., are common to frequent, and peridinioid taxa are abundant in this interval.

The lowermost samples examined from Site U1553D (18R-CC to 20R-CC; 564.90–581.16 mbsf), appear to be early Paleocene, and this interval is correlated with Biozones NZDP1 and NZDP2. Sample 18R-CC contains well-preserved specimens of *Trithyrodinium evittii*, a species with its lowest occurrence in the earliest Paleocene in New Zealand (Willumsen, 2011; Taylor et al., 2018). The base of *A. pentaradiatum* is also observed in Sample 18R-CC, which occurs within Biozone NZDP2. Samples 19R-CC and 20R-CC contain rare and poorly preserved specimens of *S. inornata*; the lowest occurrence of this species is directly above the K/Pg boundary (Willumsen, 2011; Taylor et al., 2018). A poorly preserved and pale specimen of *T. evittii* was tentatively identified in the lowermost sample (20R-CC). Supporting evidence that Site U1553 did not penetrate Late Cretaceous strata are the occurrence of abundant *P. pyrophorum*, which is rare in the latest Cretaceous (Willumsen, 2011), and an absence of any distinctive Late Cretaceous taxa (e.g., *Chatangiella campbellensis, Manumiella druggii, Xenikoon australis*). Peridinioid dinocysts are abundant in this lowermost interval.

4.7. Integrated stratigraphy

The zonation charts (Figures **F23**, **F24**) indicate good overall agreement in age control of Site U1553 for calcareous nannofossils, planktonic foraminifers, and radiolarians. An expanded Oligocene interval spans most of the upper 180 m of the sedimentary succession. Foraminifer biostratigraphy indicates that the early/late Oligocene boundary (28.1 Ma), which coincides with the base of Biozone AO3 (top of *Globigerina labiacrassata*), occurs at ~40 mbsf (40.8–50.4 mbsf in Hole U1553A; 53.8–58.7 mbsf in Hole U1553B; 26.8–36.7 mbsf in U1553E). This is consistent with correlation of this interval with the nannofossil *C. altus* zone, which spans the early–late Oligocene transition. Radiolarians suggest that the entire Oligocene succession is within the early Oligocene, but this is likely an artifact of difficulties with confident identification of *C. robusta*. The lowest occurrence of this species marks the base of Biozone zRP17 in the latest early Oligocene (28.2 Ma).

There is good agreement between all fossil groups for the E/O boundary (33.89 Ma), placing it at ~180 mbsf in Holes U1553A, U1553B, and U1553E (Figure **F26**). The boundary is bracketed by two nannofossil datums (the base of *C. altus* and the top of *R. oamaruensis*; 33.31 and 33.97 Ma, respectively), and it lies directly above the top of foraminifer Biozone AE8 (top of *G. index*; 34.6 Ma) and directly below the base of radiolarian Biozone zRP15 (base of *E. antiquum*; 33.5 Ma). These datums allow us to place the E/O boundary between 169.3 and 183.2 mbsf in Hole U1553A, between 182.9 and 187.2 mbsf in Hole U1553B, and between 160.7 and 167.8 mbsf in Hole U1553E.

The middle/late Eocene (Bartonian/Priabonian; 37.8 Ma) boundary was identified only in Hole U1553C (Figure **F24**). It is bracketed by two nannofossil datums (the top of *N. dubius* [36.70 Ma; 234.31–236.88 mbsf] and the top of *C. solitus* [38.34 Ma; 265.85–273.41 mbsf]). A location at ~255 mbsf is consistent with latest middle Eocene foraminiferal and radiolarian datums. The base of foraminiferal Zone AE8 (top of *A. primitiva*; 39.1 Ma) is identified at 265.8–277.74 mbsf, and the base of radiolarian Zone RP14 (base of *E. spinosum*; 38.15 Ma) is identified at 245.85–255.58 mbsf. The top of *A. primitiva* also defines the base of the New Zealand Kaiatan Stage (Raine et al. 2015). The early/middle Eocene boundary is also recorded only in Hole U1553C (Figure **F24**) and is provisionally placed at the base of nannofossil Zone NP14 (49.11 Ma), which is marked by the base of common *Discoaster sublodoensis* (5-rayed) at 374.40–383.33 mbsf. This location is consistent with foraminifer and radiolarian biostratigraphy, being within Biozone AE4 and Biozones zRP10 and zRP11, which span the early/middle Eocene boundary.

The Paleocene–Eocene transition was recovered in Holes U1553C and U1553D. The P/E boundary is well constrained by the top of the range of the benthic foraminifer species *G. beccariiformis*, which is one of the species known to go extinct at the P/E boundary. The datum is identified in Samples 378-U1553C-31R-CC and 378-U1553D-7R-CC and constrains the boundary to between 445.79 and 451.36 mbsf in Hole U1553C and between 447.8 and 453.5 mbsf in Hole U1553D. The precise location of the P/E boundary in this interval has yet to be determined, but a location within Core 378-U1553D-7R is supported by the lowest occurrence of planktonic foraminifer species *G. australiformis*, which marks the base of Biozone AE1, in Sample 6R-CC. The base of radiolarian species *A. prolixum*, which marks the base of earliest Eocene radiolarian Zone zRP8, also occurs in this sample, but in Hole U1553C the datum is higher in the hole (Sample 29R-CC). Similarly, the earliest Eocene calcareous nannofossil datum, the top of *F. tympaniformis* (base of Biozone CNE2), and the characteristic of the observed nannofossil assemblage help to constrain the P/E boundary within Section 378-U1553D-7R-2 and within the upper part of Core 378-U1553C-31R (between the base of Section 31R-1 and the base of Core 29R). A further complication is that the radiolarian assemblage in Sample 31R-CC consists of abundant poorly preserved spumellarians, which is a feature found in PETM intervals in New Zealand and Northwest Atlantic IODP Expedition 342 sites, suggesting an earliest Eocene age for this sample.

Given the shipboard biostratigraphy sample resolution, there is currently some uncertainty in the detailed early/late Paleocene stratigraphic succession in Hole U1553D regarding poor nannofossil assemblages. Other groups are too sparse in Hole U1553D and all groups are too sparse in Hole U1553C to evaluate this interval in more detail on board. Identification of early Paleocene radiolarians at ~480 mbsf in Holes U1553C and U1553D suggests that the K/Pg boundary may be near the base of the cored interval at Site U1553 (~580 mbsf) or possibly below the cored interval. Trace occurrences of early Paleocene nannofossils were noted to ~550 mbsf in Hole U1553C. Dinoflagellate cysts in core catcher samples from Paleocene Lithostratigraphic Unit V in Hole U1553D confirmed that the base of the cored interval is within the early Paleocene.

4.7.1. Correlation with New Zealand stages

The sedimentary sequence at Site U1553 can be correlated with New Zealand stages based on the following foraminifer and dinocyst datums:

- The top of *S. angiporoides* (base of Biozone AO2) = the base of the upper Whaingaroan–Duntroonian stage (29.8 Ma).
- The top of *G. index* (base of Biozone AO1) = the base of the lower Whaingaroan stage (34.6 Ma).
- The top of *A. primitiva* (base of Biozone AE8) = the base of the Kaiatan–Runangan stage (39.1 Ma).
- The base of *G. index* (base of Biozone AE6) = the base of the Bortonian stage (42.6 Ma).
- The top of *M. crater* = the base of the Porangan stage (45.7 Ma).
- The base of *M. crater* = the base of the Mangaorapan–Heretaungan stage (52 Ma).
- The top of *G. beccariiformis* = the base of the Waipawan stage (55.96 Ma).
- The base of *S. inornata* (Dinocyst Zone NZDP1) = the base of the Teurian stage (66.04 Ma).

5. Paleomagnetism

5.1. Shipboard measurements

Shipboard paleomagnetic studies of Site U1553 consisted of in-line alternating field (AF) demagnetization and measurement of archive-half sections using the pass-through 2G Enterprises superconducting rock magnetometer (SRM) as well as AF demagnetization of oriented discrete samples (see **Paleomagnetism** in the Expedition 378 methods chapter (Röhl et al., 2022) measured on the spinner magnetometer (AGICO JR-6A). Representative discrete samples (117 total) were collected approximately every other core section (~3 m) except for those sections that were severely disturbed or had special research interests, like critical boundaries.

In spite of good core recovery and the use of nonmagnetic core barrels (on APC, HLAPC, and RCB cores) and the Icefield MI-5 core orientation tool (Holes U1553A and U1553B; APC cores), because of carbonate-rich lithologies (see **Lithostratigraphy** and **Demagnetization behavior**) with less magnetic carriers, the sediment magnetization was not strong (10^{-8} A/m^2 to 10^{-9} A/m^2) and was close to the background noise and drift level (10^{-9} A/m^2) after low AF treatments (3 and/or 6 mT). Additional AF treatments were not considered so as not to further demagnetize the cores, allowing more detailed treatments and measurements in home laboratories. Thus, only low-temperature thermal treatments (up to 175°C) and low-field AF treatments were employed shipboard. Most of the discrete samples were measured using AF treatments, and four were selected from different lithologies (nannofossil ooze, nannofossil chalk, limestone, and muddy sandstone/mudstone, respectively; see **Lithostratigraphy** for detailed rock unit descriptions) and underwent stepwise thermal treatments (100°, 125°, 150°, and 175°C) (see **Demagnetization behavior**).

Ten magnetic reversals were determined based on the paleomagnetic data of the upper ~125 m of Hole U1553A (see **Magnetostratigraphy**). The rest turned out to be very challenging for a reliable magnetostratigraphic reconstruction, most likely because of the very low abundance of magnetic carriers in carbonate-rich sediment.

Anisotropy of magnetic susceptibility (AMS) of all discrete samples, except those that were too broken or crumbly to fit the instrument, was also measured. The results imply a possible change in the bottom water dynamic at ~440 mbsf, above which bottom water velocity increased (see **Anisotropy of magnetic susceptibility**).

5.2. Demagnetization behavior

The recovered Site U1553 sediments are mostly composed of nannofossil ooze/chalk or limestone in Lithostratigraphic Units I–IV (0 to ~475 mbsf) (see **Lithostratigraphy**), and magnetic minerals such as magnetite are not abundant. This results in a weak natural remanent magnetization. Muddy sandstone/mudstone is the primary lithology below ~475 mbsf in Holes U1553C and U1553D (Lithostratigraphic Unit V), and this unit contains relatively more magnetite than the carbonate-rich sediments above. Except for Unit I, the lithostratigraphic units are characterized by demagnetization measurements indistinguishable from the background level and likely only represent noise. Consequently, polarity interpretation and magnetostratigraphy construction are challenging. This is probably due to the overall lack of magnetic carriers and, to some degree, diagenetic processes such as dissolution of magnetite to form glauconite and/or pyrite/greigite, as suggested by Ohneiser and Tapia (2020) for DSDP Site 277 sediments.

Variations in magnetic remanence with depth can reflect changes in lithology or drilling disturbance. For example, the higher values of magnetic intensity recorded at ~129 mbsf in Section 378-U1553B-15X-3 correlate with an ash layer (Figure **F30**). The ~9.5 cm cyclicity in the magnetic intensity data is actually an artifact from drilling disturbance (mechanical force, as discussed in Yang et al., 2019). In addition, higher magnetic intensity values for the first section of each core are often caused by soupy intervals from drilling disturbance that possibly contain fall-in pyrite nodules (see **Lithostratigraphy**). The drilling-induced remanence was removed in most core sections by AF treatment of 3–6 mT (Figure **F31D**).

The intensity of the field strength of in-line AF demagnetization was limited because of our limited ability to measure weak magnetizations in the nonmagnetically shielded shipboard environment and the destructive nature of such treatments preventing high-quality measurements in our home laboratories. Typical examples of normal and reversed polarity interpretations of Hole U1553A archive-half section data are illustrated in Figure **F31A–F31D**. The modern geocentric axial dipole (GAD) inclination at Site U1553 is about 68.8°, calculated using PmagPy software (Tauxe et al., 2016) (dashed blue lines in the inclination column in Figures **F32**, **F33**, **F34**, **F35**, **F36**, and **F37**). The Eocene GAD inclination of this location, which was farther south according to paleogeography reconstructions (e.g., Torsvik et al., 2012), is about 70° as proven in DSDP Site 277 records (Ohneiser and Tapia, 2020). Although we do not have enough data to quantitatively solve

characteristic remanent magnetization (ChRM), the demagnetization paths and/or trends of low AF treatment steps (6–9 mT) were usually sufficient to estimate a normal or reversed polarity from the inclinations. For example, the measurement point in Section 378-U1553A-5H-1, 85 cm (57.15 mbsf), is interpreted to be reversed because the demagnetization first removes a drilling-induced steep-down component (inclination = 86°) at 3 mT and then removes the present-day overprint at 6 mT to reveal the Eocene component (Figure **F31D**). Only the last step, 12 mT, seems to reach the expected ChRM before the magnetization gets too close to background noise and drift level. Data resulting from measurements on section halves at measurement points in Sections 378-U1553A-2H-6, 60 cm (11.12 mbsf), and 378-U1553A-7H-5, 65 cm (32.35 mbsf) (Figure **F31B–F31C**), are classified as representing good reversed polarity, gradually removing overprints and trending toward the origin. The ChRM inclinations are a bit shallower compared to the Eocene GAD inclination, likely due to sediment compaction and consequent inclination flattening (e.g., Tauxe, 2005). The measurement from Section 378-U1553A-2H-3, 25 cm (6.26 mbsf) (Figure **F31A**), likely records a robust normal polarity because no reversal trend was observed during the demagnetization.

The typical magnetic behaviors of discrete samples from Holes U1553A and U1553C are shown in Figure **F38**. Regarding AF treatments, most samples show an initial increase in intensity at 3–6 mT followed by a gradual decrease before increasing again at 20–40 mT (at 8 mT in Sample 378-U1553A-10H-2, 46–48 cm) (Figure **F38D**), trending away from the origin on the orthogonal vector plot. We suspect that the initial intensity increase is caused by removing an opposite-directed drilling-induced magnetization component similar to the archive-half analyses. The second increase suggests a higher coercivity magnetic mineral composition that could not be demagnetized using low AF treatments, a result associated with the presence of greigite (e.g., Rowan and Roberts, 2006). Further shore-based AF/thermal demagnetization tests will refine our understanding of these properties. Sample 378-U1553C-43R-6, 57–59 cm (Figure **F38E**), did not exhibit an intensity increase but instead gradually trended toward the origin. The ChRM inclination is calculated to be −72°, which is slightly steeper than the estimated Eocene GAD inclination. Regarding thermal treatments (Figure **F38F**), an intensity drop of 50% is often observed at 100°C and followed by an increase at 150°C while trending away from the origin. This is probably caused by the formation of magnetite by the oxidation of pyrite/greigite.

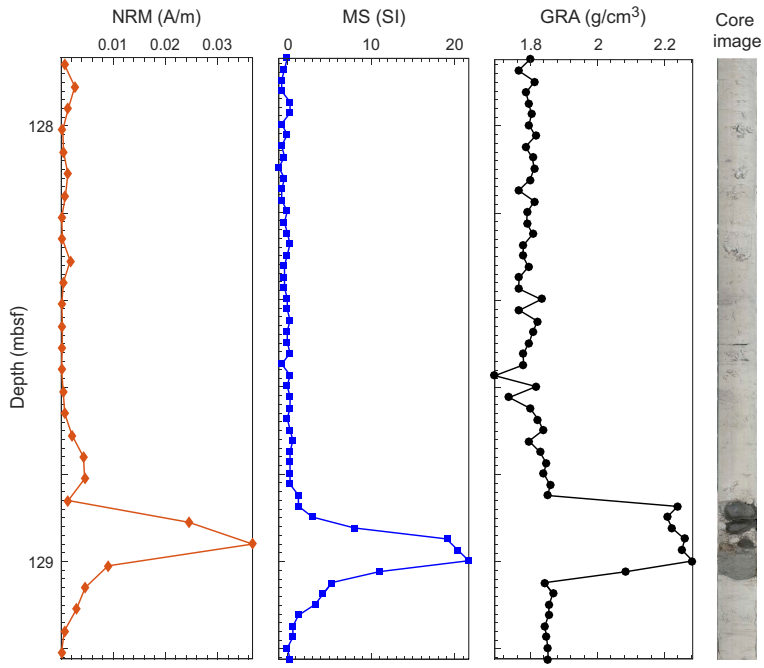

Figure F30. Magnetic intensity of natural remanent magnetization (NRM), magnetic susceptibility (MS), and gamma ray attenuation (GRA) data, Section 378-U1553B-15X-3. All point measurements were made on archive halves.

According to preliminary shipboard observations, glauconite is present in the pale green layers of the pale chalk unit (Lithostratigraphic Unit III) and the presence of pyrites and cherts/flints increases with depth below seafloor (see **Lithostratigraphy** and **Geochemistry**). The abundance of glauconite has been reported in marine sediments in New Zealand land sections (e.g., Lurcock and Wilson, 2013), which could dilute the amount of magnetite and weaken the overall remanence magnetization. Pyrite/greigite is often associated with the dissolution of magnetite through sulfate reduction, which complicates the demagnetization behaviors (e.g., Roberts, 2015; Roberts et al., 2013; Rowan and Roberts, 2006). Postcruise research efforts will be required to better understand why the sediments are weakly magnetized with poor demagnetization behaviors.

5.3. Magnetostratigraphy

Declinations of the APC cores from Holes U1553A and U1553B were corrected using the Icefield MI-5 core orientation tool. However, the corrected declinations did not help resolve magnetic polarity, probably because of the extremely weak remanence magnetization, and therefore were not used. Based on inclinations at 6 mT and the demagnetization paths of specimens from archive halves, we constructed a preliminary magnetostratigraphy of the upper ~125 m of Hole U1553A (Figure **F32**). Below ~125 mbsf, no polarity interpretation was attempted. Data from Holes U1553B and U1553E seem to indicate strong overprints and are not as clear as those from Hole

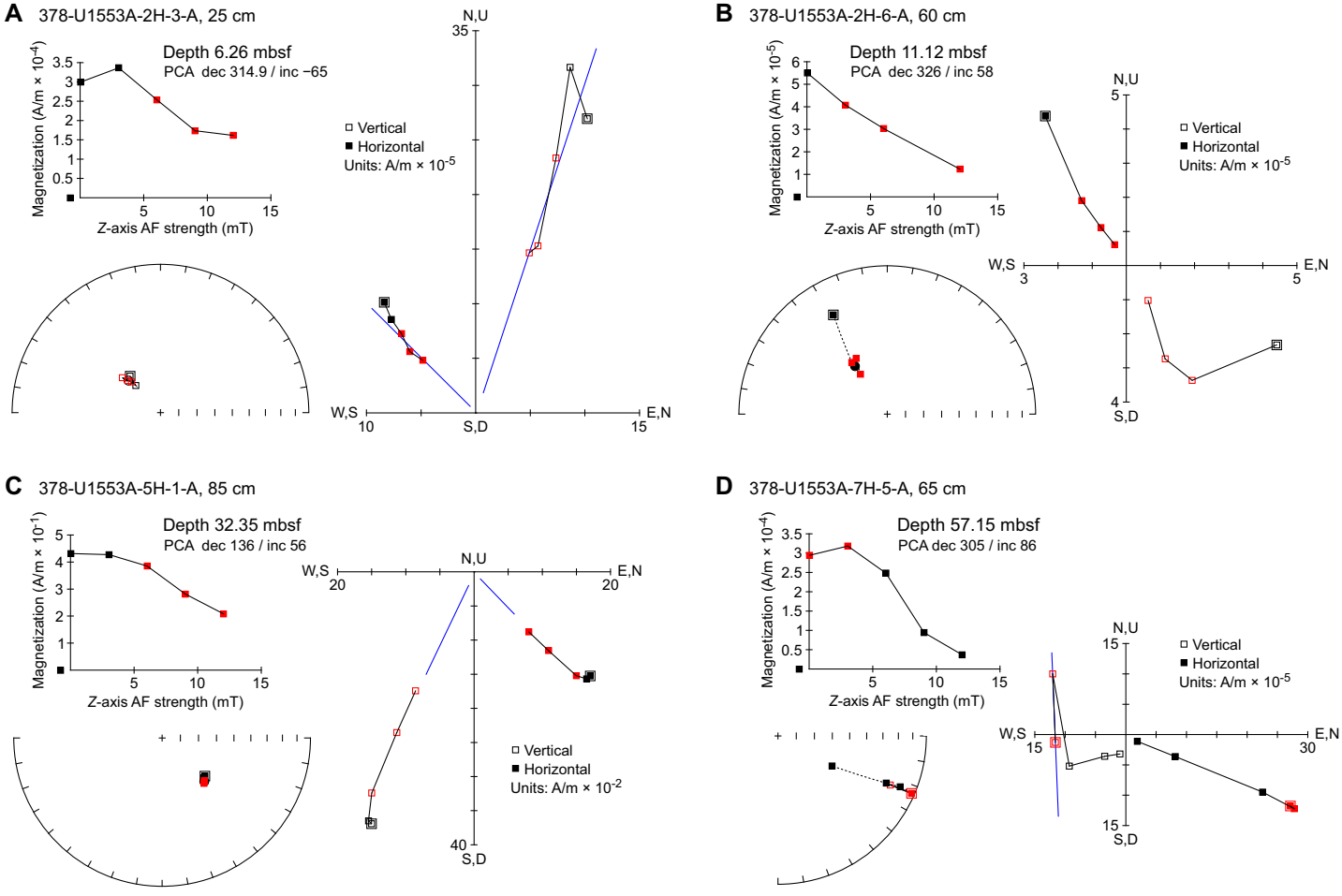

Figure F31. Demagnetization plots of archive halves, Hole U1553A. Calculated ChRM (blue line and red squares = measurements used in calculation) (A) using principal component analysis (PCA), (B) showing reversed polarity, and (C, D) showing normal polarity and the drilling induced magnetization removed at 3 mT. Declination and inclination of remanent magnetization at progressive demagnetization steps are displayed on both stereographic projection and Zijderveld diagrams (Zijderveld, 1967). Intensity of remanent magnetization is plotted against the treatment value. On Zijderveld diagrams, solid symbols represent declination and open symbols represent inclination. On stereographic plots, solid symbols indicate positive (down-pointing) inclination and open symbols indicate negative (up-pointing) inclination. AF = alternating field.

U1553A. Therefore, only the raw data for Holes U1553B and U1553E are shown in Figures **F33** and **F34**.

This ~125 m preliminary magnetostratigraphy of Hole U1553A is composed of five pairs of normal and reverse polarity patterns (n1/r1 to n5/r5 downsection). Core 378-U1553A-1H is Pleistocene in age and lies unconformably above Core 2H, which is Oligocene in age, based on shipboard microfossil ages (see **Biostratigraphy and micropaleontology**). This boundary approximately aligns with the base of r1. Comparison to the 2012 geologic timescale (GTS2012) (Gradstein et al., 2012) suggests that n1 and r1 correlate to the Brunhes and Matuyama polarity chrons, respectively. We thus propose that the unconformity should be placed at the base of r1 in Sections 378-U1553A-2H-1, 40 cm (3.4 mbsf), 378-U1553B-1H-4, 8 cm (4.6 mbsf), and 378-U1553E-1H-3, 19

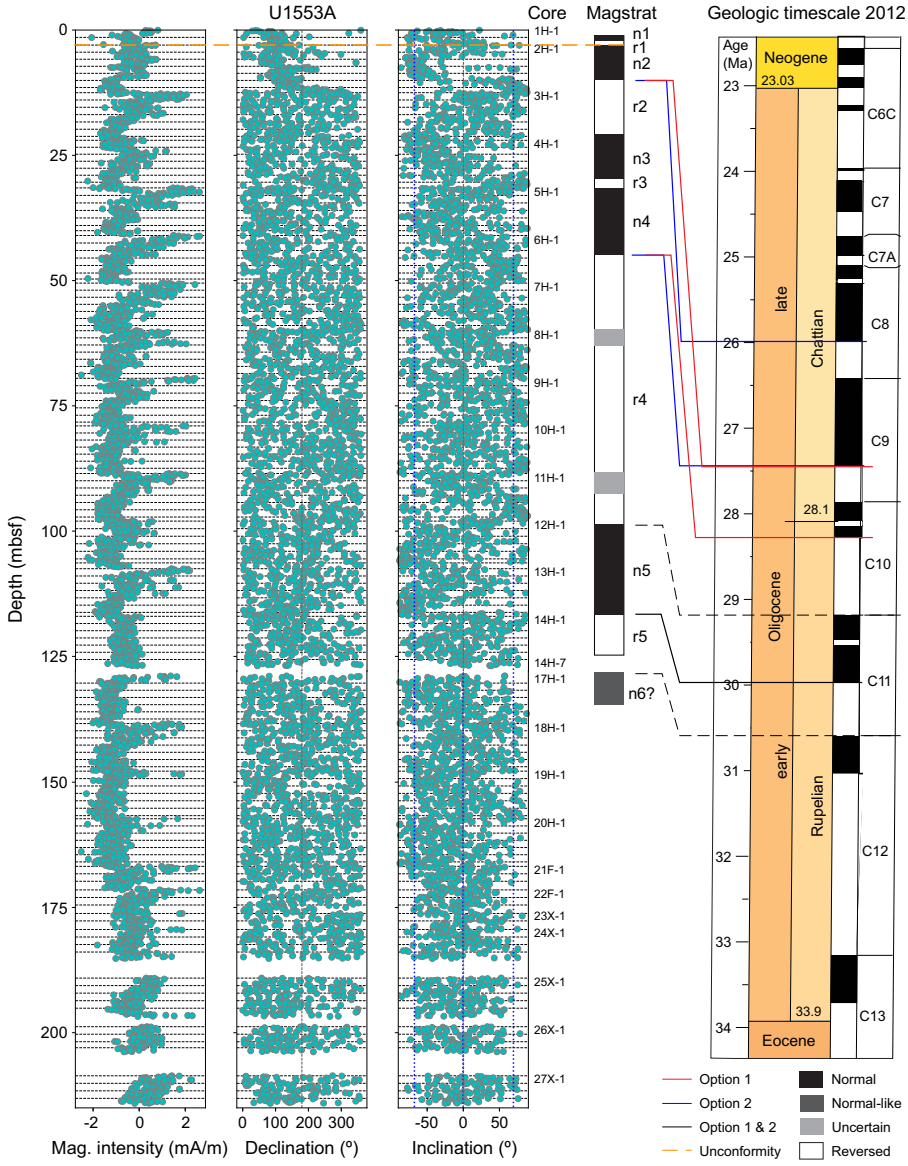

Figure F32. Magnetic measurements, Hole U1553A. Magnetic reversals were identified based on inclinations. Two options are provided (solid correlation lines in red and blue, respectively) for polarity Patterns n2/r2, n3/r3, and n4/r4. Correlation solid/dashed lines in black are the same for both options. Dashed blue line in the inclination column denotes the modern geocentric axial dipole inclination of Site U1553 (68.8°). Dashed orange line at the base of polarity pattern r1 is likely a major unconformity separating the overlying Pleistocene and the underlying Oligocene successions. Dashed black lines mark the separations of core sections, with the first core section noted, and when a core recovery gap exists the last section is also shown. Data from Cores 15H and 16X are not shown because of severe drilling disturbance (e.g., hitting a hard sandy layer in Core 16X [see Lithostratigraphy]). Magstrat = magnetostratigraphy.

cm (3.2 mbsf) (Figure **F35**). Because the ~125 m magnetostratigraphy of Hole U1553A is normal-polarity dominated, we correlate it with the middle–late Oligocene geomagnetic polarity timescale of GTS2012 (Figure **F32**) (Gradstein et al., 2012). The position of each reversal is listed in Table **T9**. Two options are provided here regarding the polarity reversals n2/r2, n3/r3, and n4/r4. Option 1 (red solid lines in Figure **F32**) correlates the base of n4 with the base of C10n.2n, the base of r2 with the base of C9r, and the base of n2 with the base of C9n of GTS2012 (Gradstein et al., 2012). This option results in an average sediment depositional rate of ~4 cm/ky for the upper ~100 m. Option 2 (blue solid lines in Figure **F32**) instead correlates the base of n4 with the base of C9n, the base r2 with the base of C8r, and the base of n2 with the base of C8n. This option results in a slower sediment depositional rate of ~2.5 cm/ky. When compared to the shipboard biostratigraphic age model, Option 1 appears to be more consistent, although further shore-based work is required to verify both paleomagnetic and biostratigraphic age models.

The recovery gaps in Holes U1553C and U1553D make it more challenging to build a polarity pattern and to correlate with the standard geomagnetic timescale. Further work will be conducted postcruise with the goal to better establish a magnetostratigraphy below ~125 mbsf. However, two reversals were identified in Hole U1553C: at ~290 mbsf between the recovery gap of Cores 8R and

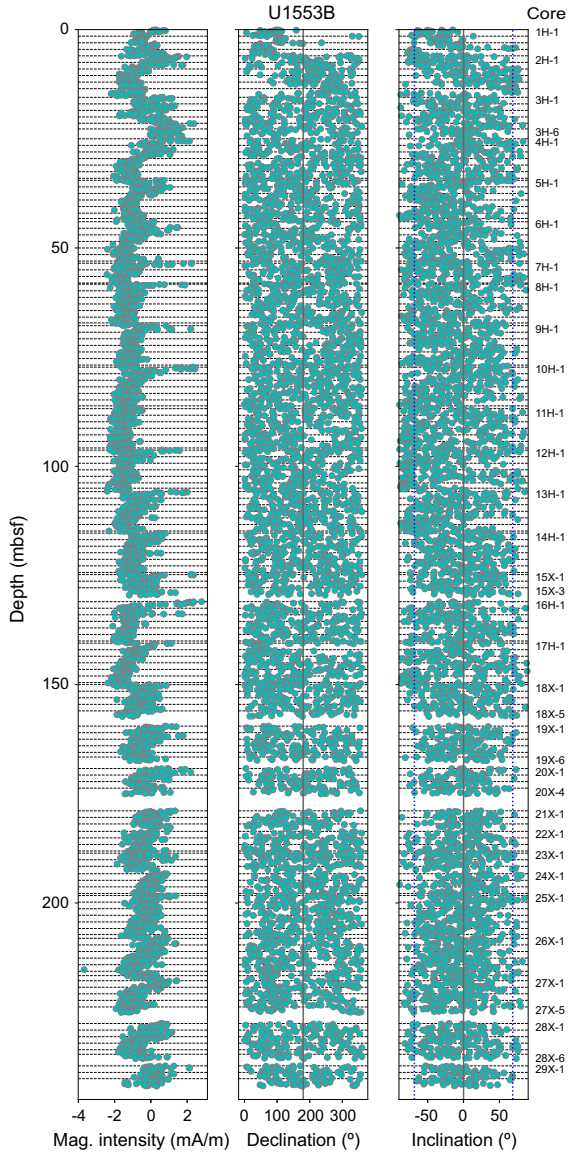

Figure F33. Paleomagnetic data at an alternating field of 6 mT, Hole U1553B.

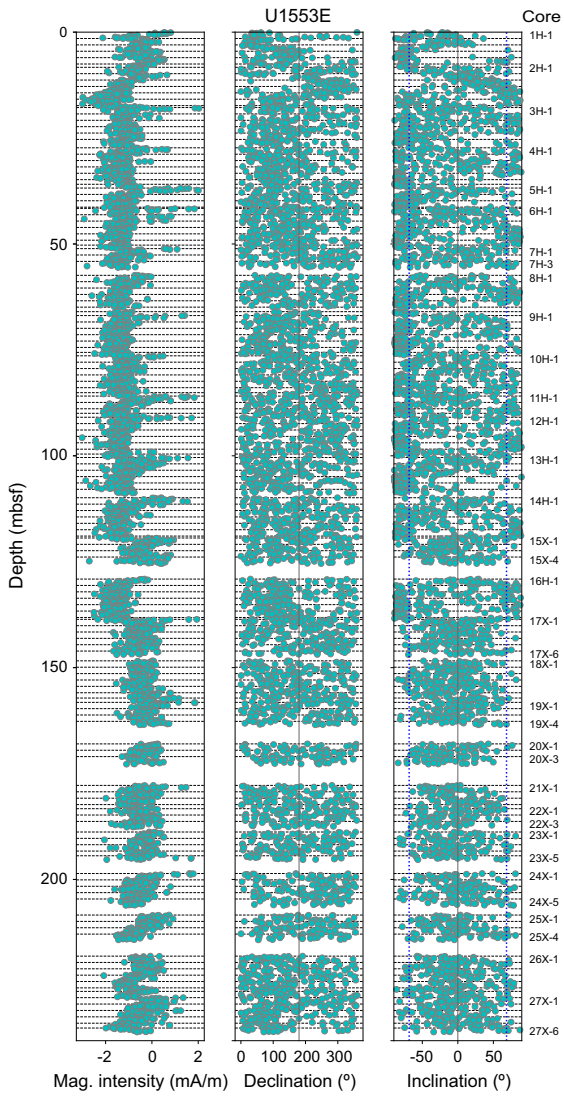

Figure F34. Paleomagnetic data at an alternating field of 6 mT, Hole U1553E.

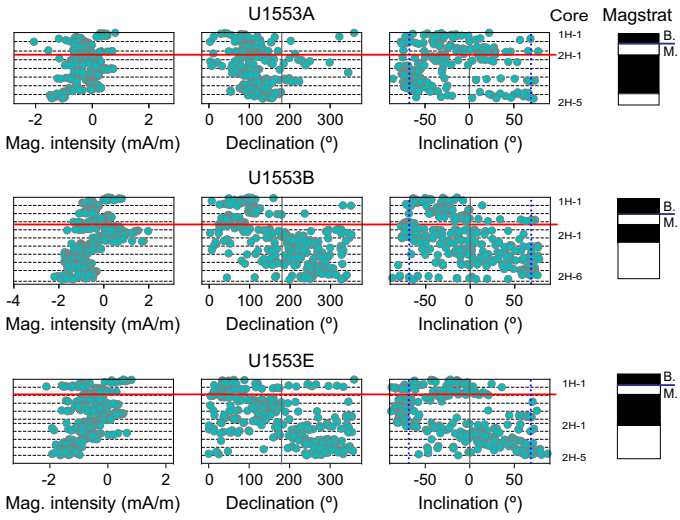

Figure F35. Paleomagnetic data at an alternating field of 6 mT from the uppermost two cores, Holes U1553A, U1553B, and U1553E. B. = Brunhes Chron, M. = Matuyama Chron, Magstrat = magnetostratigraphy. Red lines = unconformity levels of each hole based on magnetic reversals.

9R and at 442.8 mbsf in Section 29R-4, 7 cm (n7/r7 and n8/r8 in Figure **F36**). The deepest reversal observed in Hole U1553C may also be present in Hole U1553D in Section 6R-2, 24 cm (440 mbsf) (Figure **F37**). Given that these successions are Paleocene to Eocene in age, we attempted to correlate the first reversal (n7/r7) with the base of Chron C18n.2n and the second reversal (n8/r8) with the base of Chron C24n.3n, which agrees with the shipboard biostratigraphic age model (see **Biostratigraphy and micropaleontology** and **Age-depth model and mass accumulation rates**). However, these two reversals need further verification, as noted in Table **T9**.

5.4. Anisotropy of magnetic susceptibility

We measured the AMS of all discrete samples except those that were too broken or crumbly to fit into the Agico KLY 4S Kappabridge instrument. The AMS fabric is described by a symmetrical second rank tensor (Hrouda, 1982), which can be described by a triaxial ellipsoid with the principal eigenvectors $K_{max} > K_{int} > K_{min}$ representing the maximum, intermediate, and minimum susceptibility axes, respectively (Figure **F39B**). These eigenvectors could reflect the depositional plane of sediments (e.g., Lowrie and Hirt, 1987) and are associated with bottom water dynamic conditions. Usually, the K_{max} axis aligns parallel with water currents, and the tilting direction of the K_{min} axis

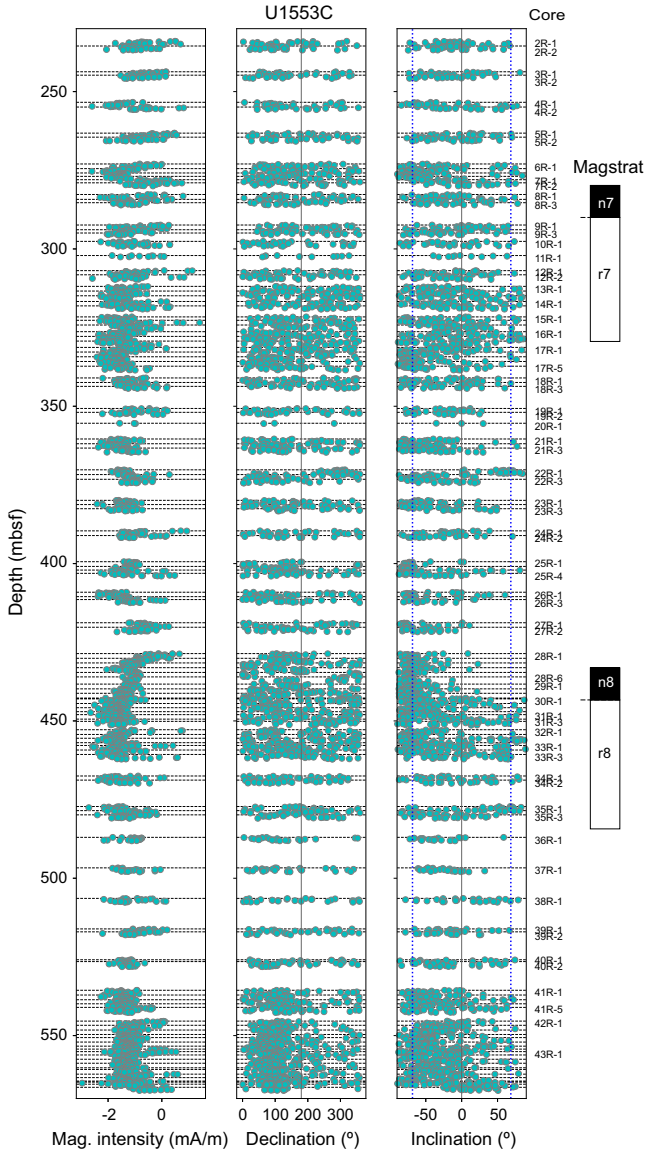

Figure F36. Paleomagnetic data at an alternating field of 6 mT, Hole U1553C. The two magnetic reversals observed (n7/r7 and n8/r8) and their potential correlations to the 2012 geologic timescale are shown. Magstrat = magnetostratigraphy.

can be used to infer the absolute water current direction (e.g., Piper et al., 1996; Liu et al., 2001). The AMS data (Figure **F39A**) clearly show a transition from steep K_{min} inclinations to much shallower and wildly distributed patterns around Section 378-U1553C-29R-2, 19 cm (~440 mbsf). This is also illustrated in the equal-area projection plots (Figure **F39D**), which show a change in K_{min} distributions from semiclustering in the steep area to scattering around the entire area. We interpreted this AMS orientation change as reflecting an increase in bottom water velocity from a low–moderate velocity below ~440 mbsf to a relatively faster velocity above (Figure **F39C**).

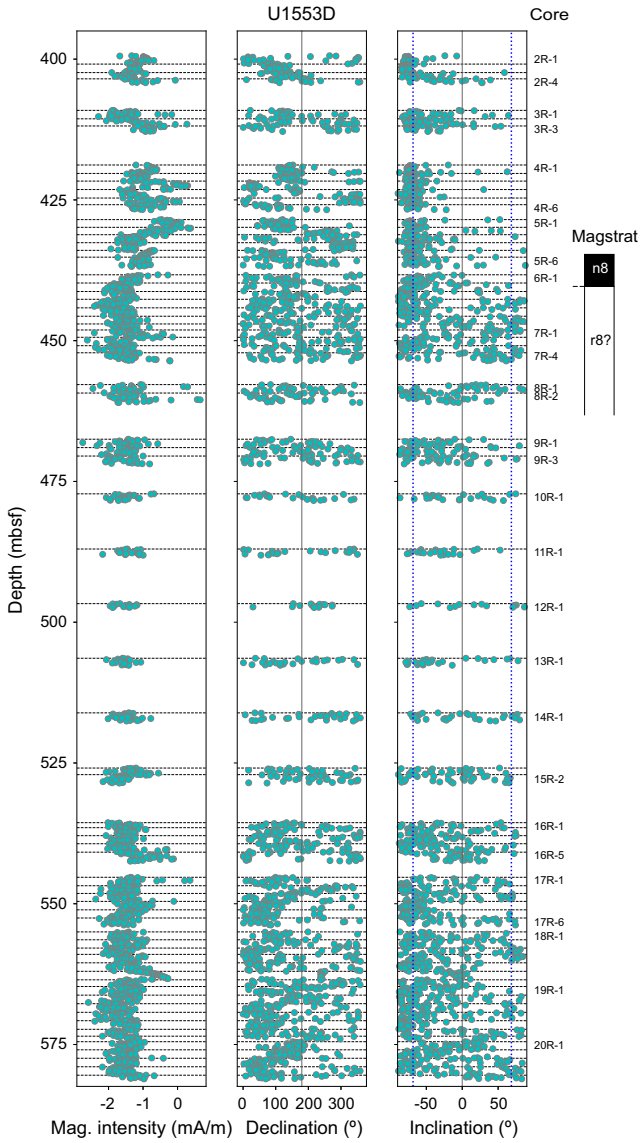

Figure F37. Paleomagnetic data at an alternating field of 6 mT, Hole U1553D. The marked magnetic reversal correlates to the second reversal (n8/r8) in Hole U1553C. AF = alternating field, Magstrat = magnetostratigraphy.

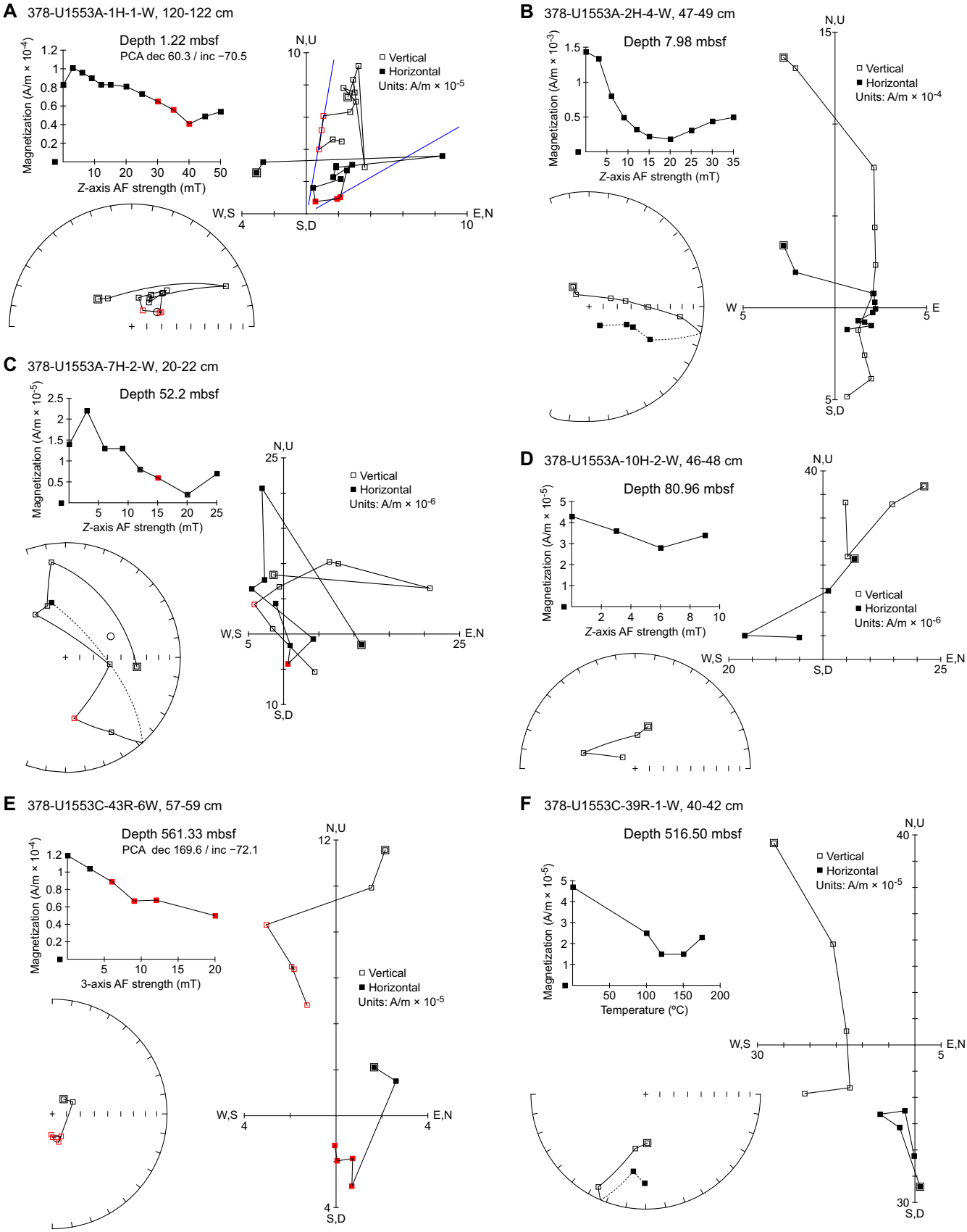

Figure F38. Demagnetization plots of discrete samples, Holes U1553A and U1553C. See Figure F31 for symbol definitions. PCA = principal component analysis. AF = alternating field.

Table T9. Shipboard paleomagnetic age model, Expedition 378. Two options are provided for polarity reversals n2/r2, n3/r4, and n4/r4. Base of r5 and n6? are not very well defined, so no base depth is listed. Magnetic chrons and base ages according to the GTS2012. In Option 2, C10n is not identified in Hole U1553A. * = depths have large uncertainties. **Download table in CSV format.**

Reversals identified in U1553A	Base depth (mbsf)	Core, section, interval (cm)	Option 1 Chron	Base age (Ma)	Option 2 Chron	Base age (Ma)
		378-U1553A-				
n1	2.2	1H-2, 70	C1n (Brunhes)	0.78		
r1	3.4	2H-1, 40	Matuyama			
n2	9.5	2H-5, 49	C9n	27.439	C8n	26
r2	21.4	3H-7, 138	C9r	27.859	C8r	26.42
n3	29.9	4H-6, 40				
r3	33.3	5H-2, 30				
n4	45	6H-3, 100	C10n.2n	28.278	C9n	27.439
r4	88.6	10H-7, 61	C10r	29.183	C10r (C10n not identified)	
n5	117.2	13H-CC, 14	C11n.2n	29.97	C11n.2n	
r5	~127					
n6?						
		378-U1553C-				
n7	290*	Gap between 8R and 9R	C18n.2n	40.073		
r7	329.9*	16R-3, 61	C18r			
n8	442.8*	29R-4, 7, or U1553D-6R-2, 24	C24n.3n	53.983		
r8	483*	Gap between 35R and 36R	C24r			

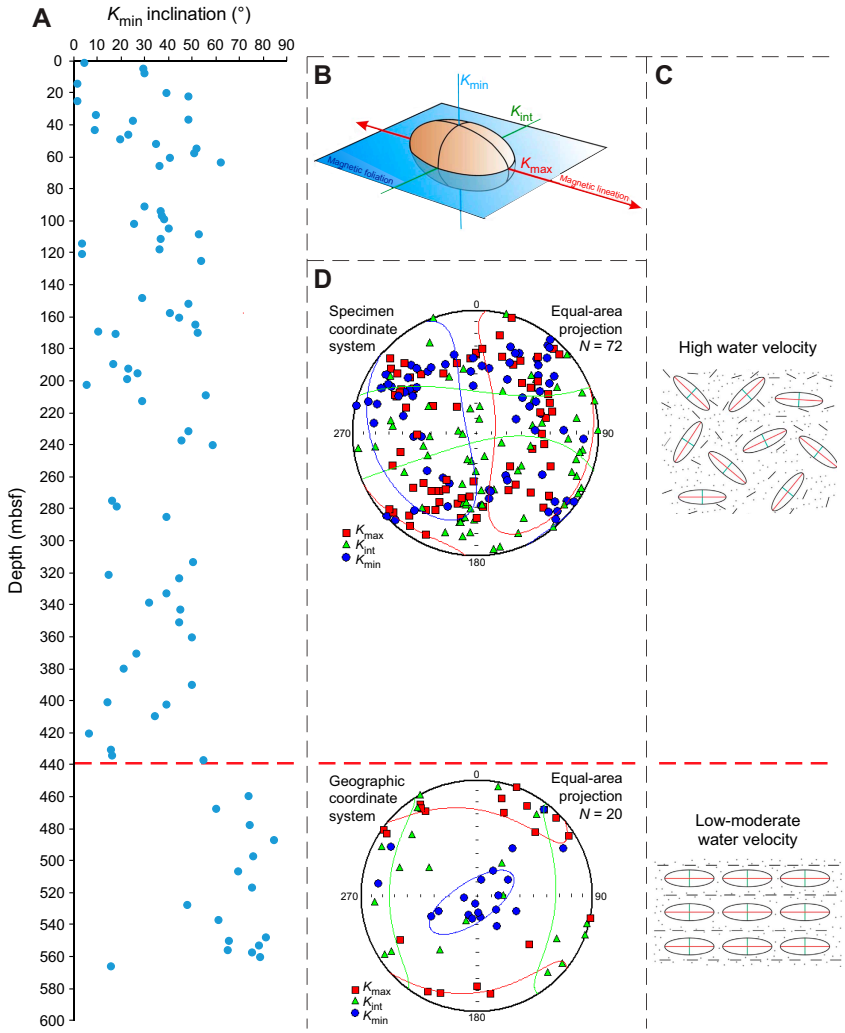

Figure F39. Anisotropy of magnetic susceptibility (AMS), Site 1553. A. AMS of all discrete samples collected on board. B. Ellipsoid of AMS axes. C. The equal area projection of all the inclinations of K_{max}, K_{int}, and K_{min} ovals represents the 95% confidence ellipses of each *K* direction. Dashed red line = depth of transition from low–moderate water velocity to high water velocity. D. Ellipsoids of magnetic minerals within sedimentary beds. B and D are adapted from Yang et al. (2019).

6. Geochemistry

The geochemical composition of the sediment and water samples from Site U1553 reflects the lithostratigraphic descriptions of the sediment (see **Lithostratigraphy**). The presence of abundant calcite and occasional glauconite, manganese nodules, pyrite, and chert suggests possible subseafloor changes in the aluminosilicates and siliceous and carbonaceous components of the sediment. At Site U1553, sufficiently resolved interstitial water (IW) profiles and solid-phase analyses were obtained to characterize the diagenetic impact on the sedimentary record that may affect paleoceanographic proxies.

6.1. Headspace gas monitoring

For the uppermost 480 m of Site U1553 (above Sample 378-U1553C-35R-2, 133–134 cm), methane is close to the 1:1 signal-to-noise ratio and ethane, propane, butane, and other heavier hydrocarbons are below the detection limit, suggesting a lack of biogenic and/or thermogenic gas production or their upward migration. A sudden increase in methane concentration occurs at 490 mbsf (Figure **F40**; Table **T10**), coincident with a strong hydrocarbon gas smell and a drastic change from white to gray core material that corresponds to the transition from Lithostratigraphic Unit IV to Unit V (see **Lithostratigraphy**). The methane increase is accompanied by the detection of thermogenic hydrocarbons (C_2, C_3, and C_4) beginning at 542 mbsf, suggesting in situ methane production, possibly by microbial activity, and thermogenic gas upward migration. The low porosity of the core material at the top of Unit V (see **Physical properties**) may have acted as a physical barrier for upward gas migration. Hydrocarbons reach a local maximum at ~555 mbsf (Sample 378-U1553C-42R-8, 149–150 cm), where methane values reached 5180 ppmv. Gradually decreasing C_1/C_2 ratios with depth led to the termination of drilling operations in Hole U1553C at 568 mbsf (Table **T10**). Reevaluation of the chromatographic response with known standards determined an underestimation of methane concentrations of 15% and a subsequent underestimation of C_1/C_2 ratios. Recalculation of C_1/C_2 ratios and an additional temperature measurement (15.63°C) at 181 mbsf in Hole U1553D provided a better constraint for the deeper drilling in Hole U1553D (Figure **F41**).

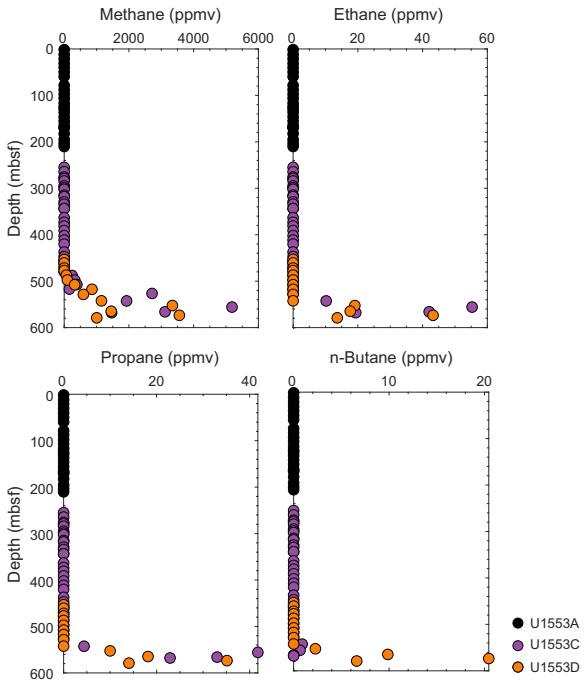

Figure F40. Hydrocarbon gas concentrations, Site U1553. ppmv = parts per million by volume.

Table T10. Hydrocarbon gases concentrations, Site U1553. **Download table in CSV format.**

6.2. Interstitial water results

For analysis of water chemistry, 77 IW samples were taken from whole-round squeezing of sediment intervals in Holes U1553A, U1553B, and U1553C (61, 3, and 13 samples, respectively). Additional samples collected included one mudline sample (Section 378-U1553A-1H-1) and one core liner water sample (Section 378-U1553B-23X-5), which were filtered with Rhizon samplers. In Hole U1553B, 99 Rhizon samples were taken for additional IW analyses. Ion chromatography (IC) was used to measure major ions, and inductively coupled plasma–atomic emission spectrometry (ICP-AES) was used to analyze samples for major and trace elements. All IC and ICP-AES measurements were converted to molar concentrations using both in-house standards and the International Association for the Physical Sciences of the Oceans (IAPSO) seawater. Ammonia and phosphate concentrations were determined with spectrophotometry, and salinity was estimated with the refractometer. For XCB cores, some Rhizon sample data suggest that water carried into the core liner through drilling disturbance was sampled, rather than in situ pore fluids.

6.2.1. Alkalinity and pH

Total alkalinity increases from 2.5 mM at the seafloor to 3.6 mM at ~200 mbsf (Sections 378-U1553A-23X-1 through 27X-1). Alkalinity continues to increase with depth in Holes U1553B and U1553C. The rate of increase is highest in the upper 5 m and below 120 mbsf, likely as a result of carbonate dissolution. pH mirrors the alkalinity trend and increases from 7.6 to ~7.8. The highest pH is found between 130 and 170 mbsf, most likely due to dissolution of carbonates (Figure **F42**).

6.2.2. Ammonium and phosphate

Despite the overall low organic carbon content, ammonium increases from ~20 µM at the seafloor to 650–700 µM below 390 mbsf (Sections 378-U1553C-23R-1 through 27R-1) (Figure **F42**), suggesting either a contribution of ammonium from organic matter degradation or from mixing with a deeper, potentially microbial, source. Precision for ammonia standards varied from 13% for ≤200 µM concentrations to 2% for higher concentrations up to 1000 µM. Phosphate is less than 5 µM at the seafloor and reaches a maximum value of ~9 µM at 40 mbsf (Sample 378-U1553A-5H-6, 99–104 cm) (Figure **F42**), most likely as the result of degradation of organic matter. Deeper than 80 mbsf, phosphate concentrations decrease, some below the precision level (3 µM), and are there-

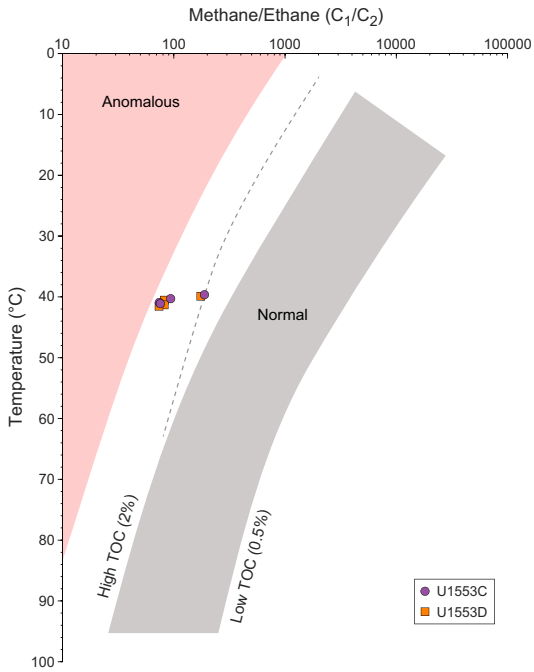

Figure F41. Methane/ethane (C_1/C_2) ratios, Site U1553. Plotted on the reference diagram for normal and anomalous regions of C_1/C_2 ratio vs. sediment temperature by Pimmel and Claypool (2001). C_1/C_2 ratios for Hole U1553C are corrected for a 15% overestimation of methane. TOC = total organic carbon. Modified from Pimmel and Claypool (2001).

fore unreliable. Rhizon sampling resulted in a noisy phosphate profile for Hole U1553B and thus was not used further.

6.2.3. Calcium, strontium, and barium

Calcium concentrations in the IW samples increase from 10.4 mM at the mudline (similar to the average seawater concentration) to ~13.5 mM at 200 mbsf in Holes U1553A–U1553C. The rate of increase changes slightly at ~100 mbsf (Figure **F43**). From 200 to 400 mbsf, the concentration of Ca remains constant between 12.5 and 14 mM. The trend is reflected in both the squeezed samples and the Rhizon samples, and it is reproduced by both inductively coupled plasma spectroscopy and IC analyses. Sr concentrations increase from 89.6 µM at the mudline to ~200 µM at 124 mbsf (Sample 378-U1553A-14H-5, 145–150 cm). Between 129 and 132 mbsf, concentrations abruptly increase from ~200 to ~234 µM. Deeper than 136 mbsf, Sr concentrations continue to increase and average 470 µM at 334–420 mbsf (Sections 378-U1553C-17R-2 through 27R-1). Carbonate dissolution could explain the increase in calcium and strontium with depth. The abrupt change in Ca and likely also in Sr from 124 to 136 mbsf corresponds to a sandstone layer encountered in all holes. This step change in the IW Ca and Sr profile may also represent a coring disturbance or poor recovery near a hard layer of sediment. Ba concentrations derived from squeezed samples are noisier than the trends observed in the Rhizon samples. This is considered an artifact related to the squeeze process, and many of the squeezed samples at or near the detection limit (all

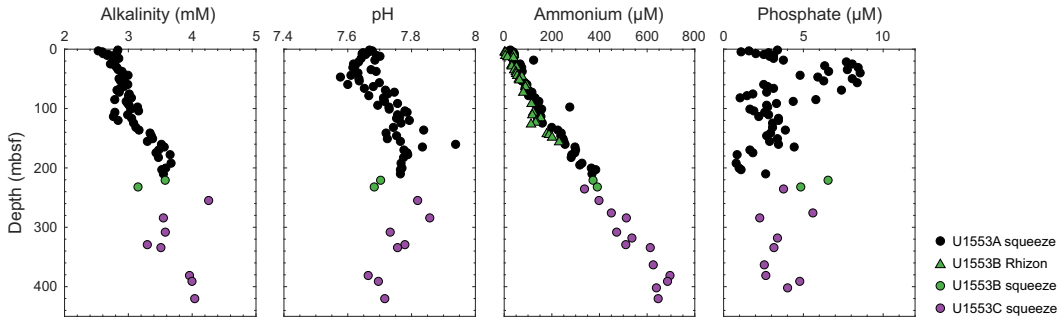

Figure F42. Pore water total alkalinity, pH, ammonium, and phosphate concentrations, Site U1553.

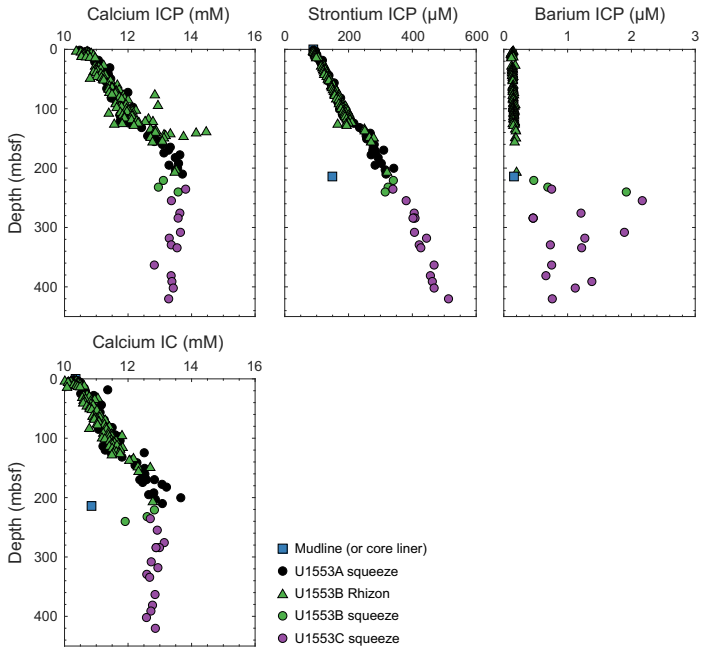

Figure F43. Pore water calcium, strontium, and barium concentrations, Site U1553. ICP = inductively coupled plasma–atomic emission spectrometry, IC = ion chromatography.

Hole U1553A samples) were discarded. The uppermost 160 m of Site U1553 are characterized by <0.2 µM Ba concentrations. Below 200 mbsf, Ba concentrations increase to 2.5 µM. Although these Ba concentrations are still very low, the trends in the profile possibly suggest low amounts of sulfate reduction that dissolves barite ($BaSO_4$), releasing Ba into the IW.

6.2.4. Magnesium, potassium, lithium, silicon, and boron

Dissolved Mg concentrations are 53 mM in the mudline water sample and decrease to ~33 mM at 420 mbsf (Sample 378-U1553C-27R-1, 138–143 cm) (Figure **F44**), possibly due to uptake into recrystallizing carbonates or authigenic clays forming within the seafloor. Alternatively, there may be a sink of Mg deeper in the sediment (e.g., dolomite), and the Mg profile reflects diffusion between seawater and the hypothesized deeper sink. K concentrations decrease downcore from 10.5 mM at the mudline to ~6 mM at 420 mbsf, reflecting alteration and uptake into clays formed within the seafloor (e.g., glauconite). Li concentrations are ~28 µM at the mudline and decrease to ~18 µM around 170 mbsf in Holes U1553A and U1553B. Below 170 mbsf, Li concentrations increase to ~34 µM at 420 mbsf. Si concentrations at the mudline are 55 µM but increase progressively to ~800 µM at 100 mbsf (Holes U1553A and U1553B). From 100 to 128 mbsf, Si concentrations decrease to ~580 µM. Si concentrations increase to 1030 µM, the maximum value measured at this site, at 170 mbsf. Below 170 mbsf, Si concentrations decrease and remain between 490 and 620 µM from 232 to 400 mbsf. The concave shape of the Si profile would suggest that Si is being supplied to the pore waters from the seafloor to 170 mbsf, except near 128 mbsf where there is a net removal of Si from the pore waters. Si concentrations deeper than 232 mbsf do not vary, perhaps because of the more lithified nature of the sediment. B concentrations increase from ~417

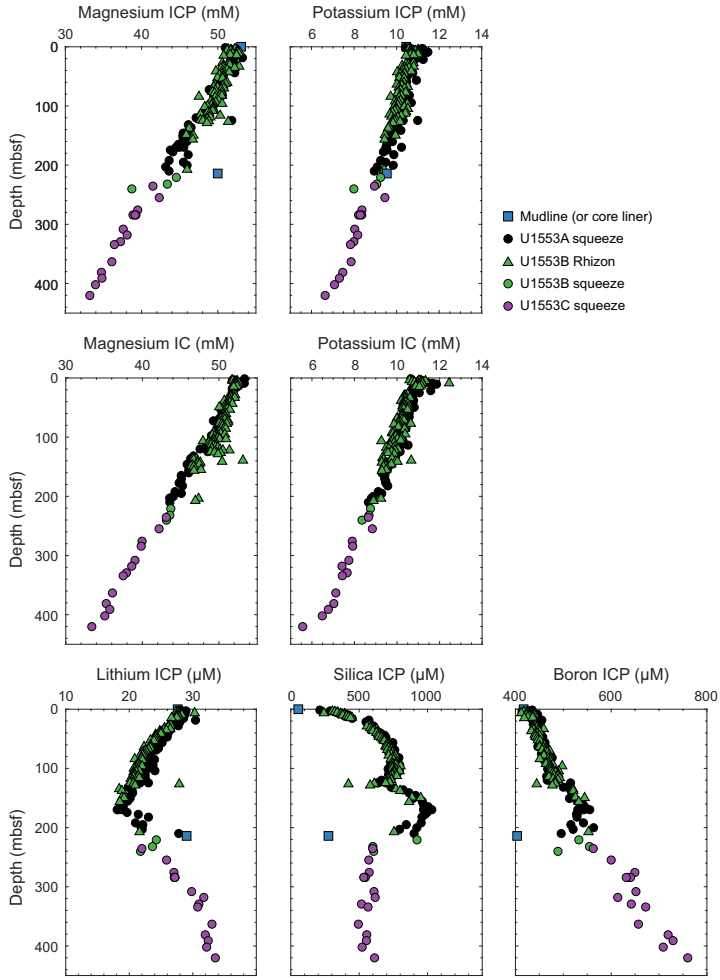

Figure F44. Pore water magnesium, potassium, lithium, silica, and boron concentrations, Site U1553. ICP = inductively coupled plasma–atomic emission spectrometry, IC = ion chromatography.

µM at the mudline to 760 µM at 420 mbsf (Sample 378-U1553C-27R-1, 138–143 cm), possibly because of the dissolution of biogenic carbonates and reprecipitation in B-depleted inorganic carbonates.

6.2.5. Sodium, chloride, bromide, and salinity

IW Na, Cl, and Br profiles reveal trends that may be linked to changes in freshwater and organic matter supply (e.g., Shishkina, 1978). Rhizon and squeeze samples indicate mostly uniform concentrations with depth for Na and Cl and show a ratio similar to seawater, suggesting a dominant seawater origin (Figure **F45**). Na concentrations show no significant downcore trend, although values are scattered between 430 and 550 mM. Cl concentrations measured from squeezers and Rhizon samplers show scatter between ~545 and 565 mM. Br concentrations vary within the lower range expected from seawater, possibly because of low organic carbon input to the seafloor during deposition (Leri et al., 2010). Although Rhizon sample analyses generated for Hole U1553B show larger variations than the squeeze samples derived from the overlapping depth range in Hole U1553A, they follow similar trends, with the exception of Br. The magnitude of Br variability derived from Rhizon samples was not commensurate with the values derived from squeezed samples (Table **T11**) and were therefore not included in the profile. Br concentration decreases gradually from 0.85 mM at the seafloor to 0.8 mM at 130–210 mbsf (Sections 378-U1553A-17H-2 through 27X-1) and remains largely constant through the deepest samples squeezed (all Hole U1553C samples). Salinity measurements with the refractometer resulted in higher values than estimated from Cl alone (assuming a salinity of 35 is equivalent to a Cl concentration of 558 mM). Because salinity was measured on the archive solution several days after collection and because remaining volumes were ≤1 mL for several samples, evaporation could have affected the analysis. Therefore, salinity estimates >37 (beyond the range predicted from Cl concentrations) are not included in Table **T11**. This is demonstrated by comparing the salinity measurements from Holes U1553A and U1553B (Figure **F45**).

6.2.6. Manganese, sulfate, and iron

Mn concentrations in the IW samples are between 0.7 and 1 µM in the uppermost 20 m (Figure **F46**). From 20 to 27 mbsf, Mn concentrations decrease rapidly to ~0.2 µM. Below 27 mbsf, Mn

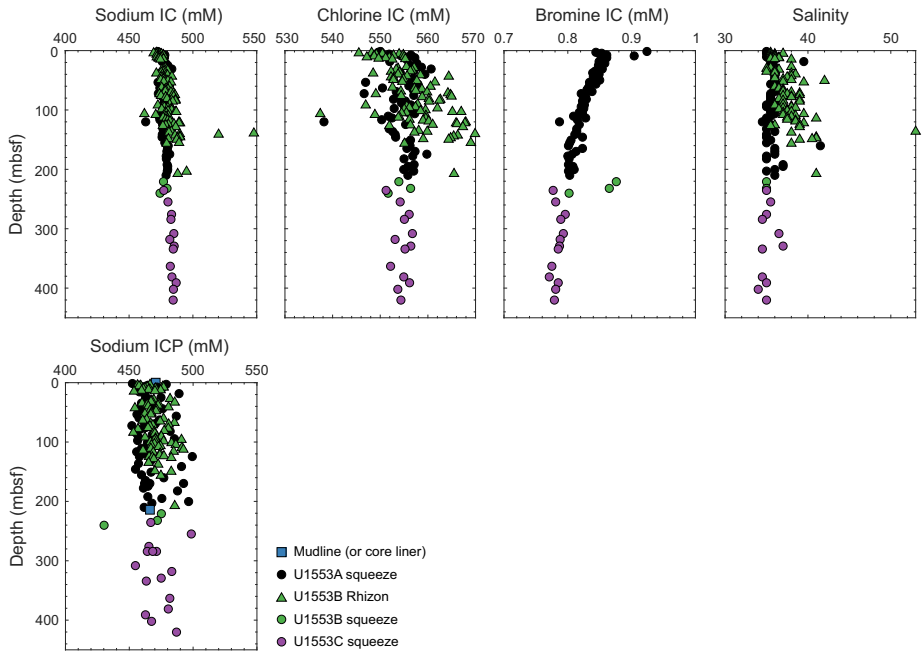

Figure F45. Pore water sodium, chloride, and bromide concentrations and salinity measured with the refractometer, Site U1553. IC = ion chromatography, ICP = inductively coupled plasma–atomic emission spectrometry.

Table T11. Geochemical parameters measured for the liquid phase, Site U1553. **Download table in CSV format.**

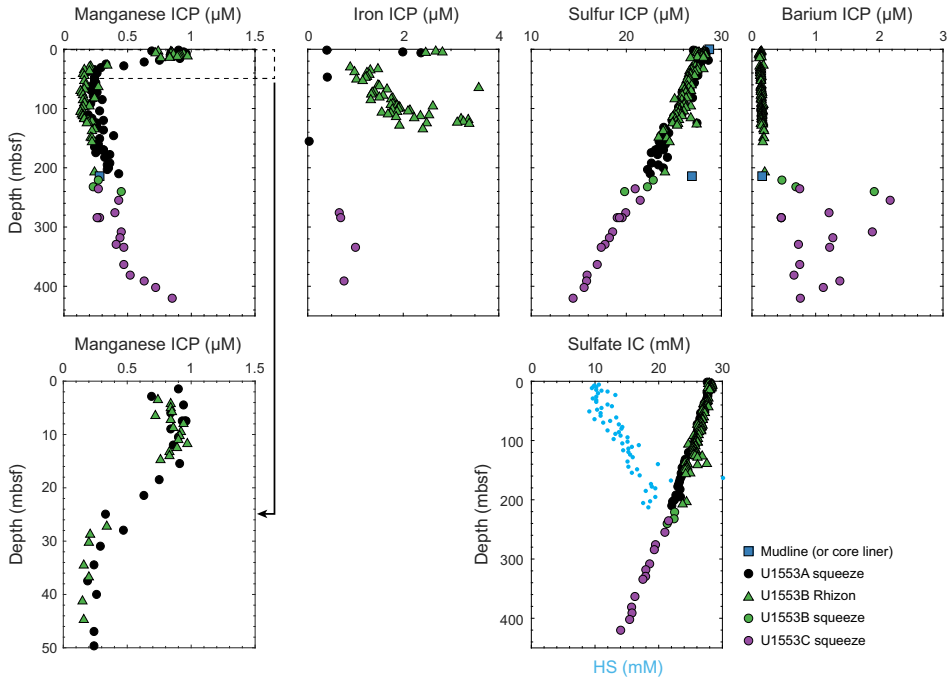

Figure F46. Pore water manganese, iron, sulfur and sulfate, and barium concentrations, Site U1553. Hydrogen sulfide (HS^-) concentrations are calculated from total alkalinity and dissolved inorganic carbon. ICP = inductively coupled plasma spectroscopy, IC = ion chromatography.

concentrations gradually increase with depth to 0.5 µM at 300–363 mbsf and then increase more rapidly to 0.9 µM at 420 mbsf (Sample 378-U1553C-27R-1, 138–143 cm). The higher Mn concentrations near the seafloor suggest Mn oxides are reduced during the oxidation of organic matter. Analyses of the samples below 363 mbsf (Sections 23R-1 through 27R-1) may reflect anaerobic oxidation of methane, which results in Mn reduction and dissolution of Mn oxides and is consistent with XRF measurements (see **Lithostratigraphy**). Sulfate decreases from ~29 mM in the mudline sample to 14 mM at 420 mbsf (Sample 27R-1, 138–143 cm) (Figure **F46**). The smell of sulfide gas was noticeable in Core 34R (~470 mbsf), but the sediment was too lithified to recover any IW and no sulfide measurements were performed. However, the sulfide odor in Core 34R suggests that the sulfate–methane transition zone is ~470 mbsf, where the reduction of sulfate oxidizes methane and produces sulfide. Instead, hydrogen sulfide (HS^-) concentrations (Figure **F46**) estimated by the difference between dissolved inorganic carbon (DIC) and total alkalinity indicate a potential small peak below 140 mbsf. DIC values used to estimate HS^- were derived from alkalinity and pH measurements using the CO2sys.exe software (Pierrot et al., 2006). Fe concentrations decline from ~2 µM at 5 mbsf (Holes U1553A and U1553B) to 1 µM at ~20 mbsf. Fe concentrations increase to >3 µM between 20 and 120 mbsf (Hole U1553B), which may represent Fe oxides being reduced during the oxidation of organic matter. Below 135 mbsf, the majority of samples were below the detection limit, although a few samples had Fe concentrations of 0.5–1 µM below 270 mbsf. Deeper than 135 mbsf, Ba concentrations increase coincident with low Fe concentrations in the pore water, suggesting barite dissolution due to sulfate reduction in the pore waters. This implies Fe was reacting to form an iron sulfide mineral such as pyrite, which was observed in Lithostratigraphic Units II and III (see **Lithostratigraphy**).

6.3. Bulk sediment geochemistry

6.3.1. Carbon content

A total of 96 discrete freeze-dried bulk-sediment samples were measured for calcium carbonate, organic carbon, total nitrogen, and total sulfur. Drastic changes and strong geochemical gradients in carbonate content occur in parallel with the main lithostratigraphic changes. Assuming that all measured inorganic carbon is in the form of calcium carbonate, sediments predominantly consist

of carbonate (90% on average) for the uppermost 420 m of Site U1553, ranging from 78% to 99% ± 0.5% (Figure **F47**). A drastic decrease to 9% carbonate between 420 and 480 mbsf corresponds to marlstone and coincides with a lithostratigraphic transition from limestone to muddy sandstone (see **Lithostratigraphy**). From 480 mbsf (Sample 378-U1553C-38R-1, 35–37 cm) to 580 mbsf (Sample 378-U1553D-20R-5, 28–29 cm), average carbonate content is 2.2%. One exception occurs at 566 mbsf in Sample 378-U1553C-44R-1, 107–108 cm, which contains 85% carbonate and is related to a dolomite-calcite concretion.

Total carbon content shows a similar trend to that of calcium carbonate downhole (Figure **F47**), indicating that most of the carbon is inorganic. Overall, organic carbon content, calculated from total carbon and inorganic carbon, is generally <0.4% ± 0.06% (Figure **F47**). Relatively low organic carbon prevails for the uppermost 200 m (0.14% on average), increasing gradually to 330 mbsf and averaging 0.33% from 330 to 580 mbsf. This observation is in line with a transition from an oligotrophic system to a mesotrophic system, which corresponds with observations from benthic foraminiferal assemblages (see **Biostratigraphy and micropaleontology**). Organic matter degradation and diagenesis are apparent from the geochemical profiles from IW samples (Figures **F42**, **F43**, **F44**, **F45**, **F46**). Total nitrogen content is low (<0.13%) or below the detection limit at Site U1553, which hampers confident estimation of C/N ratios. Total sulfur is only present in the lowermost part of Site U1553 (479–565 mbsf). Average values are <1% and may derive from pyrite minerals, which increase in abundance over this depth range (Table **T12**).

6.3.2. Organic matter source analysis

Headspace gas measurements with low C_1/C_2 ratios prompted the investigation of a possible proximal source of thermogenic gas. Pyrolysis was conducted with the source rock analyzer (SRA) on a set of 19 discrete bulk sediment samples from 295 to 580 mbsf to explore the thermal maturity of Lithostratigraphic Unit V. If no hydrocarbon potential (S_2) is detected, values for T_{max} and other indexes are randomized. This is the case for 11 samples. The presence of hydrocarbons and low petroleum potential are observed in Unit V at Site U1553 from S_1 and S_2 parameters, respectively, for 8 samples (Table **T13**). T_{max} values below 335°C and low production index values indicate

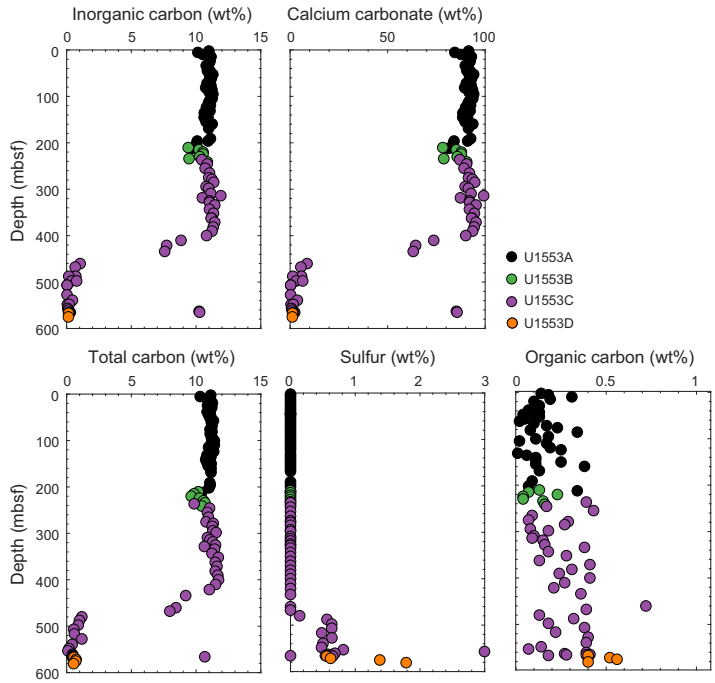

Figure F47. Elemental composition of the solid phase, Site U1553.

Table T12. Carbon, nitrogen, sulfur content of bulk sediment samples, U1553. **Download table in CSV format.**

organic matter is immature. Hydrogen index and oxygen index parameters indicate that the material is primarily of terrestrial origin and is kerogen Type III (Tissot and Welte, 1984). Overall, TOC values are low (<1%). However, linear correlation of TOC values estimated from the difference between total carbon measured on the elemental analyzer and those from IC by coulometry is low (R^2 = 0.39) (Figure **F48**). Large and variable magnitudes of the offsets between values derived from both methods were observed, similar to the TOC values measured using the SRA being higher than those from elemental analyzer coulometry, as has been previously observed and discussed in great detail (e.g., Expedition 317 Scientists, 2011).

6.3.3. Major and trace element concentrations

The major and trace element concentrations (Figure **F49**; Table **T14**) reflect the major change in lithologies at the boundary between Lithostratigraphic Units I–IV and Unit V (see **Lithostratigraphy**). Elements commonly associated with aluminosilicate phases in the sediment are low in Units I–IV. In Units I–IV, concentrations range from 0.8 to 10.3 wt% for SiO_2, from 0.3 to 1.64 wt% for Al_2O_3, from below detection limit to 0.05 wt% for TiO_2, from 0.07 to 0.8 wt% for Fe_2O_3, from 0.03 to 0.3 wt% for K_2O, from 0.2 to 0.6 wt% for MgO, from below detection limit to 35 ppm for Cr, from 0.9 to 2.9 ppm for Sc, and from 10.27 to 35 ppm for V (a few are below detection limit). Zn remains below 53 ppm, and Zr concentrations above the detection limit are ≤16.35 ppm. These elements increase in Unit V and reach maxima of 83 wt% for SiO_2, 8.5 wt% for Al_2O_3, 0.45 wt% for TiO_2, 4.9 wt% for Fe_2O_3, 1.7 wt% for K_2O, 1.6 wt% for MgO, 71 ppm for Cr, 7 ppm for Sc, 61 ppm for V, 193 ppm for Zn, and 199 ppm for Zr. Elements enriched in carbonates have high concentrations in Units I–IV, such as 55.6 wt% for CaO and 1721 ppm for Sr. In Unit V, CaO decreases to as low as 0.15 wt% and Sr decreases to as low as 82 ppm. MnO and Ba are consistently lower than 0.023 wt% and 1070 ppm, respectively, throughout the samples analyzed, except those from between 285 mbsf (Sample 378-U1553C-8R-2, 70 cm) and 480 mbsf (Sample 35R-2, 133 cm), in which concentrations are higher, reaching maxima of 0.06 wt% and 3120 ppm, respectively. Concentrations of Na_2O decrease from ~1 wt% at the seafloor to ~0.5 wt% at ~470 mbsf (Sample 34R-1, 13 cm) and then increase to 0.9–1.3 wt% from 480 to 580 mbsf (Sections 378-U1553C-35R-2 through 378-U1553D-20R-5). Concentrations of P_2O_5 range from 0.04 to 0.24 wt% and do not show a significant change with depth. One sample is from the dolomite concretion at 565 mbsf (Sample 378-U1553C-44R-1, 107–108 cm) and has anomalously high MgO (14.3 wt%), CaO (27.6 wt%), and MnO (0.24 wt%) compared to samples from similar depths.

Table T13. Source Rock Analyses (SRA) of bulk sediment samples, Site U1553. **Download table in CSV format.**

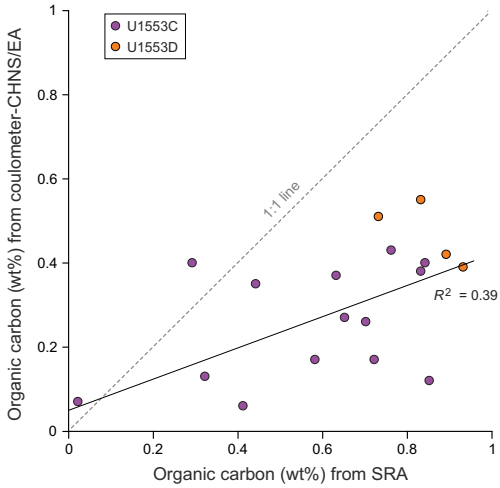

Figure F48. Comparison of total organic carbon results from the coulometer carbon-hydrogen-nitrogen-sulfur (CHNS)/elemental analyzer (EA) method and the source rock analyzer (SRA) method, Site U1553. Note that most data fall below the 1:1 dotted line.

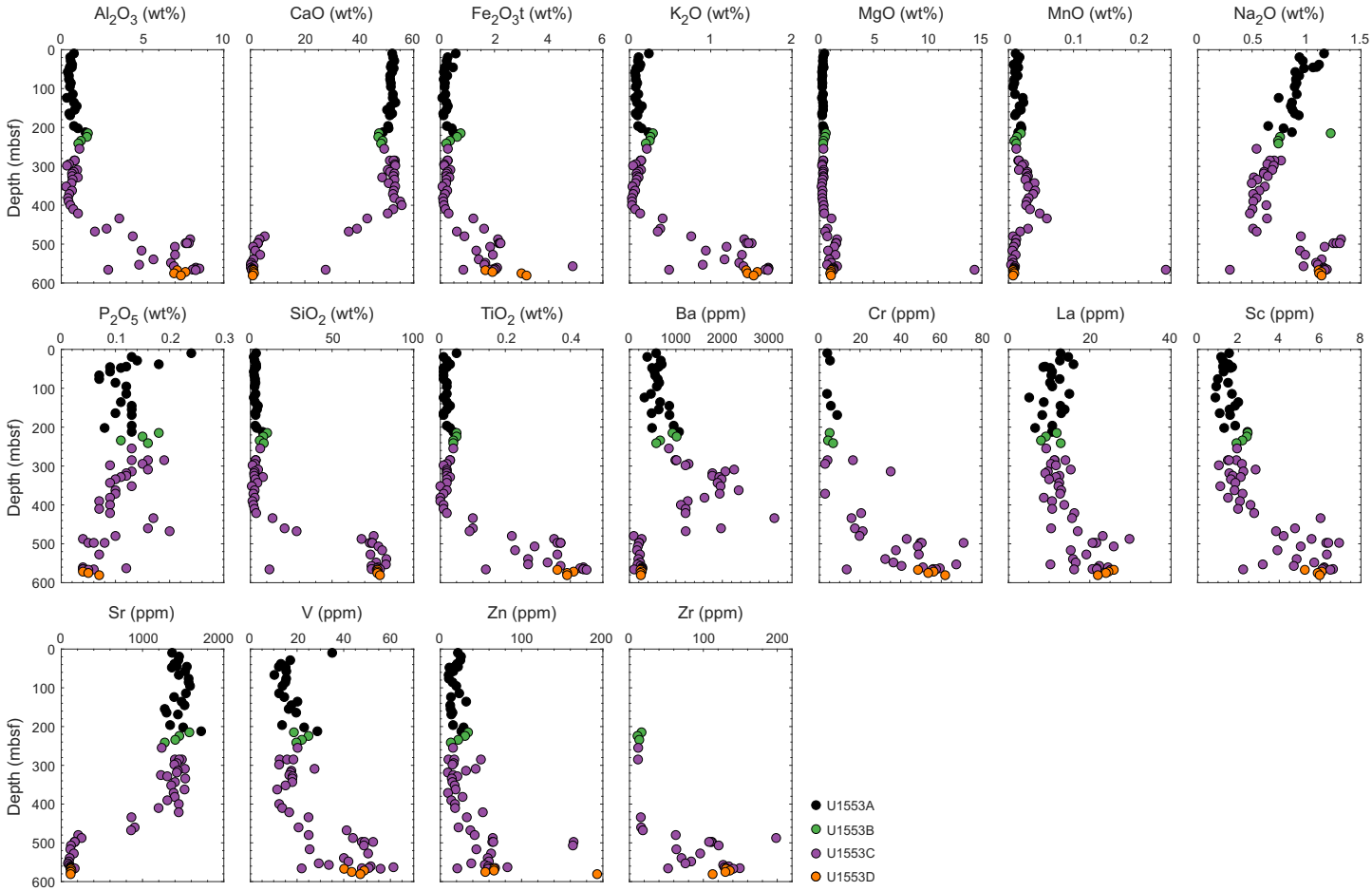

Figure F49. Major and trace element concentrations in sediment samples measured by inductively coupled plasma–atomic emission spectrometry, Site U1553. ppm = parts per million.

Table T14. Major and trace element composition of bulk sediment samples, Site U1553. **Download table in CSV format.**

6.3.4. X-ray fluorescence scanning of Site U1553 cores

Semiquantitative elemental results from XRF scanning of sediment cores were collected from Site U1553. XRF elemental data were collected every 2 cm (see **Major and trace element concentrations**) from all core sections drilled at Site U1553. We acquired raw elemental intensities (total counts) at suborbital resolution for, for example, Al, Si, K, Ca, Ti, Fe, Br, Sr, Zr, and Ba and identify covariation patterns that have been crucial for compiling the spliced composite record that was not accurately possible with shipboard core logging data (see **Stratigraphic correlation**). Our XRF scanning of Site U1553 sediments was conducted to aid in core correlation of the mainly high-carbonate sediments, is consistent with lithofacies variations, and will facilitate detailed interpretation of sedimentation and more detailed paleoceanographic studies at this location.

The XRF scanning data provide a high-resolution record of the geochemistry of the sediments analyzed at Site U1553. Based on shipboard estimated sedimentation rates of 0.5–4 cm/ky for the interval analyzed (see **Age-depth model and mass accumulation rates**), the 2 cm measurement interval yields a temporal spacing of 0.5–4 ky between data points.

7. Physical properties

7.1. Physical properties

Gamma ray attenuation (GRA) bulk density, MS, *P*-wave velocity, NGR, moisture and density (MAD), thermal conductivity, color, reflectance, shear strength, and compressive strength were measured on cores from Site U1553 (for sampling strategy, see **Physical properties** in the Expedition 378 methods chapter [Röhl et al., 2022]). Whole-round *P*-wave velocity, thermal conductivity, discrete shear strength, and compressive strength measurements were not made on RCB cores (Holes U1553C and U1553D). Downhole temperature measurements were taken in Holes U1553A and U1553D.

Variations in physical properties data correspond to transitions between major lithologic units, and in some cases these variations were used to define unit boundaries (see **Lithostratigraphy**). A slight increase in bulk density and NGR at 180 mbsf was used to define the transition between Lithostratigraphic Units II and III. A significant increase in *P*-wave velocity and bulk density at ~423 mbsf marks the top of Lithostratigraphic Unit IV. A large increase in NGR counts, decrease in *P*-wave velocity and bulk density, and change in color at 477 mbsf correspond to the higher silica and clay content of Lithostratigraphic Unit V.

7.2. Gamma ray attenuation bulk density

GRA bulk density was measured on the Whole-Round Multisensor Logger (WRMSL). Variations in GRA bulk density may reflect variations in lithology, consolidation, cementation, and porosity. There is a systematic offset between GRA-measured bulk density and MAD-calculated bulk density in Holes U1553C and U1553D, where RCB coring yielded cores of smaller diameter leading to an underestimation of GRA bulk density by the WRMSL. This systematic underestimation can be corrected to compare with the measured MAD values by multiplying by a correction factor of 1.10. The correction factor was determined by linear regression (R^2 = 0.997; p < 0.0001). Figure **F50** shows the uncorrected raw data to enhance potential quality and accuracy of GRA bulk density data, which strongly depend on the calibration parameters and coring method. From 0 to ~225 mbsf, GRA bulk density increases slowly with depth from an average of 1.6 to 1.7 g/cm^3, which is consistent with the relatively homogeneous calcareous nannofossil ooze lithology of Lithostratigraphic Unit II and compaction downhole (Figure **F50**). GRA bulk density values below 1.5 g/cm^3, such as those in Cores 378-U1553B-3H and 378-U1553A-15H, are associated with poor core recovery and drilling disturbance. Bulk density declines in the uppermost 40 m of Lithostratigraphic Unit III before stabilizing throughout the remainder of the unit (~225–425 mbsf) with uncorrected GRA bulk density values around 1.7–1.8 g/cm^3. These measurements are consistent with the dominant lithology of compacted chalk. The boundary between Units II and III is more clearly observed when the GRA bulk density offset correction is applied because Unit II has a lower average bulk density (~1.7 g/cm^3) than Unit III (~1.9 g/cm^3). At 425 mbsf, the uncorrected GRA bulk density increases from 1.7 to 1.9 g/cm^3 (from 1.9 to 2.1 g/cm^3 in the corrected data), which coincides with the boundary between Lithostratigraphic Units III and IV. GRA bulk density values then remain high and stable to 477 mbsf, where there is a decrease to ~1.5 g/cm^3 (uncorrected) or ~1.7 g/cm^3 (corrected) that corresponds to the boundary between Lithostratigraphic Units IV and V. Variable GRA bulk density values in Lithostratigraphic Unit V may be caused by the lithologic heterogeneity that is pervasive throughout the unit (see **Lithostratigraphy**). Below 520 mbsf in Cores 378-U1553C-41R through 43R and 378-U1553D-16R, there are intervals of extremely low GRA bulk density (~0.5–0.7 g/cm^3) that are associated with darker sections of rubble in Lithostratigraphic Unit V.

7.2.1. Magnetic susceptibility

MS was measured on the WRMSL with a loop and on the Section-Half Multisensor Logger (SHMSL) with a point sensor, increasing resolution and accuracy. MS ranges from –2 to 10 instrument units (IU). Values higher than ~4 IU correspond to the tops and bottoms of cores and core sections where sediments are most likely to be disturbed or poorly measured on the logger tracks (Figure **F50**). Throughout the upper 425 m of Site U1553, MS remains near zero (ranging from –2 to 2 IU), which is

consistent with the predominantly carbonate lithology, except for drilling disturbances in Cores 378-U1553A-15H and 378-U1553B-3H where suck-in occurred. MS slightly increases to ~3–4 IU throughout Lithostratigraphic Unit IV (425–477 mbsf). In Lithostratigraphic Unit V (477–577 mbsf), MS is elevated compared to the upper units but is still relatively low, ranging from 0 to 4 IU.

7.2.2. *P*-wave velocity

Between 0 and ~175 mbsf, *P*-wave velocities remain constant at ~1600 m/s. The high *P*-wave values of ~4400 m/s at ~130 mbsf derived from the packstone layer recovered in Core 378-U1553A-16X. Whole-round *P*-wave measurements from the WRMSL are consistent with discrete *P*-wave caliper measurements made on selected section halves and discrete MAD cubes. Below 175 mbsf, *P*-wave velocities were measured using only the Section Half Measurement Gantry (SHMG) (see **Physical properties** in the Expedition 378 methods chapter [Röhl et al., 2022]). Between 175 and 425 mbsf, *P*-wave velocities gradually increase to ~2000 m/s. In this interval, some discrete measurements were also taken on the interbedded chert layers, which recorded higher *P*-wave velocities (3000–4200 m/s) than the majority of Lithostratigraphic Unit III. A sharp increase in *P*-wave velocity from ~2000 to 2600 m/s occurs at 425 mbsf, which coincides with the boundary between Lithostratigraphic Units III and IV. *P*-wave values gradually decrease throughout Lithostratigraphic Unit IV (425–477 mbsf) to approximately 2100 m/s. In Lithostratigraphic Unit V, *P*-wave velocities remain at ~1900–2000 m/s.

7.2.3. Natural gamma radiation

NGR was measured on whole-round sections with the Natural Gamma Radiation Logger (NGRL) (Figure **F51**). NGR measurements at Site U1553 ranged from 0 to 40 counts/s. Consistent with other physical properties measurements, NGR and the constituent elemental concentrations

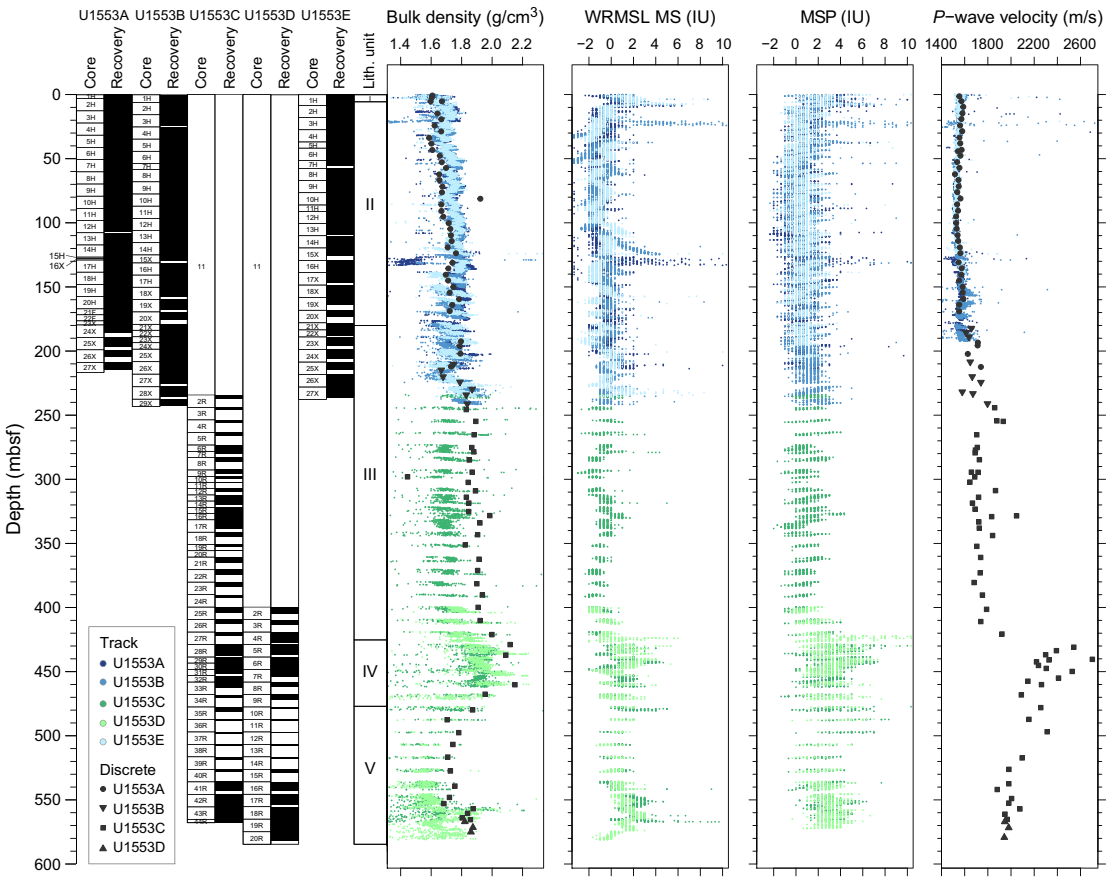

Figure F50. Gamma ray attenuation (GRA) bulk density, Whole-Round Multisensor Logger (WRMSL) magnetic susceptibility (MS), Section-Half Multisensor Logger point MS (MSP), and *P*-wave velocity, Site U1553. GRA bulk density values for Holes U1553C and U1553D are the raw, uncorrected values. Discrete measurements are superimposed in black.

remain low and constant between ~0 and 180 mbsf, which corresponds to the homogeneous carbonate lithology of Lithostratigraphic Unit II. Between 180 and 240 mbsf, there is a transient increase in NGR values to ~10 counts/s (~225 mbsf) followed by a decrease to ~5 counts/s. NGR then remains constant to 425 mbsf, where an increase in the average value (from ~5 to 15 counts/s) coincides with the transition from Lithostratigraphic Unit III to Unit IV. NGR values remain elevated but variable throughout Lithostratigraphic Unit IV (425–477 mbsf). At 477 mbsf, there is a sharp increase in NGR counts associated with the boundary between Lithostratigraphic Units IV and V. Although data are sparse between ~477 and 540 mbsf because of poor core recovery, NGR counts in Lithostratigraphic Unit V are variable (10–40 counts/s). Similar to GRA bulk density measurements, this is likely a result of the heterogeneous lithology, and NGR counts remain greater than values observed in the overlying carbonate units. The NGR spectra were also deconvolved into approximated uranium, thorium, and potassium concentrations using the interpolated MAD-derived bulk density values and methods described by De Vleeschouwer et al. (2017). U, Th, and K concentrations covary throughout most of the hole. The U/Th ratio increases at the Lithostratigraphic Unit IV/V boundary, coinciding with the increased clay content of the sediments.

7.2.4. Moisture and density

To achieve a continuous downhole record, two carefully selected samples were taken from each Hole U1553A core and from Cores 378-U1553B-26X through 29X, 378-U1553C-3R through 44R, and 378-U1553D-19R and 20R for MAD analysis. Care was taken to cover representative lithologies and to avoid intervals of obvious drilling disturbance, and special caution was taken to exclude intervals with potentially critical boundaries. The ~10 cm^3 samples were measured for wet mass, dry mass, and dry volume. Using these measurements, bulk density, grain density, porosity, and salt volume were calculated. Throughout Lithostratigraphic Units I–III (0–425 mbsf), bulk density gradually increases downhole from 1.6 to 1.9 g/cm^3. This is followed by a transient decrease in bulk density to 1.6 g/cm^3 at 220 mbsf alongside a decrease in porosity from 65% to 45% (Figure **F52**). Grain density remains near constant at 2.7 g/cm^3 to 450 mbsf. This is consistent with a near-pure carbonate lithology undergoing increasing compaction downhole (Figure **F53**). Coincident declines in salt volume and porosity, alongside an increase in NGR counts/s between 170 and 225 mbsf, mark the gradual transition between the carbonate ooze of Lithostratigraphic Unit II and the chalk that is characteristic of Lithostratigraphic Unit III. At 425 mbsf, porosity declines to 35% and bulk density increases to 2.1 g/cm^3, marking the transition to the limestone of Lithostratigraphic Unit IV. Throughout Lithostratigraphic

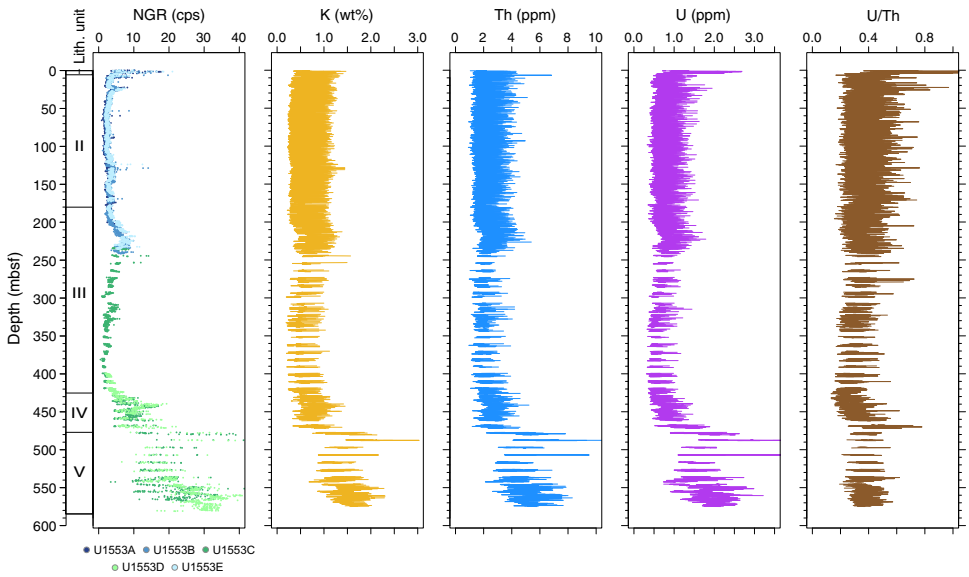

Figure F51. Whole-round natural gamma radiation (NGR) data, Site U1553. NGR = total counts. K, Th, and U = estimated concentrations. cps = counts per second, ppm = parts per million

Unit V (below 477 mbsf), decreased but variable grain density ranges from 2.1 to 2.6 g/cm^3. Bulk density is also lower in Lithostratigraphic Unit V, averaging around 1.7 g/cm^3 and increasing slightly at the base of the hole to 1.85 g/cm^3. The observed variability in bulk density, porosity, and grain density is consistent with the heterogeneous lithology observed throughout the unit (Figure **F53**).

7.2.5. Thermal conductivity, temperature, and heat flow

Thermal conductivity was measured on cores with good recovery and softer lithologies that are conducive for measurements. Measurements were generally collected in the third section of each core. Because of lithification, measurements were only collected to 241 mbsf. Thermal conductiv-

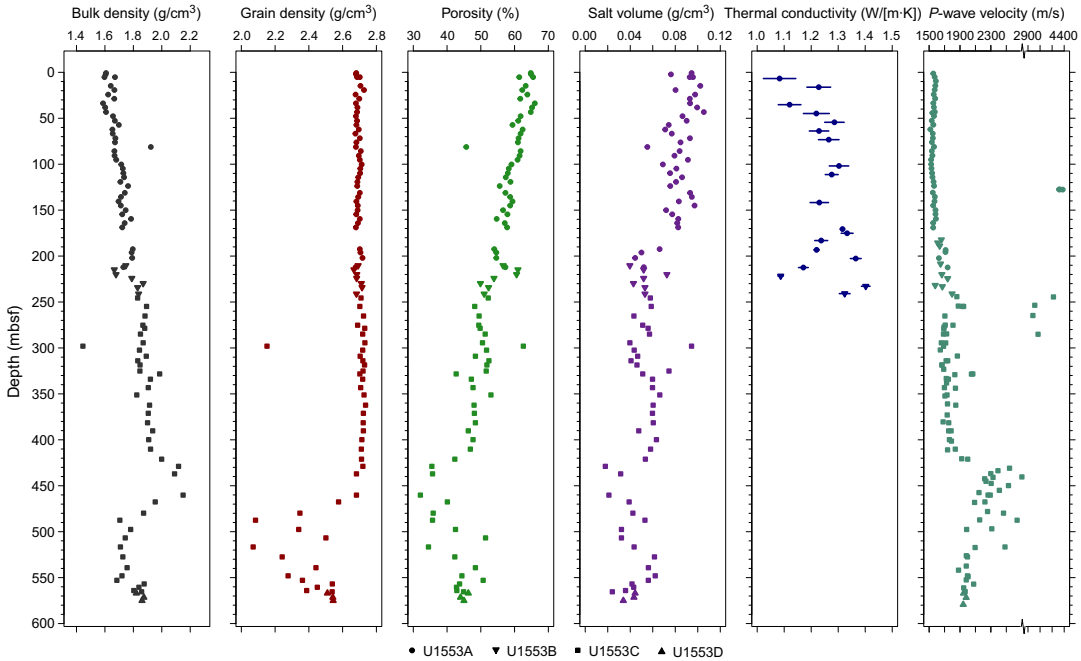

Figure F52. Discrete bulk density, grain density, porosity, salt volume, thermal conductivity, and *P*-wave velocity measurements, Holes U1553A–U1553D. No discrete measurements were taken for Hole U1553E. *P*-wave velocity has a split *x*-axis to show the higher velocities measured in the packstone and chert layers.

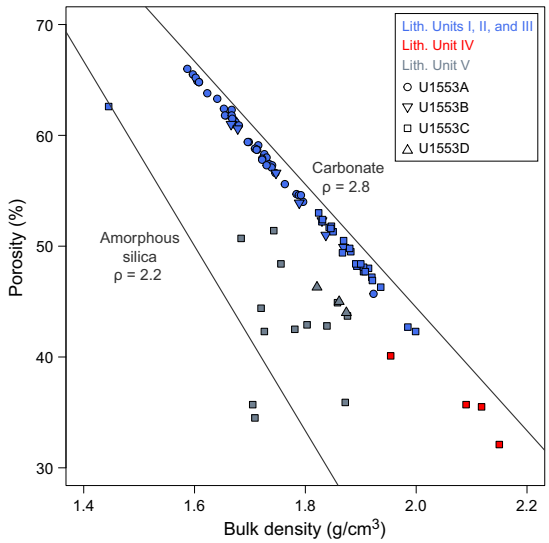

Figure F53. Cross-plot of bulk density and calculated porosity of discrete moisture and density samples, Holes U1553A–U1553D. Lines are calculated relationships for constant grain density that correspond approximately to carbonate (2.8 g/cm^3) and amorphous silica (2.2 g/cm^3).

ity measurements ranged from 1.1 to 1.4 W/m^2, did not vary significantly with depth, and were often compromised because of poor contact between the needle probe and the sediment.

Downhole temperature measurements were collected from Cores 378-U1553A-4H, 7H, and 10H (31.5, 60, and 88.5 mbsf, respectively) using the APCT-3 tool and from 181 mbsf in the drilled interval of Hole U1553D (Section 1-1) using the SET2 tool (Table **T15**). Temperatures ranged from 5.83°C at 31.5 mbsf in Hole U1553A to 15.63°C at 181 mbsf in Hole U1553D. Calculations of heat flow at Site U1553 resulted in a value of 80 mW/m^2 following the methods outlined in Pribnow et al. (2000) and using an average approach. However, this value should be considered with care because there was no systematic downhole trend in the calculated thermal conductivity.

7.2.6. Reflectance spectrophotometry and colorimetry

Reflectance spectroscopy colorimetry (RSC) and RGB color space data were measured on the surface of archive-half sections at a 2.5 cm resolution for L*, a*, and b* and at a 1 cm resolution for RGB (Figure **F54**). From 0 to ~425 mbsf, high RGB values of ~220 reflect the light color of the cores, which is typical of Lithostratigraphic Units II and III. The high reflectance of this core interval is also indicated by a high L* value of about 80. From 0 to 20 mbsf, the b* values increase from 0 to 10, indicating more yellow colors. From ~25 to ~425 mbsf, L*, a*, and b* values vary only slightly. Changes in the RSC and RGB data correspond to the Lithostratigraphic Unit III/IV boundary. Throughout Lithostratigraphic Unit IV, from 425 to 477 mbsf, sediments become

Table T15. Summary of downhole temperature measurements, Site U1553. **Download table in CSV format.**

Core	Depth (mbsf)	Temperature (°C)
378-U1553A-		
4H	31.5	5.83
7H	60	7.61
10H	88.5	8.97
378-U1553D-		
1-1	181	15.63

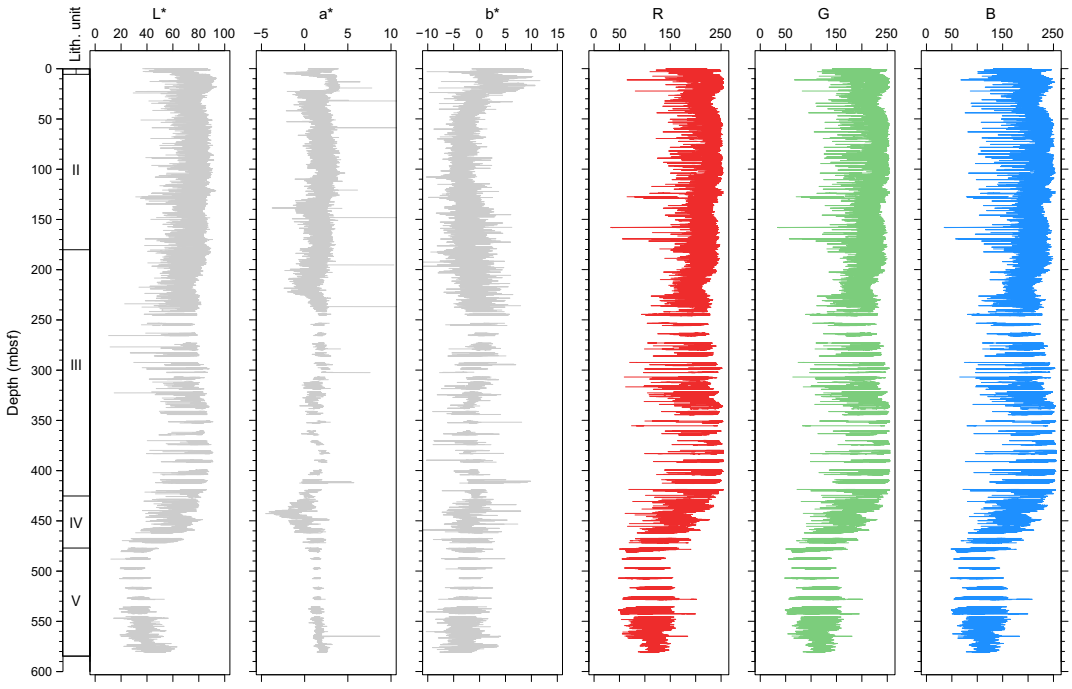

Figure F54. Section Half Imaging Logger color reflectance and red-green-blue (RGB) color channels combined across all holes, Site U1553. For Lithostratigraphic Unit V, RGB values were collected after allowing the cores to fully dry (see Lithostratigraphy in the Expedition 378 methods chapter [Röhl, 2022]).

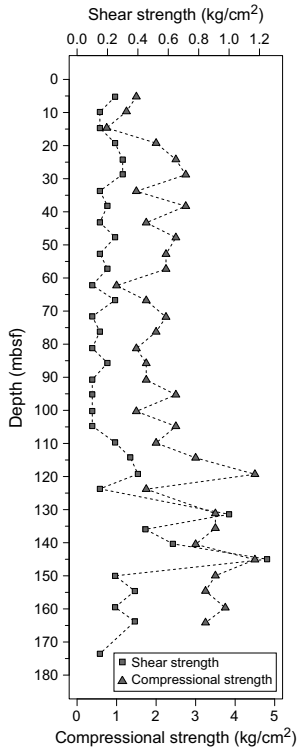

Figure F55. Sediment compressional and shear strength, 0–180 mbsf, Hole U1553A.

darker and L* values decrease from 80 to 50. RGB channels decrease from 220 to 100 to the base of the unit (~477 mbsf). At ~445 mbsf, a* values reach a minimum value of –4, indicating the presence of an enhanced green interval. Below 477 mbsf, relatively low L* values (~30) and RGB values (~100–150) reflect the darker sediments of Lithostratigraphic Unit V.

7.2.7. Shear and compressional strength

Sediment shear strength and compressional strength were measured on two section halves per core in Hole U1553A using the handheld Torvane and penetrometer, respectively (Figure **F55**). Compressional and shear strength were not measured below Section 21F-2 because of increased lithification of the sediments that exceeded instrument measurement limits and the potential presence of critical boundaries. Shear strength varies from ~0.1 to 0.3 kg/cm^2 between 1 and ~100 mbsf, followed by increased variability from 0.15 to 1.25 kg/cm^2 between ~114 and 173 mbsf. Compressional strength is relatively constant at approximately 2.0 kg/cm^2 for the uppermost 110 m and increases to 3.5–4.5 kg/cm^2 downsection.

8. Stratigraphic correlation

Final core offsets and a splice for Site U1553 were not completed until ~7 months postcruise following XRF scanning at the Gulf Coast Repository in College Station, Texas (USA). Cores recovered using the APC and XCB coring systems in Holes U1553A, U1553B, and U1553E, which seem to be in good condition and have reasonable recovery rates, were difficult to correlate on board *JOIDES Resolution*. The combined effects of the carbonate-rich lithology, the age of the sediments, their postdepositional history, and occasional drilling disturbance, mostly at the top of the cores (i.e., the first section), made it difficult to identify precise tie points between holes using the scanning data collected on board the ship. GRA density scans, usually reliable for piston-cored sediments, at times exhibited variability within cores that was not recognizable in cores from adjacent holes at similar depths (mbsf scale). Natural gamma ray and MS traces were invariant for most of the cored intervals, although natural gamma ray did play a vital role in tying together Cores 378-U1553A-1H through 3H, 378-U1553B-1H through 3H, and 378-U1553E-1H through 3H at the top of the holes, as well as

Cores 378-U1553C-28R through 32R and 378-U1553D-4R through 7R, which span the late Paleocene to early Eocene, including a possible PETM sequence and, deeper, the early Paleocene. Parameter a* (RSC) was the only useful color-related data. The RGB color space profiles have 1.5 m section-related cycles, and scans of core sections are slightly darker at the top than at the bottom. This artifact was only noticeable because of the extremely limited range of colors in the recovered core. Core images, usually helpful in tying holes to one another, did not show enough variability to be useful in most instances. XRF scans overcame many of the problems encountered in the shipboard data and were used as the primary source for setting offsets and splices in Holes U1553A, U1553B, and U1553E. Cumulative offsets for all five holes at Site U1553 are provided in Table **T16**, and splice intervals are given in Table **T17**.

In the following discussion, we will address separately the holes cored using the APC and XCB tools (Holes U1553A, U1553B, and U1553E) and those cored using the RCB system (Holes U1553C and U1553D). A core image splice is presented in Figure **F56**. Although there are a few possible gaps in

Table T16. Cumulative offsets, Site U1553. These values are added to the drilling depth (mbsf) for each core to calculate composite depths (CCSF). Core section 1-1 is a drilled interval. **Download table in CSV format.**

Core, section	Offset (m)	Core, section	Offset (m)	Core, section	Offset (m)	Core, section	Offset (m)	Core, section	Offset (m)
378-U1553A-		378-U1553B-		378-U1553C-		378-U1553D-		378-U1553E-	
1H	0	1H	0.10	1-1	31.34	1-1	31.34	1H	0.84
2H	–0.30	2H	0.29	2R	31.34	2R	31.34	2H	0.95
3H	0.14	3H	0.93	3R	31.34	3R	31.34	3H	1.66
4H	2.26	4H	0.73	4R	31.34	4R	31.34	4H	2.14
5H	1.39	5H	1.88	5R	31.34	5R	30.32	5H	2.64
6H	2.85	6H	2.34	6R	31.34	6R	32.52	6H	3.36
7H	3.85	7H	1.93	7R	31.34	7R	32.63	7H	3.93
8H	2.71	8H	2.01	8R	31.34	8R	34.03	8H	4.16
9H	3.86	9H	2.32	9R	31.34	9R	32.63	9H	4.76
10H	3.89	10H	3.05	10R	31.34	10R	32.63	10H	5.76
11H	4.99	11H	3.92	11R	31.34	11R	32.63	11H	6.55
12H	6.85	12H	5.47	12R	31.34	12R	32.63	12H	8.35
13H	6.99	13H	5.51	13R	31.34	13R	32.63	13H	9.15
14H	8.11	14H	5.52	14R	31.34	14R	32.63	14H	9.19
15H	6.05	15X	5.60	15R	31.34	15R	32.63	15X	10.41
16X	11.05	16H	6.85	16R	31.34	16R	32.63	16H	11.27
17H	9.79	17H	7.87	17R	31.34	17R	32.63	17X	12.90
18H	9.76	18X	9.51	18R	31.34	18R	36.19	18X	14.24
19H	11.40	19X	10.94	19R	31.34	19R	36.75	19X	15.24
20H	12.10	20X	12.32	20R	31.34	20R	36.75	20X	16.10
21F	12.70	21X	10.60	21R	31.34			21X	15.00
22F	13.00	22X	12.63	22R	31.34			22X	16.00
23X	13.83	23X	14.19	23R	31.34			23X	18.02
24X	14.83	24X	14.19	24R	31.34			24X	23.58
25X	13.63	25X	16.19	25R	31.34			25X	24.85
26X	18.00	26X	18.19	26R	31.34			26X	24.00
27X	19.96	27X	18.09	27R	31.34			27X	24.42
		28X	22.42	28R	30.83				
		29X	21.83	29R	30.50				
				30R	31.58				
				31R	32.67				
				32R	32.87				
				33R	33.37				
				34R	32.43				
				35R	31.42				
				36R	32.87				
				37R	32.87				
				38R	32.87				
				39R	32.87				
				40R	32.87				
				41R	32.72				
				42R	33.69				
				43R	37.35				
				44R	40.35				

Table T17. Splice intervals, Site 1553. **Download table in CSV format.**

the APC/XCB splice, recovery was much better than for the RCB system. The deepest APC/XCB core, 378-U1553B-29X, overlaps in mbsf depth with the first rotary core (378-U1553C-2R; the first core after a drilled interval). However, calcareous nannofossil biostratigraphy (Table **T2**) indicates that Core 378-U1553C-2R may overlap with the shallow holes approximately 20 m higher in the section (e.g., Cores 378-U1553A-25X, 378-U1553B-26X, and 378-U1553E-25X). Such a large difference in mbsf depth seems unjustified, especially because barium-strontium ratio values (Figure **F57**) in Core 378-U1553C-2R are roughly half the values in Cores 378-U1553A-25X, 378-U1553B-26X, and 378-U1553E-25X. Poor recovery from the top of Hole U1553C (the first three cores from Hole

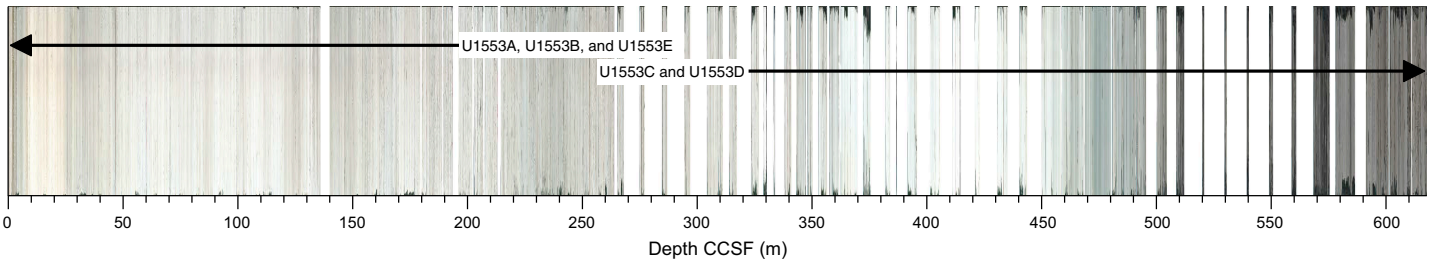

Figure F56. Spliced core image. Holes U1553A, U1553B, and U1553E were piston cored to approximately 160 m CCSF and cored with the extended core barrel (XCB) system below that depth. Holes U1553C and U1553D were cored with the rotary core barrel (RCB) system. Recovery was much better in the softer sediments using the APC/XCB bits.

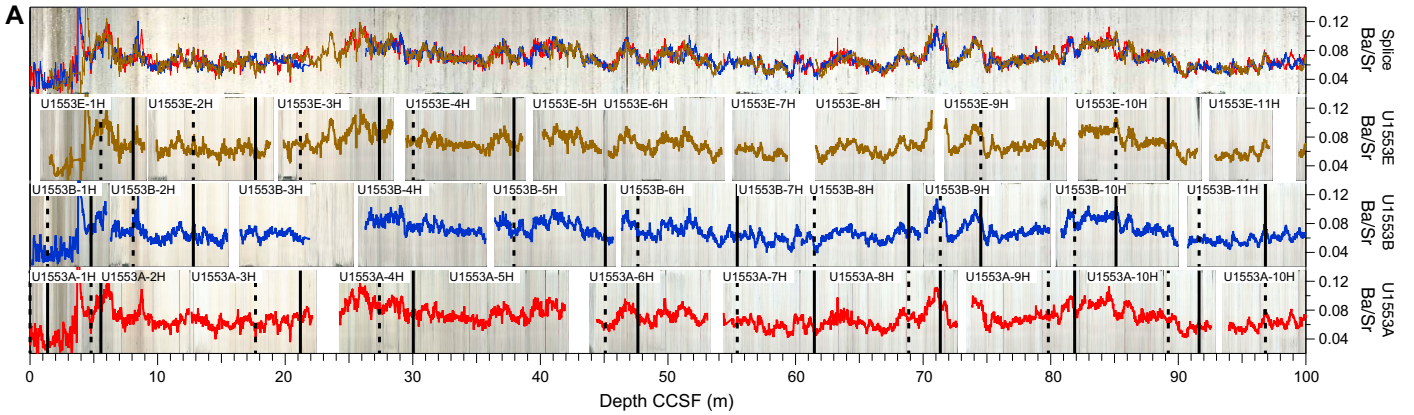

Figure F57. Core images and Ba/Sr data plotted against shifted depth (CCSF scale), Holes U1553A, U1553B, and U1553E. Ba/Sr data from all three holes are plotted on a single axis over the spliced image at the top of the figure. Dashed black vertical lines = tops of spliced intervals, solid black vertical lines = bottoms of spliced intervals. Disturbed core has been removed from the core images so that in some cases labels or data seem to extend beyond the core image boundaries. Please be advised not to use those intervals of data for correlation or analysis. A. 0–100 m CCSF. (Continued.)

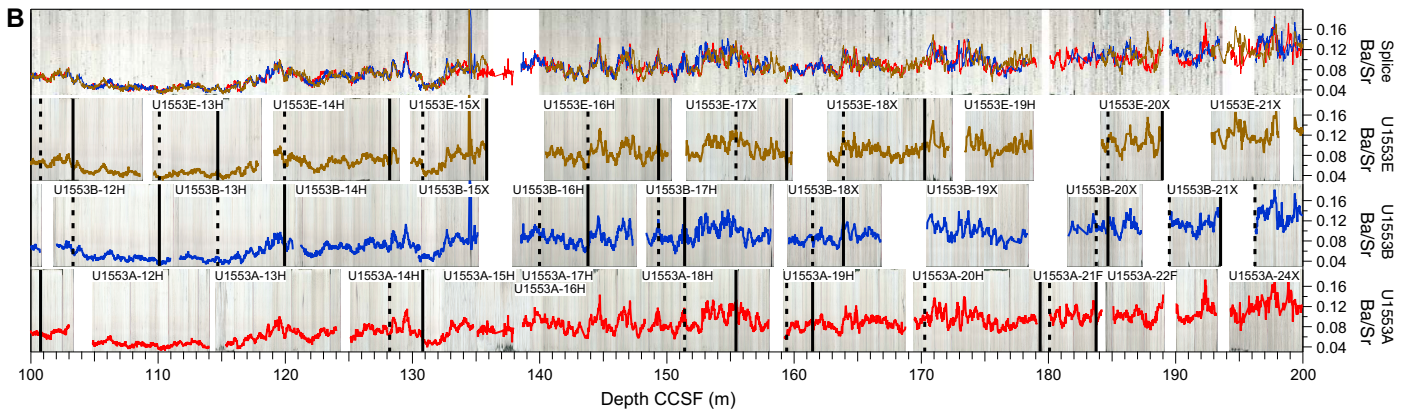

Figure F57 (continued). B. 100–200 m CCSF.

U1553C have a total recovery of 7.5 m) calls into question whether the recovered cores span overlapping depths. Because scan data do not suggest a tie between the two cores and a 20 m adjustment to mbsf depth seems overly large, we decided to offset the data from the rotary cores such that the top of Core 378-U1553C-2R is below Core 378-U1553B-29X rather than imply correlation where none can be found. Fortunately, any future revision of the overlap between Holes U1553B and U1553C will not have any effect on the relative spacing of samples between Holes U1553C and U1553D lower in the section.

8.1. Holes U1553A, U1553B, and U1553E

The barium-strontium ratio (Ba/Sr) derived from XRF scans is plotted on top of core images in Figure **F57**. The data from individual holes are plotted against a single axis at the top of the figure. A spliced core image is also included under the single-axis Ba/Sr data. Cores are labeled, and splice sections are indicated by vertical lines at the tops and bottoms of splice intervals. Disturbed core has been removed from the core images so that in some cases labels or data seem to extend beyond the core image boundaries. This is a reminder not to use those bits of data for correlation or analysis.

Between the seafloor and 100 m core composite depth below seafloor (CCSF) (Figure **F57A**), we have pieced together a robust continuous record. A gap that is spanned by only a single record occurs at 23 m CCSF, but reasonable fits between data from Holes U1553A and U1553E above and below this interval suggest that recovery is complete there. Note also that there appear to be intervals of misfit evident in the plot of Ba/Sr on the single axis. This is the result of the often unequal thickness of correlatable events in the data. For instance, if a feature observed near the top of two cores is aligned, there may be features deeper in the core that do not share the same alignment. An example can be seen at 86 m CCSF. This misfit may only be remedied by expanding and compressing data within cores, which is beyond the scope of this report.

The quality of the splice is high to approximately 134 m CCSF (Figure **F57B**), where cherts were encountered, resulting in poor recovery. Chert (or at least some chert) was the only sediment recovered from Core 378-U1553A-16A, but Holes U1553B and U1553E recovered intercalated sediment with the chert. Nevertheless, there is a good possibility of missing 1 m or so of section here.

The splice becomes tenuous from 180 to 214 m CCSF. Core 378-U1553A-21F is appended to the bottom of Core 20H. Disturbance at the top of Core 21F creates a gap in the splice, and it is important to remember that in any instance where a core is appended to a core above, there is most likely a missing section between them. Between 190 and 223 m CCSF, a combination of half cores and modest recovery created a major splicing challenge. We decided to carry the splice through a series of appends of Cores 378-U1553B-20X through 25X. Cores from Holes U1553A and U1553E were aligned as best possible, but no firm splices were identified. This is a critical area spanning the EOT. Isotope studies of cores in this interval from all three APC holes should help

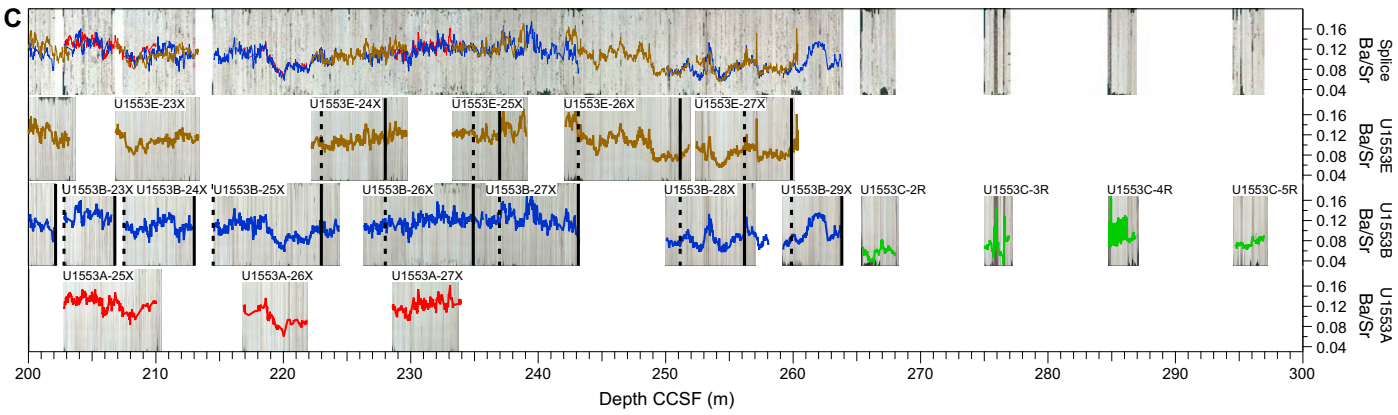

Figure F57 (continued). C. 200–300 m CCSF.

further refine our understanding of the sedimentary progression. Below 215 m CCSF, variability in the data and somewhat better recovery allow construction of a continuous record (Figure **F57C**).

Holes U1553C and U1553D penetrate into the sedimentary succession from the base of Hole U1553B at 263 m CCSF to a total depth of 618 m CCSF in Hole U1553D. Much of the cored interval in Holes U1553C and U1553D was poorly recovered (Figure **F56**), and coring in Hole U1553D only began at 430 mbsf. The probable PETM, however, was well captured by Cores 378-U1553C-28R through 32R and 378-U1553D-4R through 7R and is illustrated in a plot of natural gamma ray data superimposed on core images (Figure **F58**). The PETM occurs just below the pale interval between 481 and 482 m CCSF. Sedimentation rates calculated for these cores (Figure **F63**) suggest that coring captured matter from approximately 0.5 My prior to the possible PETM and extending almost continuously to approximately 1 My after, with a good chance of more in overlying cores of Hole U1553D.

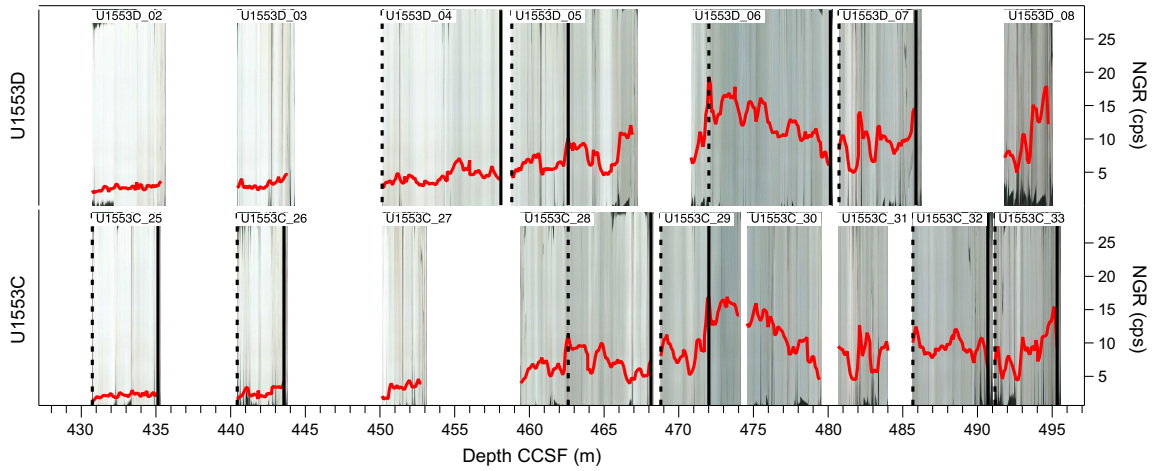

Figure F58. Core images and natural gamma radiation (NGR) data plotted against shifted depth (CCSF scale), Holes U1553C and U1553D. Poor recovery made correlation impossible except for Cores 378-U1553C-28R through 32R and 378-U1553D-4R through 7R. The Paleocene/Eocene Thermal Maximum appears just below the white interval between 481 and 482 m CCSF. Dashed black vertical lines = tops of spliced intervals, solid black vertical lines = bottoms of spliced intervals. cps = counts per second.

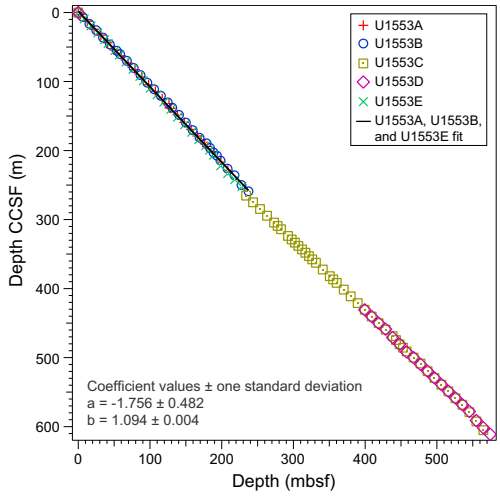

Figure F59. CCSF depths to the top of each hole plotted versus original mbsf depths. The slope of the fit to the data of 1.094 indicates that the CCSF depth is approximately 9% greater than the mbsf depth in Holes U1553A, U1553B, and U1553E. Holes U1553C and U1553D were not included in the fit because the offset in these holes was a constant carried from the bottom of the shallow holes (Core 378-U1553B-29X) almost to the bottom.

Comparison of mbsf depth with CCSF depth (Figure **F59**) indicates that CCSF is approximately 9% greater than mbsf in Holes U1553A, U1553B, and U1553E based on the slope of the best fit to the data. Note that Holes U1553C and U1553D are not included because they have an almost constant offset, and no shifting was done to cores from those holes other than some small adjustments in the late Paleocene to early Eocene and deeper down in the hole in early Paleocene cores.

9. Age-depth model and mass accumulation rates

The age-depth model developed for Site U1553 is based on an integrated sequence of datums derived from shipboard biostratigraphy and magnetostratigraphy (Table **T18**). The micropaleontologists examined all five holes in similar detail, whereas the paleomagnetists focused on Holes U1553A and U1553C. Because of difficulties in establishing a spliced composite record with shipboard data and providing the age-depth information for all the cored holes, the current model is based on depth measured as meters below seafloor for all five holes (Figures **F60**, **F61**). Core composite depth below seafloor depths that resulted from preliminary correlation of physical properties track data from parallel holes (see **Stratigraphic correlation**) are also listed in Table **T18**. Datums are placed at midpoints for biostratigraphy and between inflection points in the inclination data for magnetochron boundaries. All datum ages are based on the geologic timescale of Gradstein et al. (2012). See **Biostratigraphy and micropaleontology** for more detailed descriptions of datums and biozones and **Paleomagnetism** for a more detailed description of the basis for magnetochron delineation.

Table T18. Biostratigraphic and magnetostratigraphic datums, Site U1553. (This table is available in an **oversized format**.) **Download table in CSV format**.

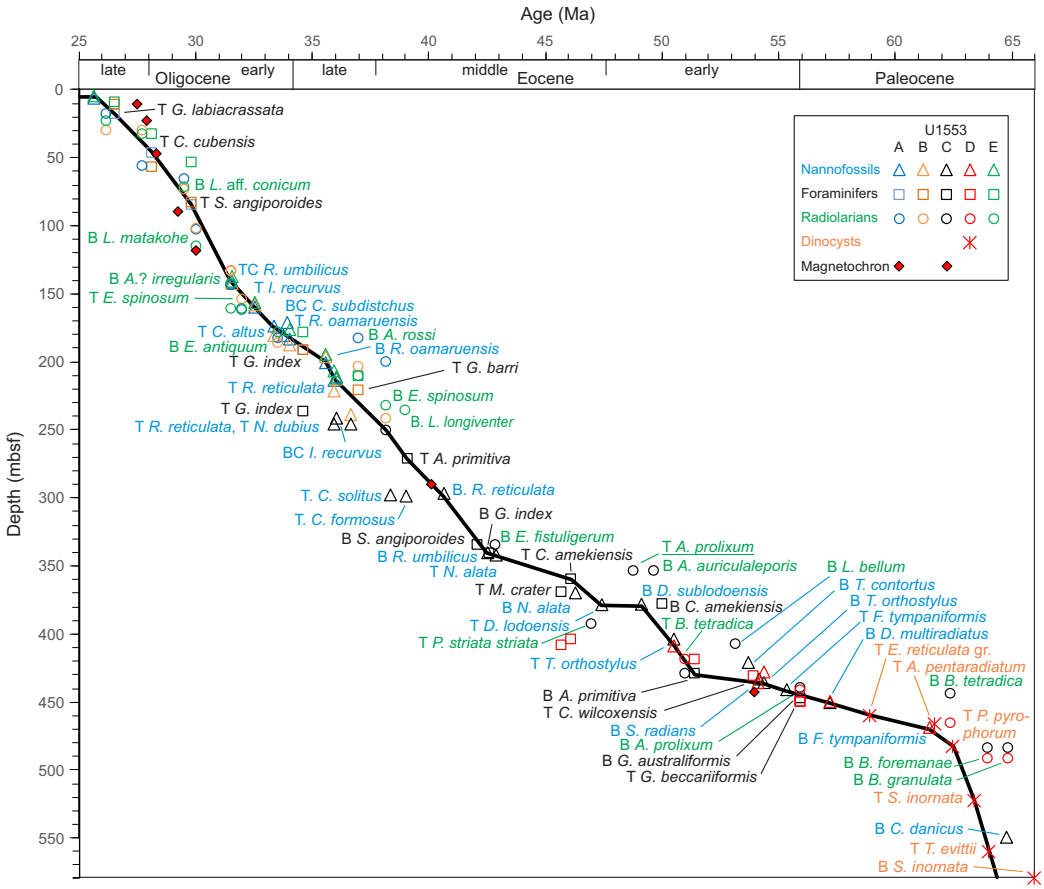

Figure F60. Age-depth plot, 25–66 Ma, Site U1553. Underlined datum = age reversal. T = top, B = base, TC = top common occurrence, BC = base common occurrence.

9.1. Age-depth model

The age-depth model is based mainly on datums from Holes U1553A, U1553C, and U1553D. Although general agreement exists among holes, there are significant offsets between datums from Holes U1553A, U1553B, and U1553E in some intervals. We hope these offsets will be reconciled once higher resolution onshore biostratigraphic data and a refined composite record are established. The shipboard datums were primarily identified with a ~10 m resolution for foraminifers and radiolarians and a ~1.5 m resolution for calcareous nannofossils. The line of correlation is constructed by connecting primary datums where possible (Table **T19**). Where there is a conflict between datums, the line is drawn to ensure most of the datum bases are above the line and most of the datum tops are below the line. Datum bases below the line and datum tops above the line are referred to as age reversals. A datum top above the line of correlation implies the marker species ranges higher than its established range. Similarly, a datum base below the line of correlation implies that the marker species ranges lower than its established range. Such range extensions are unlikely for well-known species and are considered to signify a problem with the age model or with the datum range.

In broad terms, the age-depth plot for all datums identified at Site U1553 shows general agreement between biostratigraphic and magnetostratigraphic datums and within the microfossil groups (Figure **F60**). However, it was not possible to reconcile detailed biostratigraphy and magnetostratigraphy in the upper part of the Oligocene (Figure **F61**). Neither of the two options for magnetostratigraphic interpretation (Table **T9**) in the upper 50 m of Hole U1553A can be reconciled with foraminifer datums in this interval. Option 1 results in an age reversal for *S. angiporoides*, whereas Option 2 results in age reversals for *C. cubensis* and *S. angiporoides*. We show a possible line of correlation based on Option 1 (dashed line in Figure **F61**), but the preferred line of correlation is based on biostratigraphic datums because it is consistent with both foraminifer and radiolarian datums in this interval and avoids age reversals. In the entire sequence, only one age reversal is noted. The top of early Eocene index species

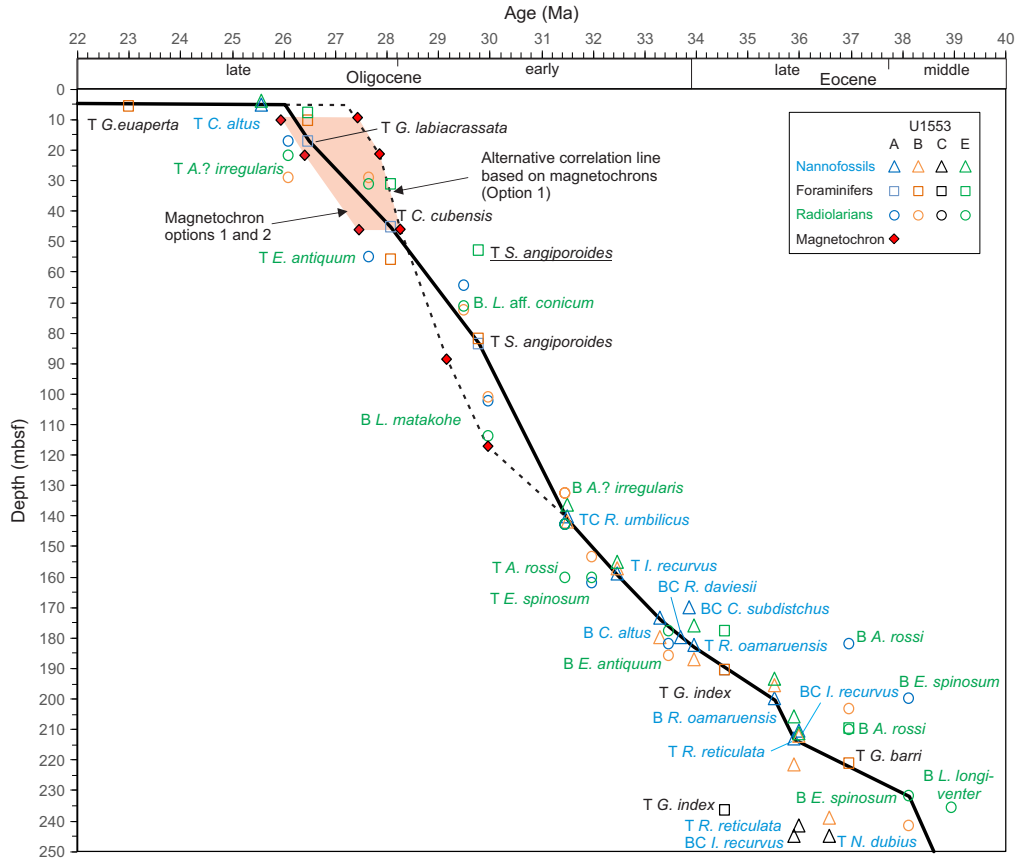

Figure F61. Age-depth plot, 22–40 Ma, Site U1553. Underlined datums are age reversals. T = top, B = base, TC = top common occurrence, BC = base common occurrence.

A. prolixum is found to occur in the middle Eocene (Figure **F60**). The upper range limit of this species is not well established; therefore, this may represent a true range extension for the species.

Several other datums are not age reversals, but they do represent last occurrences earlier than the established datum age or first occurrences later than the established datum age. This is likely an artifact of a preliminary study based on widely spaced core catcher samples. With further study of samples, it is anticipated that a closer fit with the correlation line will emerge.

9.2. Comparison with Site 277

Many of the biostratigraphic datums identified at Site U1553 were also found at the single hole, spot cored DSDP Site 277 (Hollis et al., 1997, 2014, 2015). A depth-depth plot of datums for the two sites (Figure **F62**) shows very good correspondence in the upper part (<200 mbsf) but more divergence in the lower part where spot-coring at Site 277 is likely a contributing factor for sporadic identification of marker species. In studies of Site 277 (Hollis et al., 1997, 2014, 2015), unconformities were identified in the middle Eocene (~45 Ma), early Eocene (~54 Ma), and late Paleocene (~59.60 Ma). Further study may also reveal uncertainties in some intervals of low sedimentation rate in the lowermost 340 m of Site U1553. Overall, there is a good linear correlation between the two sites.

9.3. Linear sedimentation rates

Major changes in linear sedimentation rates (LSRs) were calculated (Table **T19**) and are illustrated as line segments in the age-depth plot (Figure **F60**). They are plotted versus depth and age in Figure **F63**.

9.4. Mass accumulation rates

Mass accumulation rates (MARs) are listed for the LSR intervals in Table **T19**. They are plotted versus depth (mbsf scale) and age in Figure **F63** alongside the LSRs. MARs were calculated from

Table T19. Primary datum tie points and linear sedimentation rates, Site U1553. T = top, TC = top common occurrence, B = bottom. **Download table in CSV format.**

Datum	Age (Ma)	Core, section, interval (cm) Top	Core, section, interval (cm) Bottom	Depth (mbsf) Top	Depth (mbsf) Base	Depth (mbsf) Midpoint	Depth (mcd) Top	Depth (mcd) Base	Depth (mcd) Midpoint	Tie point (mbsf) Top	Tie point (mbsf) Base	LSR (cm/ky)	MAR (g/cm²/ky)
		384-U1553A-	384-U1553A-										
Unconformity	26.00					5.00							
T *Globigerina labiacrassata*	26.50	2H-CC, 14	3H-CC, 14	12.98	22.14	17.56	12.68	22.28	17.48	5.00	17.56	2.51	2.55
TC *Chiloguembelina cubensis*	28.10	5H-CC, 13	6H-CC, 13	40.68	50.34	45.51	42.07	53.19	47.63	17.56	45.51	1.75	1.72
T *Subbotina angiporoides*	29.80	9H-CC, 13	10H-CC, 17	79.02	88.88	83.95	82.88	92.77	87.82	45.51	83.95	2.26	2.34
TC *Reticulofenestra umbilicus* (>14 µm)	31.51	18H-1, 100	18H-2, 100	139.30	140.81	140.06	149.06	150.57	149.81	83.95	140.06	3.28	3.58
T *Isthmolithus recurvus*	32.49	19H-5, 80	19H-6, 80	154.60	156.11	155.36	166.00	167.51	166.75	140.06	155.36	1.56	1.78
B *Chiasmolithus altus*	33.31	22F-2, 100	22F-3, 100	174.01	175.51	174.76	187.01	188.51	187.76	155.36	174.76	2.37	2.75
T *Reticulofenestra oamaruensis*	33.97	24X-2, 80	24X-3, 80	181.70	183.20	182.45	196.53	198.03	197.28	174.76	182.45	1.17	1.40
B *Reticulofenestra oamaruensis*	35.54	26X-1, 20	26X-2, 20	199.00	200.50	199.75	217.00	218.50	217.75	182.45	199.75	1.10	1.35
T *Reticulofenestra reticulata*	35.92	26X-CC, 46	27X-1, 46	203.97	209.06	206.52	221.97	229.02	225.49	199.75	206.52	1.78	2.13
		384-U1553C-	384-U1553C-										
B *Eucyrtidium spinosum*	38.15	3R-CC, 8	R-CC, 8	245.79	255.64	250.72	277.13	286.98	282.06	206.52	250.72	1.98	2.68
T *Acarinina primitiva*	39.10	5R-CC, 11	6R-CC, 3	265.74	277.77	271.75	297.08	309.11	303.09	250.72	271.75	2.21	3.02
B *Reticulofenestra reticulata*	40.69	10R-1, 30	10R-1, 100	297.90	298.60	298.25	329.24	329.94	329.59	271.75	298.25	1.67	2.23
B *Reticulofenestra umbilicus*	42.48	17R-5, 60	17R-CC, 6	337.87	338.52	338.19	369.21	369.86	369.53	298.25	338.19	2.23	3.18
T *Cassigerinelloita amekiensis*	46.13	20R-CC, 2	21R-CC, 13	355.54	364.52	360.03	386.88	395.86	391.37	338.19	360.03	0.60	0.84
T *Discoaster lodoensis*	47.41	22R-2, 60	22R-CC, 8	372.31	374.37	373.34	403.65	405.71	404.68	360.03	373.34	1.04	1.47
B *Discoaster sublodoensis* (5-rayed)	49.11	22R-CC, 8	23R-1, 60	374.37	380.50	377.44	405.71	411.84	408.77	373.34	377.44	0.24	0.34
T *Tribrachiatus orthostylus*	50.50	25R-CC, 8	26R-CC, 10	403.90	412.37	408.14	435.52	444.08	439.80	377.44	408.14	2.21	3.18
B *Acarinina primitiva*	51.43	27R-CC, 13	28R-CC, 7	421.61	437.43	429.52	452.95	468.26	460.60	408.14	429.52	2.30	4.03
B *Sphenolithus radians*	54.17	28R-3, 70	28R-4, 84	432.27	433.92	433.09	463.10	464.75	463.92	429.52	433.09	0.13	0.23
B *Tribrachiatus orthostylus*	54.37	28R-5, 36	28R-6, 84	434.95	436.85	435.90	465.78	467.68	466.73	433.09	435.90	1.40	2.42
T *Fasciculithus tympaniformis*	55.33	29R-2, 52	29R-3, 42	440.33	441.64	440.98	470.83	472.14	471.48	435.90	440.98	0.53	0.92
B *Discoaster multiradiatus*	57.20	31R-CC, 1	32R-CC, 13	448.01	457.98	453.00	480.68	490.85	485.76	440.98	453.00	0.64	1.15
		384-U1553D-	384-U1553D-										
B *Fasciculithus tympaniformis*	61.51	9R-1, 68	9R-2, 93	468.18	469.92	469.05	500.81	502.55	501.68	453.00	469.05	0.37	0.57
B *Palaeoperidinium pyrophorum*	62.50	10R-CC	11R-CC	478.14	488.11	483.13	510.77	520.74	515.76	469.05	483.13	1.42	2.04
T *Senoniasphaera inornata*	63.40	14R-CC	15R-CC	517.59	528.57	523.08	550.22	561.20	555.71	483.13	523.08	4.44	5.85
B *Trithyrodinium evittii*	64.00	17R-CC	18R-CC	553.79	564.74	559.27	586.42	600.93	593.68	523.08	559.27	6.03	8.51

the LSR interval values and the average of dry bulk density (ρ G) measurements (see **Physical properties**) within the intervals using the formula:

$$\text{MAR (g/cm}^2\text{/ky)} = \text{LSR (m/My)} \times \rho\ \text{G (g/cm}^3\text{)}/10.$$

The calculation excluded the upper 3–5 m (depending on the hole) above the Pleistocene–Oligocene unconformity. The MAR is primarily a function of the sedimentation rate in these relatively uniform carbonate sediments because ρ G varies little (see **Physical properties**).

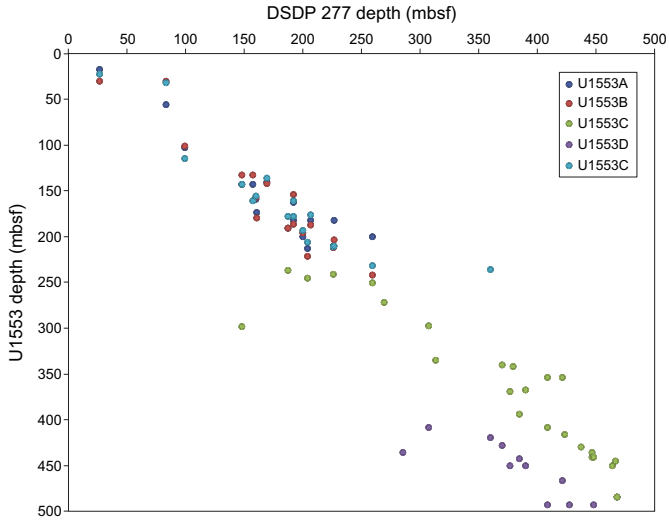

Figure F62. Depth-depth plot of biostratigraphic datums, Sites 277 and U1553.

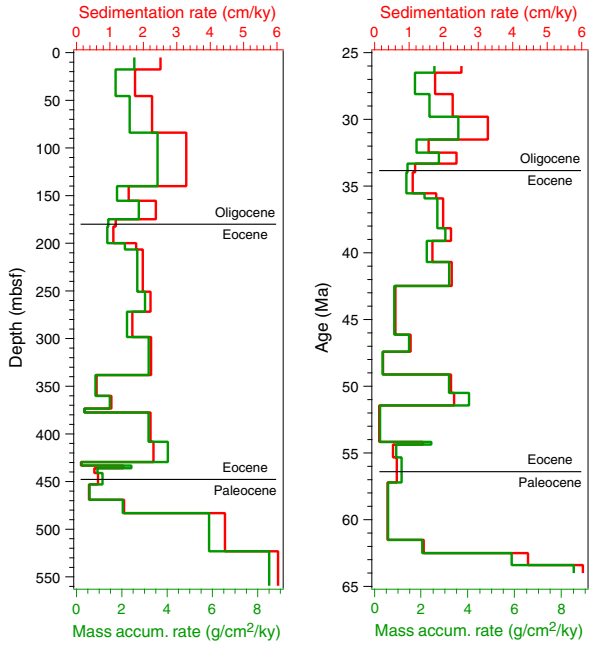

Figure F63. Linear sedimentation rate (LSR; red) and mass accumulation rate (MAR; green) plotted versus (left) depth and (right) age, Site U1553. See Table T18 for data.

References

Abelmann, A., 1990. Oligocene to middle Miocene radiolarian stratigraphy of southern high latitudes from Leg 113, Sites 689 and 690, Maud Rise. *In* Baker, P.F., Kennett, J.P., et al., *Proceedings of the Ocean Drilling Program, Initial Reports,* 113: College Station, TX (Ocean Drilling Program), 675–708. **https://doi.org/10.2973/odp.proc.sr.113.200.1990**

Agnini, C., Fornaciari, E., Raffi, I., Catanzariti, R., Palike, H., Backman, J., and Rio, D., 2014. Biozonation and biochronology of Paleogene calcareous nannofossils from low and middle latitudes. *Newsletters on Stratigraphy*, 47(2):131–181. **https://doi.org/10.1127/0078-0421/2014/0042**

Alegret, L., and Thomas, E., 2013. Benthic foraminifera across the Cretaceous/Paleogene boundary in the Southern Ocean (ODP Site 690): diversity, food and carbonate saturation. *Marine Micropaleontology*, 105:40–51. **https://doi.org/10.1016/j.marmicro.2013.10.003**

Anagnostou, E., John, E.H., Babila, T.L., Sexton, P.F., Ridgwell, A., Lunt, D.J., Pearson, P.N., Chalk, T.B., Pancost, R.D., and Foster, G.L., 2020. Proxy evidence for state-dependence of climate sensitivity in the Eocene greenhouse. *Nature Communications*, 11(1):4436. **https://doi.org/10.1038/s41467-020-17887-x**

Anagnostou, E., John, E.H., Edgar, K.M., Foster, G.L., Ridgwell, A., Inglis, G.N., Pancost, R.D., Lunt, D.J., and Pearson, P.N., 2016. Changing atmospheric CO_2 concentration was the primary driver of early Cenozoic climate. *Nature*, 533(7603):380–384. **https://doi.org/10.1038/nature17423**

Barker, P.F., 2001. Scotia Sea regional tectonic evolution: implications for mantle flow and palaeocirculation. *Earth-Science Reviews*, 55(1):1–39. **https://doi.org/10.1016/S0012-8252(01)00055-1**

Barker, P.F., and Thomas, E., 2004. Origin, signature and palaeoclimatic influence of the Antarctic Circumpolar Current. *Earth-Science Reviews*, 66(1–2):143–162. **https://doi.org/10.1016/j.earscirev.2003.10.003**

Barnet, J.S.K., Littler, K., Westerhold, T., Kroon, D., Leng, M.J., Bailey, I., Röhl, U., and Zachos, J.C., 2019. A high-fidelity benthic stable isotope record of Late Cretaceous-early Eocene climate change and carbon-cycling. *Paleoceanography and Paleoclimatology*, 34(4):672–691. **https://doi.org/10.1029/2019PA003556**

Bijl, P.K., Bendle, J.A.P., Bohaty, S.M., Pross, J., Schouten, S., Tauxe, L., Stickley, C.E., et al., 2013. Eocene cooling linked to early flow across the Tasmanian Gateway. *Proceedings of the National Academy of Sciences of the United States of America*, 110(24):9645–9650. **https://doi.org/10.1073/pnas.1220872110**

Bijl, P.K., Schouten, S., Sluijs, A., Reichart, G.-J., Zachos, J.C., and Brinkhuis, H., 2009. Early Palaeogene temperature evolution of the southwest Pacific Ocean. *Nature*, 461(7265):776–779. **https://doi.org/10.1038/nature08399**

Bralower, T.J., 2002. Evidence of surface water oligotrophy during the Paleocene-Eocene Thermal Maximum: nannofossil assemblage data from Ocean Drilling Program Site 690, Maud Rise, Weddell Sea. *Paleoceanography and Paleoclimatology*, 17(2):13-11–13-12. **https://doi.org/10.1029/2001PA000662**

Carmichael, M.J., Lunt, D.J., Huber, M., Heinemann, M., Kiehl, J., LeGrande, A., Loptson, C.A., et al., 2016. A model–model and data–model comparison for the early Eocene hydrological cycle. *Climate of the Past*, 12(2):455–481. **https://doi.org/10.5194/cp-12-455-2016**

Cramwinckel, M.J., Huber, M., Kocken, I.J., Agnini, C., Bijl, P.K., Bohaty, S.M., Frieling, J., et al., 2018. Synchronous tropical and polar temperature evolution in the Eocene. *Nature*, 559(7714):382–386. **https://doi.org/10.1038/s41586-018-0272-2**

Crouch, E.M., Willumsen, P.S., Kulhanek, D.K., and Gibbs, S.J., 2014. A revised Paleocene (Teurian) dinoflagellate cyst zonation from eastern New Zealand. *Review of Palaeobotany and Palynology*, 202:47–79. **https://doi.org/10.1016/j.revpalbo.2013.12.004**

Dallanave, E., Bachtadse, V., Crouch, E.M., Tauxe, L., Shepherd, C.L., Morgans, H.E.G., Hollis, C.J., Hines, B.R., and Sugisaki, S., 2016. Constraining early to middle Eocene climate evolution of the Southwest Pacific and Southern Ocean. *Earth and Planetary Science Letters*, 433:380–392. **https://doi.org/10.1016/j.epsl.2015.11.010**

De Vleeschouwer, D., Dunlea, A.G., Auer, G., Anderson, C.H., Brumsack, H., de Loach, A., Gurnis, M., et al., 2017. Quantifying K, U, and Th contents of marine sediments using shipboard natural gamma radiation spectra measured on DV *JOIDES Resolution*. *Geochemistry, Geophysics, Geosystems*, 18(3):1053–1064. **https://doi.org/10.1002/2016GC006715**

Dunlea, A.G., Murray, R.W., Sauvage, J., Spivack, A.J., Harris, R.N., and D'Hondt, S., 2015. Dust, volcanic ash, and the evolution of the South Pacific Gyre through the Cenozoic. *Paleoceanography and Paleoclimatology*, 30(8):1078–1099. **https://doi.org/10.1002/2015PA002829**

Expedition 317 Scientists, 2011. Methods. *In* Fulthorpe, C.S., Hoyanagi, K., Blum, P., and the Expedition 317 Scientists, *Proceedings of the Integrated Ocean Drilling Program,* 317: Tokyo (Integrated Ocean Drilling Program Management International, Inc.). **https://doi.org/10.2204/iodp.proc.317.102.2011**

Fioroni, C., Villa, G., Persico, D., Wise, S.W., and Pea, L., 2012. Revised middle Eocene-upper Oligocene calcareous nannofossil biozonation for the Southern Ocean. *Revue de Micropaléontologie*, 55(2):53–70. **https://doi.org/10.1016/j.revmic.2012.03.001**

Funakawa, S., and Nishi, H., 2005. Late middle Eocene to late Oligocene radiolarian biostratigraphy in the Southern Ocean (Maud Rise, ODP Leg 113, Site 689). *Marine Micropaleontology*, 54(3):213–247. **https://doi.org/10.1016/j.marmicro.2004.12.002**

Goodell, H.G., Meylan, M.A., and Grant, B., 1971. Ferromanganese deposits of the South Pacific Ocean, Drake Passage, and Scotia Sea. *In* Reid, J.L. (Ed.), *Antarctic Research Series* (Volume 15): *Antarctic Oceanology I:* Washington, DC (American Geophysical Union), 27–92. **https://doi.org/10.1029/AR015p0027**

Gradstein, F.M., Ogg, J.G., Schmitz, M.D., and Ogg, G.M. (Eds.), 2012. *The Geological Time Scale 2012:* Amsterdam (Elsevier). **https://doi.org/10.1016/C2011-1-08249-8**

Gutjahr, M., Ridgwell, A., Sexton, P.F., Anagnostou, E., Pearson, P.N., Palike, H., Norris, R.D., Thomas, E., and Foster, G.L., 2017. Very large release of mostly volcanic carbon during the Palaeocene-Eocene Thermal Maximum. *Nature*, 548(7669):573–577. **https://doi.org/10.1038/nature23646**

Hague, A.M., Thomas, D.J., Huber, M., Korty, R., Woodard, S.C., and Jones, L.B., 2012. Convection of North Pacific Deep Water during the early Cenozoic. *Geology*, 40(6):527–530. **https://doi.org/10.1130/G32886.1**

Harper, D.T., Hönisch, B., Zeebe, R.E., Shaffer, G., Haynes, L.L., Thomas, E., and Zachos, J.C., 2020. The magnitude of surface ocean acidification and carbon release during Eocene Thermal Maximum 2 (ETM-2) and the Paleocene-Eocene Thermal Maximum (PETM). *Paleoceanography and Paleoclimatology*, 35(2):e2019PA003699. **https://doi.org/10.1029/2019PA003699**

Hayward, B.W., Grenfell, H.R., Sabaa, A., Neil, H.L., and Buzas, M.A., 2010. Recent New Zealand deep-water benthic foraminifera: taxonomy, ecologic distribution, biogeography, and use in paleoenvironmental assessment. *GNS Science Monograph*, 26.

Held, I.M., and Soden, B.J., 2006. Robust responses of the hydrological cycle to global warming. *Journal of Climate*, 19(21):5686–5699. **https://doi.org/10.1175/JCLI3990.1**

Hollis, C.J., 2006. Radiolarian faunal turnover through the Paleocene-Eocene transition, Mead Stream, New Zealand. *Eclogae Geologicae Helvetiae*, 99(1):S79–S99. **https://doi.org/10.1007/s00015-006-0604-3**

Hollis, C.J., Dunkley Jones, T., Anagnostou, E., Bijl, P.K., Cramwinckel, M.J., Cui, Y., Dickens, G.R., et al., 2019. The DeepMIP contribution to PMIP4: methodologies for selection, compilation and analysis of latest Paleocene and early Eocene climate proxy data, incorporating version 0.1 of the DeepMIP database. *Geoscientific Model Development*, 12(7):3149–3206. **https://doi.org/10.5194/gmd-12-3149-2019**

Hollis, C.J., Handley, L., Crouch, E.M., Morgans, H.E.G., Baker, J.A., Creech, J., Collins, K.S., et al., 2009. Tropical sea temperatures in the high-latitude South Pacific during the Eocene. *Geology*, 37(2):99–102. **https://doi.org/10.1130/G25200A.1**

Hollis, C.J., Hines, B.R., Littler, K., Villasante-Marcos, V., Kulhanek, D.K., Strong, C.P., Zachos, J.C., Eggins, S.M., Northcote, L., and Phillips, A., 2015. The Paleocene-Eocene Thermal Maximum at DSDP Site 277, Campbell Plateau, southern Pacific Ocean. *Climate of the Past*, 11(7):1009–1025. **https://doi.org/10.5194/cp-11-1009-2015**

Hollis, C.J., Pascher, K.M., Kamikuri, S.-I., Nishimura, A., Suzuki, N., and Sanfilippo, A., 2017. Towards an integrated cross-latitude event stratigraphy for Paleogene radiolarians. *Newsletter of the International Association of Radiolarists*, 15:288–289.

Hollis, C.J., Tayler, M.J.S., Andrew, B., Taylor, K.W., Lurcock, P., Bijl, P.K., Kulhanek, D.K., et al., 2014. Organic-rich sedimentation in the South Pacific Ocean associated with late Paleocene climatic cooling. *Earth-Science Reviews*, 134:81–97. **https://doi.org/10.1016/j.earscirev.2014.03.006**

Hollis, C.J., Taylor, K.W.R., Handley, L., Pancost, R.D., Huber, M., Creech, J.B., Hines, B.R., et al., 2012. Early Paleogene temperature history of the southwest Pacific Ocean: reconciling proxies and models. *Earth and Planetary Science Letters*, 349–350:53–66. **https://doi.org/10.1016/j.epsl.2012.06.024**

Hollis, C.J., Waghorn, D.B., Strong, C.P., and Crouch, E.M., 1997. *Integrated Paleogene Biostratigraphy of DSDP Site 277 (Leg 29): Foraminifera, Calcareous Nannofossils, Radiolaria, and Palynomorphs, Report 97/7:* Lower Hutt, New Zealand (Institute of Geological & Nuclear Sciences Limited).

Hollister, C.D., and Nowell, A.R.M., 1991. HEBBLE epilogue. *Marine Geology*, 99(3):445–460. **https://doi.org/10.1016/0025-3227(91)90055-9**

Hönisch, B., Ridgwell, A., Schmidt, D.N., Thomas, E., Gibbs, S.J., Sluijs, A., Zeebe, R., et al., 2012. The geological record of ocean acidification. *Science*, 335(6072):1058–1063. **https://doi.org/10.1126/science.1208277**

Hornibrook, N.B., Brazier, R.C., and Strong, C.P., 1989. Manual of New Zealand Permian to Pleistocene foraminiferal biostratigraphy. *New Zealand Geological Survey Paleontological Bulletin*, 56.

Hovan, S.A., and Rea, D.K., 1992. Paleocene/Eocene boundary changes in atmospheric and oceanic circulation: a Southern Hemisphere record. *Geology*, 20(1):15–18. **https://doi.org/10.1130/0091-7613(1992)020%3C0015:PEBCIA%3E2.3.CO;2**

Hrouda, F., 1982. Magnetic anisotropy of rocks and its application in geology and geophysics. *Geophysical surveys*, 5(1):37–82. **https://doi.org/10.1007/BF01450244**

Huber, B.T., and Quillévéré, F., 2005. Revised Paleogene planktonic foraminiferal biozonation for the austral realm. *Journal of Foraminiferal Research*, 35(4):299–314. **https://doi.org/10.2113/35.4.299**

Huber, M., 2008. A hotter greenhouse? *Science*, 321(5887):353–354. **https://doi.org/10.1126/science.1161170**

Huber, M., Brinkhuis, H., Stickley, C.E., Doos, K., Sluijs, A., Warnaar, J., Schellenberg, S.A., and Williams, G.L., 2004. Eocene circulation of the Southern Ocean: was Antarctica kept warm by subtropical waters? *Paleoceanography and Paleoclimatology*, 19(4):PA4026. **https://doi.org/10.1029/2004PA001014**

Huber, M., and Caballero, R., 2011. The early Eocene equable climate problem revisited. *Climate of the Past*, 7(2):603–633. **https://doi.org/10.5194/cp-7-603-2011**

Hutchinson, D.K., de Boer, A.M., Coxall, H.K., Caballero, R., Nilsson, J., and Baatsen, M., 2018. Climate sensitivity and meridional overturning circulation in the late Eocene using GFDL CM2.1. *Climate of the Past*, 14(6):789–810. **https://doi.org/10.5194/cp-14-789-2018**

Ivany, L.C., Brey, T., Huber, M., Buick, D.P., and Schöne, B.R., 2011. El Niño in the Eocene greenhouse recorded by fossil bivalves and wood from Antarctica. *Geophysical Research Letters*, 38(16):L16709. **https://doi.org/10.1029/2011GL048635**

Janecek, T.R., and Rea, D.K., 1983. Eolian deposition in the northeast Pacific Ocean: Cenozoic history of atmospheric circulation. *Geological Society of America Bulletin*, 94(6):730–738. **https://doi.org/10.1130/0016-7606(1983)94<730:EDITNP>2.0.CO;2**

Jenkins, D.G., 1975. Cenozoic planktonic foraminiferal biostratigraphy of the southwestern Pacific and Tasman Sea—DSDP Leg 29. *In* Kennett, J.P., Houtz, R. E., et al., *Initial Reports of the Deep Sea Drilling Project,* 29: Washington, DC (US Government Printing Office), 449–467. **https://doi.org/10.2973/dsdp.proc.29.112.1975**

Kennett, J.P., Houtz, R.E., Andrews, P.B., Edwards, A.R., Gostin, V.A., Hajos, M., Hampton, M., Jenkins, D.G., Margolis, S.V., Ovenshine, A.T., and Perch-Nielsen, K., 1975. Introduction and explanatory notes. *In* Kennett, J.P., Houtz, R. E., et al., *Initial Reports of the Deep Sea Drilling Project,* 29: Washington, DC (US Government Printing Office), 3–16. **https://doi.org/10.2973/dsdp.proc.29.101.1975**

Kulhanek, D.K., Crouch, E.M., Tayler, M.J.S., and Hollis, C.J., 2015. Paleocene calcareous nannofossils from East Coast, New Zealand: biostratigraphy and palaeoecology. *Journal of Nannoplankton Research*, 35(2):155–176.

Lauretano, V., Hilgen, F.J., Zachos, J.C., and Lourens, L.J., 2016. Astronomically tuned age model for the early Eocene carbon isotope events: a new high-resolution benthic $\delta^{13}C$ benthic record of ODP Site 1263 between ~49 and ~54 Ma. *Newsletters on Stratigraphy*, 49(2):383–400. **https://doi.org/10.1127/nos/2016/0077**

Lawver, L.A., and Gahagan, L.M., 1998. Opening of Drake Passage and its impact on the Cenozoic Ocean. *In* Crowley, T.J., and Burke, K.C. (Eds.), *Tectonic Boundary Conditions for Climate Reconstructions:* Oxford (Oxford University Press), 212–223.

Lawver, L.A., and Gahagan, L.M., 2003. Evolution of Cenozoic seaways in the circum-Antarctic region. *Palaeogeography, Palaeoclimatology, Palaeoecology*, 198(1):11–37. **https://doi.org/10.1016/S0031-0182(03)00392-4**

Leri, A.C., Hakala, J.A., Marcus, M.A., Lanzirotti, A., Reddy, C.M., and Myneni, S.C.B., 2010. Natural organobromine in marine sediments: new evidence of biogeochemical Br cycling. *Global Biogeochemical Cycles*, 24(4):GB4017. **https://doi.org/10.1029/2010GB003794**

Littler, K., Röhl, U., Westerhold, T., and Zachos, J.C., 2014. A high-resolution benthic stable-isotope record for the South Atlantic; implications for orbital-scale changes in late Paleocene-early Eocene climate and carbon cycling. *Earth and Planetary Science Letters*, 401:18–30. **https://doi.org/10.1016/j.epsl.2014.05.054**

Liu, B., Saito, Y., Yamazaki, T., Abdeldayem, A., Oda, H., Hori, K., and Zhao, Q., 2001. Paleocurrent analysis for the late Pleistocene–Holocene incised-valley fill of the Yangtze delta, China by using anisotropy of magnetic susceptibility data. *Marine Geology*, 176(1):175–189. **https://doi.org/10.1016/S0025-3227(01)00151-7**

Lowrie, W., and Hirt, A.M., 1987. Anisotropy of magnetic susceptibility in the Scaglia Rossa pelagic limestone. *Earth and Planetary Science Letters*, 82(3):349–356. **https://doi.org/10.1016/0012-821X(87)90208-1**

Lunt, D.J., Jones, T.D., Heinemann, M., Huber, M., Legrande, A., Winguth, A., Loptson, C., et al., 2012. A mode-data comparison for a multi-model ensemble of early Eocene atmosphere ocean simulations: EoMIP. *Climate of the Past*, 8:1717–1736. **https://doi.org/10.5194/cp-8-1717-2012**

Lurcock, P.C., and Wilson, G.S., 2013. The palaeomagnetism of glauconitic sediments. *Global and Planetary Change*, 110(C):278–288. **https://doi.org/10.1016/j.gloplacha.2013.06.010**

Lyle, M., Gibbs, S., Moore, T.C., and Rea, D.K., 2007. Late Oligocene initiation of the Antarctic Circumpolar Current: evidence from the South Pacific. *Geology*, 35(8):691–694. **https://doi.org/10.1130/G23806A.1**

Martini, E., 1971. Standard Tertiary and Quaternary calcareous nannoplankton zonation. *Proceedings of the Second Planktonic Conference, Roma, 1970*, 2:739–785.

Norris, R.D., Wilson, P.A, Blum, P., and the Expedition 342 Scientists, 2014. *Proceedings of the Integrated Ocean Drilling Program*, 342: College Station, TX (Integrated Ocean Drilling Program). **https://doi.org/10.2204/iodp.proc.342.2014**

Ohneiser, C., and Tapia, C., 2020. Diagenesis of magnetic minerals at the Southwest Pacific DSDP Site 277. *New Zealand Journal of Geology and Geophysics*, 63(2):250–261. **https://doi.org/10.1080/00288306.2019.1665075**

Pagani, M., Huber, M., Liu, Z., Bohaty, S.M., Henderiks, J., Sijp, W., Krishnan, S., and DeConto, R.M., 2011. The role of carbon dioxide during the onset of Antarctic glaciation. *Science*, 334(6060):1261–1264. **https://doi.org/10.1126/science.1203909**

Pagani, M., Pedentchouk, N., Huber, M., Sluijs, A., Schouten, S., Brinkhuis, H., Sinninghe Damsté, J.S., et al., 2006. Arctic hydrology during global warming at the Palaeocene/Eocene Thermal Maximum. *Nature*, 442(7103):671–675. **https://doi.org/10.1038/nature05043**

Pearson, P.N., Foster, G.L., and Wade, B.S., 2009. Atmospheric carbon dioxide through the Eocene–Oligocene climate transition. *Nature*, 461(7267):1110–1113. **https://doi.org/10.1038/nature08447**

Pearson, P.N., Olsson, R.K., Huber, B.T., Hemleben, C., and Berggren, W.A., 2006. Atlas of Eocene planktonic foraminifera. *Special Publication - Cushman Foundation for Foraminiferal Research*, 41.

Pearson, P.N., van Dongen, B.E., Nicholas, C.J., Pancost, R.D., Schouten, S., Singano, J.M., and Wade, B.S., 2007. Stable warm tropical climate through the Eocene Epoch. *Geology*, 35(3):211–214. **https://doi.org/10.1130/G23175A.1**

Pfuhl, H.A., and McCave, I.N., 2005. Evidence for late Oligocene establishment of the Antarctic Circumpolar Current. *Earth and Planetary Science Letters*, 235(3):715–728. **https://doi.org/10.1016/j.epsl.2005.04.025**

Pierrot, D.E., Lewis, E., and Wallace, D.W.R., 2006. *MS Excel program developed for CO_2 system calculations:* Oak Ridge, TN (Carbon Dioxide Information Analysis Center, Oak Ridge National Laboratory, US Department of Energy).

Pimmel, A., and Claypool, G., 2001. Introduction to shipboard organic geochemistry on the *JOIDES Resolution*. *Ocean Drilling Program Technical Note*, 30. **https://doi.org/10.2973/odp.tn.30.2001**

Piper, J.D.A., Elliot, M.T., and Kneller, B.C., 1996. Anisotropy of magnetic susceptibility in a Palaeozoic flysch basin: the Windermere Supergroup, northern England. *Sedimentary Geology*, 106(3–4):235–258. **https://doi.org/10.1016/S0037-0738(96)00011-5**

Pribnow, D.F.C., Kinoshita, M., and Stein, C.A., 2000. *Thermal Data Collection and Heat Flow Recalculations for ODP Legs 101–180:* Hannover, Germany (Institut für Geowissenschaftliche Gemeinschaftsaufgaben). **http://www-odp.tamu.edu/publications/heatflow/**

Pross, J., Contreras, L., Bijl, P.K., Greenwood, D.R., Bohaty, S.M., Schouten, S., Bendle, J.A., et al., 2012. Persistent near-tropical warmth on the Antarctic continent during the early Eocene epoch. *Nature*, 488(7409):73–77. **https://doi.org/10.1038/nature11300**

Raine, J.I., Beu, A.G., Boyes, A.F., Campbell, H.J., Cooper, R.A., Crampton, J.S., Crundwell, M.P., Hollis, C.J., Morgans, H.E.G., and Mortimer, N., 2015. New Zealand Geological Timescale NZGT 2015/1. *New Zealand Journal of Geology and Geophysics*, 58(4):398–403. **https://doi.org/10.1080/00288306.2015.1086391**

Roberts, A.P., 2015. Magnetic mineral diagenesis. *Earth-Science Reviews*, 151:1–47. **https://doi.org/10.1016/j.earscirev.2015.09.010**

Roberts, A.P., Florindo, F., Chang, L., Heslop, D., Jovane, L., and Larrasoaña, J.C., 2013. Magnetic properties of pelagic marine carbonates. *Earth-Science Reviews*, 127:111–139. **https://doi.org/10.1016/j.earscirev.2013.09.009**

Röhl, U., Thomas, D.J., Childress, L.B., Anagnostou, E., Ausín, B., Borba Dias, B., Boscolo-Galazzo, F., Brzelinski, S., Dunlea, A.G., George, S.C., Haynes, L.L., Hendy, I.L., Jones, H.L., Khanolkar, S.S., Kitch, G.D., Lee, H., Raffi, I., Reis, A.J., Sheward, R.M., Sibert, E., Tanaka, E., Wilkens, R., Yasukawa, K., Yuan, W., Zhang, Q., Zhang, Y., Drury, A.J., and Hollis, C.J., 2022. Expedition 378 methods. *In* Röhl, U., Thomas, D.J., Childress, L.B., and the Expedition 378 Scientists, *South Pacific Paleogene Climate.* Proceedings of the International Ocean Discovery Program, 378: College Station, TX (International Ocean Discovery Program). **https://doi.org/10.14379/iodp.proc.378.102.2022**

Röhl, U., Westerhold, T., Bralower, T.J., and Zachos, J.C., 2007. On the duration of the Paleocene-Eocene Thermal Maximum (PETM). *Geochemistry, Geophysics, Geosystems*, 8(12):Q12002. **https://doi.org/10.1029/2007GC001784**

Rowan, C.J., and Roberts, A.P., 2006. Magnetite dissolution, diachronous greigite formation, and secondary magnetizations from pyrite oxidation: unravelling complex magnetizations in Neogene marine sediments from New Zealand. *Earth and Planetary Science Letters*, 241(1):119–137. **https://doi.org/10.1016/j.epsl.2005.10.017**

Savin, S.M., 1977. The history of the Earth's surface temperature during the past 100 million years. *Annual Review of Earth and Planetary Sciences*, 5(1):319–355. **https://doi.org/10.1146/annurev.ea.05.050177.001535**

Scher, H.D., and Martin, E.E., 2006. Timing and climatic consequences of the opening of Drake Passage. *Science*, 312(5772):428–430. **https://doi.org/10.1126/science.1120044**

Shackleton, N.J., and Kennett, J.P., 1975. Paleotemperature history of the Cenozoic and the initiation of Antarctic glaciation: oxygen and carbon isotope analyses in DSDP Sites 277, 279, and 281. *In* Kennett, J.P., Houtz, R. E., et al., *Initial Reports of the Deep Sea Drilling Project,* 29: Washington, DC (US Government Printing Office), 743–755. **https://doi.org/10.2973/dsdp.proc.29.117.1975**

Shipboard Scientific Party, 1975. Site 277. *In* Kennett, J.P., Houtz, R.E., et al., *Initial Reports of the Deep Sea Drilling Project,* 29: Washington, DC (US Government Printing Office), 45–120. **https://doi.org/10.2973/dsdp.proc.29.104.1975**

Shishkina, O.V., 1978. Distribution of bromine, Cl/Br relationships, and iodine in interstitial water of the Black Sea, based on DSDP Leg 42B. *In* Ross, D.A., Neprochnov, Y. P., et al., *Initial Reports of the Deep Sea Drilling Project,* 42, Part 2: Washington, DC (US Government Printing Office), 631–635. **https://doi.org/10.2973/dsdp.proc.42-2.122.1978**

Sibert, E., Friedman, M., Hull, P., Hunt, G., and Norris, R., 2018. Two pulses of morphological diversification in Pacific pelagic fishes following the Cretaceous–Palaeogene mass extinction. *Proceedings of the Royal Society, B: Biological Sciences*, 285(1888):20181194. **https://doi.org/10.1098/rspb.2018.1194**

Sluijs, A., Pross, J., and Brinkhuis, H., 2005. From greenhouse to icehouse; organic-walled dinoflagellate cysts as paleoenvironmental indicators in the Paleogene. *Earth-Science Reviews*, 68(3):281–315. **https://doi.org/10.1016/j.earscirev.2004.06.001**

Stickley, C.E., Brinkhuis, H., Schellenberg, S.A., Sluijs, A., Röhl, U., Fuller, M., Grauert, M., Huber, M., Warnaar, J., and Williams, G.L., 2004. Timing and nature of the deepening of the Tasmanian Gateway. *Paleoceanography and Paleoclimatology*, 19(4):PA4027. **https://doi.org/10.1029/2004PA001022**

Sutherland, R., Dickens, G.R., Blum, P., and the Expedition 371 Scientists, 2019. *Tasman Frontier Subduction Initiation and Paleogene Climate.* Proceedings of the International Ocean Discovery Program, 371: College Station, TX (International Ocean Discovery Program). **https://doi.org/10.14379/iodp.proc.371.2019**

Tauxe, L., 2005. Inclination flattening and the geocentric axial dipole hypothesis. *Earth and Planetary Science Letters*, 233(3–4):247–261. **https://doi.org/10.1016/j.epsl.2005.01.027**

Tauxe, L., Shaar, R., Jonestrask, L., Swanson-Hysell, N.L., Minnett, R., Koppers, A.A.P., Constable, C.G., Jarboe, N., Gaastra, K., and Fairchild, L., 2016. PmagPy: software package for paleomagnetic data analysis and a bridge to the Magnetics Information Consortium (MagIC) Database. *Geochemistry, Geophysics, Geosystems*, 17(6):2450–2463. **https://doi.org/10.1002/2016GC006307**

Taylor, K.W.R., Willumsen, P.S., Hollis, C.J., and Pancost, R.D., 2018. South Pacific evidence for the long-term climate impact of the Cretaceous/Paleogene boundary event. *Earth-Science Reviews*, 179:287–302. **https://doi.org/10.1016/j.earscirev.2018.02.012**

Thomas, D.J., Korty, R., Huber, M., Schubert, J.A., and Haines, B., 2014. Nd isotopic structure of the Pacific Ocean 70–30 Ma and numerical evidence for vigorous ocean circulation and ocean heat transport in a greenhouse world. *Paleoceanography and Paleoclimatology*, 29(5):454–469. **https://doi.org/10.1002/2013PA002535**

Tissot, B.P., and Welte, D.H., 1984. *Petroleum Formation and Occurrence*: New York (Springer-Verlag). **https://www.osti.gov/biblio/6632464**

Tjalsma, R.C., and Lohmann, G.P., 1983. *Paleocene-Eocene Bathyal and Abyssal Benthic Foraminifera from the Atlantic Ocean:* Flushing, NY (Micropaleontology Press).

Torsvik, T.H., Van der Voo, R., Preeden, U., Mac Niocaill, C., Steinberger, B., Doubrovine, P.V., van Hinsbergen, D.J.J., et al., 2012. Phanerozoic polar wander, palaeogeography and dynamics. *Earth-Science Reviews*, 114(3–4):325–368. **https://doi.org/10.1016/j.earscirev.2012.06.007**

van de Flierdt, T., Frank, M., Halliday, A.N., Hein, J.R., Hattendorf, B., Günther, D., and Kubik, P.W., 2004. Deep and bottom water export from the Southern Ocean to the Pacific over the past 38 million years. *Paleoceanography and Paleoclimatology*, 19(1):PA1020. **https://doi.org/10.1029/2003PA000923**

Wade, B.S., Pearson, P.N., Berggren, W.A., and Pälike, H., 2011. Review and revision of Cenozoic tropical planktonic foraminiferal biostratigraphy and calibration to the geomagnetic polarity and astronomical time scale. *Earth-Science Reviews*, 104(1–3):111–142. **https://doi.org/10.1016/j.earscirev.2010.09.003**

Watkins, N.D., and Kennett, J.P., 1977. Erosion of deep-sea sediments in the Southern Ocean between longitudes 70°E and 190°E and contrasts in manganese nodule development. *In* Heezen, B.C. (Ed.), *Developments in Sedimentology* (Volume 23): *Influence of Abbysal Circulation on Sedimentary Accumulations in Space and Time:* New York (Elsevier), 103–111. **https://doi.org/10.1016/S0070-4571(08)70553-3**

Wei, W., and Thierstein, H.R., 1991. Upper Cretaceous and Cenozoic calcareous nannofossils of the Kerguelen Plateau (southern Indian Ocean) and Prydz Bay (East Antarctica). *In* Barron, J., Larsen, B., et al., *Proceedings of the Ocean Drilling Program, Scientific Results,* 119: College Station, TX (Ocean Drilling Program), 467–493. **https://doi.org/10.2973/odp.proc.sr.119.165.1991**

Westerhold, T., Marwan, N., Drury, A.J., Liebrand, D., Agnini, C., Anagnostou, E., Barnet, J.S.K., et al., 2020. An astronomically dated record of Earth's climate and its predictability over the last 66 million years. *Science*, 369(6509):1383–1387. **https://doi.org/10.1126/science.aba6853**

Westerhold, T., Röhl, U., Donner, B., McCarren, H.K., and Zachos, J.C., 2011. A complete high-resolution Paleocene benthic stable isotope record for the central Pacific (ODP Site 1209). *Paleoceanography and Paleoclimatology*, 26(2):PA2216. **https://doi.org/10.1029/2010PA002092**

Westerhold, T., Röhl, U., Donner, B., and Zachos, J.C., 2018. Global extent of early Eocene hyperthermal events: a new Pacific benthic foraminiferal isotope record from Shatsky Rise (ODP Site 1209). *Paleoceanography and Paleoclimatology*, 33(6):626–642. **https://doi.org/10.1029/2017PA003306**

Willumsen, P.S., 2011. Maastrichtian to Paleocene dinocysts from the Clarence Valley, South Island, New Zealand. *Alcheringa: An Australasian Journal of Palaeontology*, 35(2):199–240. **https://doi.org/10.1080/03115518.2010.494484**

Yang, T., Zhao, X., Petronotis, K., Dekkers, M.J., and Xu, H., 2019. Anisotropy of magnetic susceptibility (AMS) of sediments from Holes U1480E and U1480H, IODP Expedition 362: sedimentary or artificial origin and implications for paleomagnetic studies. *Geochemistry, Geophysics, Geosystems*, 20(11):5192–5215. **https://doi.org/10.1029/2019GC008721**

Zhou, L., and Kyte, F.T., 1992. Sedimentation history of the South Pacific pelagic clay province over the last 85 million years inferred from the geochemistry of Deep Sea Drilling Project Hole 596. *Paleoceanography*, 7(4):441–465. **https://doi.org/10.1029/92PA01063**

Zijderveld, J.D.A., 1967. AC demagnetization of rocks: analysis of results. *In* Runcorn, S.K.C., Creer, K.M., and Collinson, D.W. (Ed.), *Methods in Palaeomagnetism:* Amsterdam (Elsevier), 254–286.